Materials Science

**7th Korean-Polish Joint Seminar
on Physical Properties of Magnetic Materials**

Warszawa, Poland, 1-5 December 2002

**Guest Editors
Henryk K. Lachowicz
Jang-Roh Rhee
Wojciech Suski**

Materials Science is an interdisciplinary journal devoted to experimental and theoretical research into the synthesis, structure, properties and applications of materials.

Among the materials of interest are:
- glasses and ceramics
- sol-gel materials
- photoactive materials (including materials for nonlinear optics)
- laser materials
- photonic crystals
- semiconductor micro- and nanostructures
- piezo-, pyro- and ferroelectric materials
- high-T_c superconductors
- magnetic materials
- molecular materials (including polymers) for use in electronics and photonics
- novel solid phases
- other novel and unconventional materials

The broad spectrum of the areas of interest reflects the interdisciplinary nature of materials research. Papers covering the modelling of materials, their synthesis and characterisation, physicochemical aspects of their fabrication, properties and applications are welcome. In addition to regular papers, the journal features issues containing conference papers, as well as special issues on key topics in materials science.

Materials Science is published under the auspices of the Centre of Advanced Materials and Nanotechnology of the Wrocław University of Technology, in collaboration with the Institute of Low Temperatures and Structural Research of the Polish Academy of Sciences and the Wroclaw University of Economics.

All accepted papers are placed on the Web page of the journal and are available at the address: http://MaterialsScience.pwr.wroc.pl

Editorial Office

Łukasz Maciejewski

Editorial layout

Hanna Basarowa

Printed in Poland

Contents

Professor Bogusław Kędzia

Professor Bogusław Kędzia, founder and the first Editor of *Materials Science,* passed away on 14 December 2002. His scientific career began in 1957 when, still being a student, he was appointed by Professor Bogusława Jeżowska-Trzebiatowska, then chairman of the 2 Chair of Inorganic Chemistry of the Wrocław University of Technology. Three years later, he graduated from the University, in 1963 he received PhD, in 1972 - DSc in Chemistry, and in 1976 he was appointed Professor of Chemistry. From 1969 until 1972 he was Director of the Institute of Inorganic Chemistry of the Wrocław University of Technology, between 1972 and 1979 he held the position of vice-Rector, and in 1980/81 - of the Rector of the Wrocław University of Technology. In 1993, he moved to the Central Institute of Labour Protection in Warsaw, where worked on modern multimedia for academic teaching of work safety and ergonomics.

Scientific interests of Professor Kędzia were focused on the coordination chemistry of rare and transition elements, mainly on their vibrational spectroscopy. In early years, he worked on the IR spectroscopy of uranyl compounds, then his interest shifted to transition metal complexes with organic ligands offering nitrogen, oxygen, sulfur and selenium atoms as coordinating centres. His late works were devoted to mono- and poly-nuclear carbonyls of chromium. A part of his results was obtained during his numerous visits to U.S. universities, where he collaborated with distinguished scientits (e.g., with Professor Kazuo Nakamoto).

As an instructor, he was involved in modernizing inorganic chemistry courses. He was advisor of six PhD students; two of them received later their DScs, and one holds at present the professorial title. He was also member of editorial boards of several scientific journals, and served on scientific and organizing committees of several Polish and international conferences.

Bogusław Kędzia was a man of wide interests and of warm heart. He will be missed by his colleagues and friends.

Walter Wojciechowski

From the Guest Editors

The Seventh Korean-Polish Joint Seminar on *Physical Properties of Magnetic Materials* was held from Sunday through Thursday, December 1-5, 2002, in Warsaw, in the seat of the Institute of Physics of the Polish Academy of Sciences. The Seminar was organized by the Institute of Physics and the Institute of Low Temperature and Structural Research, both belonging to the Polish Academy of Sciences. It was supported by the Polish Academy of Sciences, the Korean Science and Engineering Foundation, the Institute of Physics of the Polish Academy of Sciences, the Faculty of Materials Science and Engineering of the Warsaw University of Technology and the Committee of Physics of the Polish Academy of Sciences.

The first Seminar of the series, initiated by Professor Seong-Cho Yu of the Chungbuk National University, was held in Cheongju in 1995 as a satellite meeting to the 3 International Symposium on *Physics of Magnetic Materials* which took place in Seoul. It was then settled that the Seminar would be held annually. Accordingly, the following meetings were held in Warsaw (1996), Cracow (1997), again in Cheongju (1998), Seoul (1999) - just after the International Magnetics Conference INTERMAG 1999 in Kyongju, in Będlewo near Poznań (2000), and finally again in Warsaw (2002). In 2001, the seminar, which that time should have been held again in Poland, did not take place for reasons beyond the control of the organizers.

The present, seventh Seminar, similarly to the previous ones, was based on plenary sessions during which only invited lectures were presented. There were altogether 20 talks presented at the meeting, nine of them presented by the Korean participants, representing academic and research centers. The remaining eleven were given by the Polish attendees representing the universities and institutes of the Academy. Proceedings, issued as a special issue of *Materials Science,* contain 16 papers presented at the Seminar.

The Seminar was attended not only by the invited scientists but also by numerous participants from various academic and research institutions in Poland.

In our opinion, shared by a majority of the participants, the technical subject matter dealing with various facets of the fundamental and applied magnetics maintained a high standard. The majority of presentations were devoted to the hottest topics in magnetism being actually of the greatest interest of the worldwide community of magneticians. The Seminar was indeed motivating for its participants, as was confirmed by numerous animated discussions held at the sessions and continued dur-

ing the breaks. The meeting went on in an informal and friendly atmosphere providing relaxing conditions for such discussions.

The success of the Seminar is undoubtedly due to all of its participants, but in particular to the invited lecturers. We would like to take this opportunity to express our hearty appreciation to all of them. We also would like to thank all our colleagues from the Institute of Physics and Polish Academy of Sciences for their willing assistance in all aspects of planning and running the Seminar.

It was agreed at this meeting that the Seminar would be held not every year but every two years and that the next meeting will take place in Korea in 2004. We sincerely hope that the participants of the Joint Seminar will have a good chance to meet again in 2004, this time in Korea.

Henryk K. Lachowicz,

Jang-Roh Rhee,

Wojciech Suski

Structure analysis and local magnetic parameters of magnetoresistance tunnel junctions

CHEOLGI KIM [1*], CHONG-OH KIM[1], YONGKANG HU[1],
JAROSŁAW KANAK[2], TOMASZ STOBIECKI[2], SATOSHI OGATA[3],
MASAKIYO TSUNODA[3], MIGAKU TAKAHASHI[3]

[1]Department of Materials Engineering, Chungnam National University, Taejon, 305-764, Korea

[2]Department of Electronics, University of Mining and Metallurgy, 30-059 Krakow, Poland

[3]Department of Electronic Engineering, Tohoku University, Sendai 980-8579, Japan

The Magnetic Tunnel Junctions (MTJs) were deposited by DC magnetron sputtering method in the following layer sequence: Ta(50 Å)/Cu(100 Å)/Ta(50 Å)/$Ni_{80}Fe_{20}$(20 Å)/Cu(50 Å)/$Mn_{75}Ir_{25}$(100 Å) /$Co_{70}Fe_{30}$(25 Å)/Al-O/$Co_{70}Fe_{30}$(25 Å)/$Ni_{80}Fe_{20}$(t)/Ta(50 Å)/, with t = 0 Å, 100 Å and 1000 Å. X-ray diffraction analysis revealed that highly oriented *fcc* (111) of $IrMn_3$, Cu, $Ni_{80}Fe_{20}$ and $Co_{70}Fe_{30}$ crystal planes are stacked parallel to the substrate plane. An improvement of (111) texture and crystallinity was observed after annealing. The tunneling magnetoresistance ratio of patterned junction with electrode layer of $Ni_{80}Fe_{20}$ (t = 1000 Å) deposited on the free layer of $Co_{70}Fe_{30}$ (25 Å) exceeds 40% at a room temperature after annealing at 200 °C in the magnetic field of 1 kOe. Local hysteresis loops were measured using the magneto-optical Kerr effect system. Relatively irregular variations of the coercive force H_c and unidirectional anisotropy field H_{ua} in as-deposited sample are revealed. After 200 °C annealing, the H_c decreases but H_{ua} increases with smooth local variations. Two-dimensional plots of H_c and H_{ua} show symmetric saddle shapes with their axes aligned with the pinned layer. The distribution of surface roughness is symmetric with respect to the centre of MTJ. Correlation between surface roughness and the variation of H_{ua} suggests that the H_{ua} variation of the free layer is well described by dipole interactions in the form of so-called Néel "orange peel" coupling.

Key words: *coercive force; exchange coupling; TMR; XRD; MOKE; surface roughness*

1. Introduction

Ever since large tunnel magnetoresistance (TMR) at a room temperature was observed [1, 2], properties of magnetic tunnel junctions (MTJs) have been steadily

*Corresponding author, e-mail: cgkim@cnu.ac.kr.

improved. Recently MTJs with 60% TMR at a room temperature (RT) have been demonstrated [3]. This fact makes them appropriate for magnetic random access memory (M-RAM) devices [4, 5], highly sensitive bio-sensors [6, 7] or read heads in hard-disk drives [8].

As is generally known [9, 10], the tunneling resistance (R) depends on the relative orientation of the magnetization (M) of each layer. In a memory device, an independent switching of the magnetically soft layer is achieved by making the other layer either exchange-biased or magnetically hard. The antiparallel and parallel M arrangements in a tunnel junction may represent two states of a bit. Reading the information requires only the measurement of R. Writing the information involves a switching of M for one layer, ideally without affecting M for the reference layer.

To stabilize the reference layer, its hysteresis loop can be shifted away from the zero field by exchange biasing. M of the reference layer is pinned to an adjacent antiferromagnetic (AF) layer through an exchange interaction, which effectively acts as internal field on the reference layer and must be overcome in order to switch the layer.

The magnetization reversal in a stack of thin films may be strongly affected by various magnetic parameters. One important parameter is unidirectional anisotropy of free layer caused by the interlayer coupling between pinned and free layers separated by an insulating spacer. The main interlayer coupling effects have been identified to be RKKY-like coupling through an indirect exchange mediated by the itinerant electrons, and Néel's "orange peel" coupling from magnetic dipole interaction related to interfacial morphological corrugations [11–14]. When an insulating layer prevents electron itinerancy, dipole interaction is reasonable rather than RKKY-like coupling.

However, there are contradictory results for the correlation between exchange coupling and surface roughness; while one result indicates that the exchange coupling is inversely proportional to surface roughness [15, 16], the other claims that the exchange coupling is proportional to surface roughness [17]. A full understanding of their relationship has not been attained because of the complex material and magnetic parameters.

In reality, the inhomogeneity of material and structure are responsible for the above results, hence local magnetic parameters (magnetization, coercivity and unidirectional anisotropy field) in both free and pinned layers can be non-uniform over the junction.

The distribution of magnetic parameters probably arises from local variations of the magnetic anisotropy and/or coupling from grain to grain within each layer. The magnetization reversal and strength of exchange coupling play a decisive role in the magnetoresistivity (MR) ratio and its field sensitivity [18, 19].

In this work, we investigate not only general properties of the structure and magnetoresistance, but also distributions of the coercive force, unidirectional anisotropy field and surface roughness on patterned junctions prepared by DC-sputtering method. We discuss magnetic parameters obtained and coupling interactions in relation to the surface roughness.

2. Experimental

MTJs with the structure of Ta(50 Å)/Cu(100 Å)/Ta(50 Å)/$Ni_{80}Fe_{20}$(20 Å) /Cu(50 Å)/$Mn_{75}Ir_{25}$(100 Å)/$Co_{70}Fe_{30}$(25 Å)/Al-O/$Co_{70}Fe_{30}$(25 Å)/$Ni_{80}Fe_{20}$(t)/Ta(50 Å), and the thickness of $Ni_{80}Fe_{20}$ top electrode of $t = 0$ Å, 100 Å and 1000 Å (Fig. 1), were deposited on thermally oxidized Si wafers using DC magnetron sputtering with ultra pure Ar (9N) as a process gas, in a chamber with a base pressure of 3×10^{-9} Torr. For barrier formation, metallic Al film of 15 Å thickness was deposited and subsequently oxidized in an oxidation chamber with a radial line slot antenna (RLSA) for 2.45-GHz microwaves [3]. Kr was used as the inert gas mixed with O_2 molecular gas for the plasma oxidation. For the X-ray diffraction and VSM measurements, in the same deposition process simultaneously the samples in the form of discs of 10 mm in diameter were fabricated. In-situ patterned junctions were prepared using a shadow mask during deposition. The junction size was 180×180 μm^2 or 250×250 μm^2.
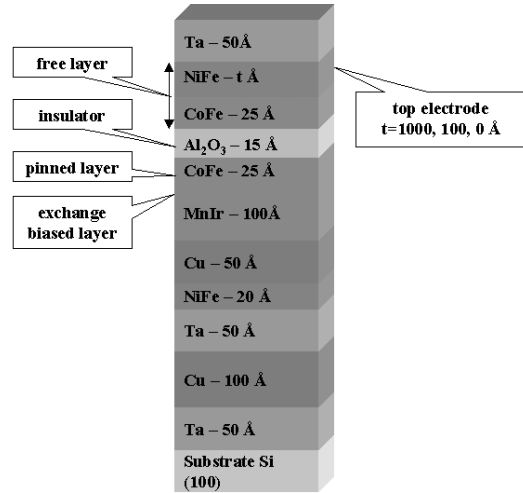
Fig. 1. Multilayer structure of MTJ

The junction samples were annealed at 200 °C for 1 hour under the magnetic field of 1 kOe, followed by field cooling. The magneto-optical Kerr effect (MOKE) method was used to obtain the local *M–H* loops under a 50 Hz driving magnetic field with 100 Oe amplitude. The penetration depth of He–Ne laser light is about 20 nm, which is enough to affect the whole thickness of the free layer. The field was applied in the annealing field direction. The laser beam size was about 2 μm in diameter, corresponding to the spatial resolution of the micro-MOKE system. The sample was scanned using a computer-controlled *x–y* stage to obtain a two-dimensional plot of magnetic parameters. The distribution of the surface roughness was determined by atomic force microscopy (AFM) at different points across the junction.

3. Results and discussion

3.1. Structure

In order to understand the different magnetic performances in as-deposited and annealed MTJs, an X-ray diffraction experiment was done in θ–2θ geometry for low
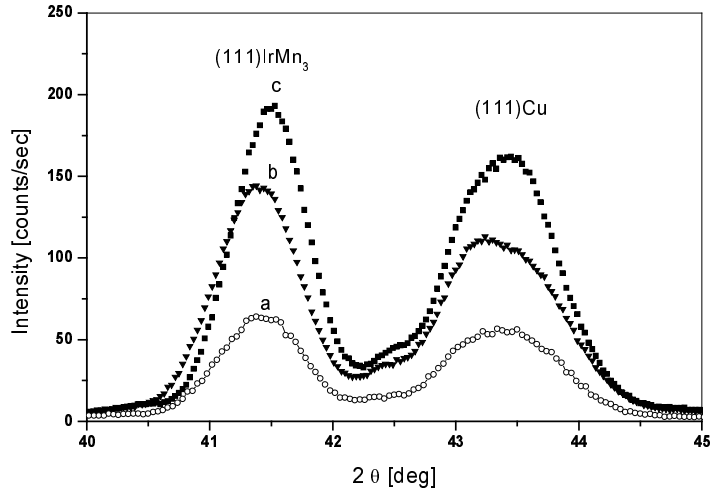
Fig. 2. Textured part of θ–2θ profile with *fcc* (111) IrMn$_3$, (111) Cu planes for as-deposited samples with free layer of Co$_{70}$Fe$_{30}$(25 Å) (a), Co$_{70}$Fe$_{30}$(25 Å)/Ni$_{80}$Fe$_{20}$ (t = 100 Å) (b) and annealed Co$_{70}$Fe$_{30}$(25 Å)/Ni$_{80}$Fe$_{20}$ (t = 100 Å) (c)
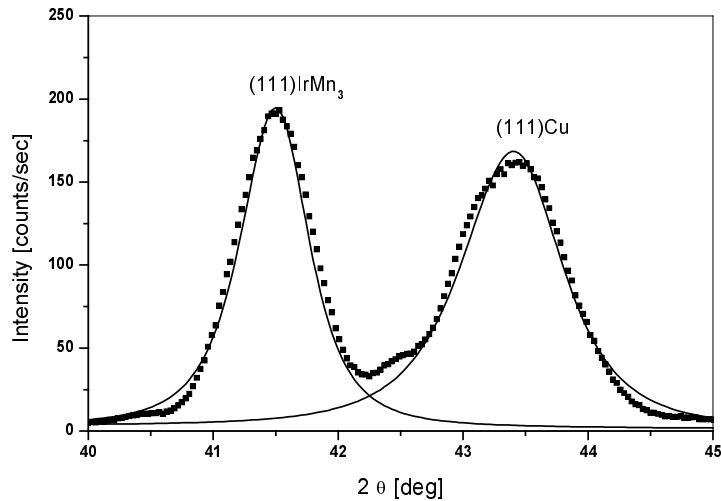
Fig. 3. θ–2θ profile for annealed samples of Co$_{70}$Fe$_{30}$(25 Å)/Ni$_{80}$Fe$_{20}$ (t = 100 Å) with fitting lines of *fcc*-(111) IrMn$_3$ and (111) Cu peaks

and high angles using a Philips diffractometer of the type X'Pert–MPD with Cu-anode (λ_{Cu} = 1.54184 Å). Figure 2 shows the high angle diffraction θ–2θ scan for the as-deposited and annealed stacking structure of the samples with the thickness of NiFe t = 0 Å and 100 Å. According to the diffraction data of Tsunoda [22], strong *fcc* peaks of (111) IrMn$_3$ and (111) Cu (not distinguished with *fcc* (111) Ni$_{80}$Fe$_{20}$ and Co$_{70}$Fe$_{30}$) are observed. These peaks manifested highly oriented *fcc* (111) crystal planes stacked parallel to the film plane. Lattice planes and lattice constants were determined from these peaks positions for as-deposited and annealed samples (as for example, Fig. 3). These parameters of *fcc*-(111) IrMn$_3$ and *fcc*-(111) Cu for the samples with the thickness of Ni$_{80}$Fe$_{20}$ t = 0 Å and 100 Å are: (111) IrMn$_3$ d = 2.179 Å (a = 3.775 Å) and d = 2.181 Å (a = 3.777 Å), respectively and for (111) Cu d = 2.085 Å (a = 3.612 Å) and d = 2.087 Å (a = 3.614 Å), respectively. The annealing treatment in vacuum at 200 °C for 1 hour induces an increase in (111) peaks intensity and a slight peak shift to higher 2θ position: (111) IrMn$_3$ d = 2.176 Å (a = 3.768 Å) and (111) Cu d = 2.084 Å (a = 3.610 Å) indicate an improvement in the crystallinity [22, 23] of the multilayer structure.
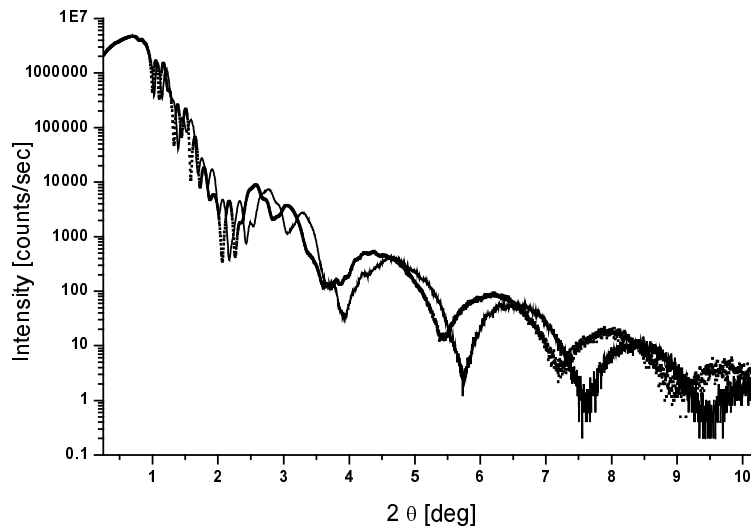
Fig. 4. The low angle diffraction θ–2θ reflectivity profiles
of as-deposited (solid line) and annealed (points) samples

The low-angle diffraction (scan θ–2θ) in the range of 2θ < 10° presents the reflectivity curves (Fig. 4) of as-deposited and annealed samples. No remarkable differences (within the accuracy of this experiment) were recognized in these curves (Fig. 4), meaning that no significant changes occurred in the interfacial roughness. The shift of reflectivity curve of annealed sample to the lower angle of 2θ indicates particularly an increase of the thickness of the Ta sublayer. Tantalum, due to twice higher the absorption coefficient of X-ray and density than other elements in multi-

layer system, dominates the periodicity of reflectivity profiles (Figs. 4, 5). The fitting analysis (using WINGIXA program of Philips, Fig. 5) proved that the thickness of IrMn$_3$ remains unchanged and Al–O barrier decreases only slightly after annealing: from 15.5 Å for as-deposited sample to 14 Å for annealed one.
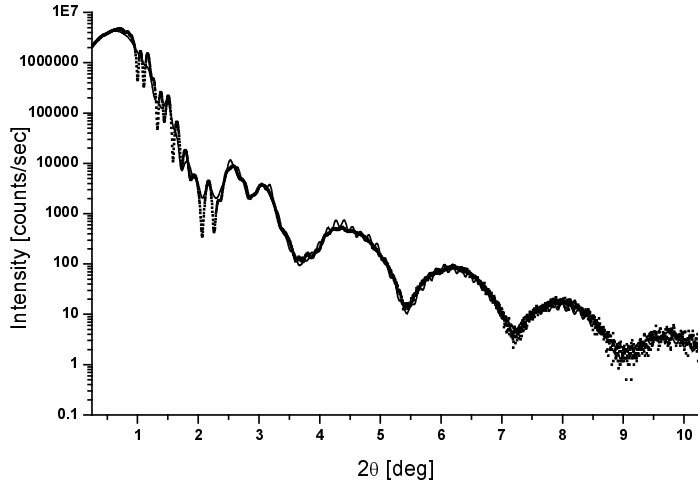
Fig. 5. θ–2θ reflectivity profile. Fitting profile (solid line) and experimental one (points)

The thickness of the top Ta layer increases by 8 Å (before annealing 55 Å, after – 63 Å) due to energetically preferred diffusion of Ni from the top electrode of Ni$_{80}$Fe$_{20}$ (high negative formation enthalpy of TaNi alloy, ΔH_{for}[TaNi] = –44kJ/mol) [24]. This conclusion is confirmed by the slight increase in the thickness (2 Å) of the bottom Ta layer (before annealing 47 Å, after 49 Å), because Cu from the adjacent layer does not diffuse into the bottom Ta layer due to negligibly small formation enthalpy (ΔH_{for}[TaCu] $\approx$ 0 kJ/mol) [24].

3.2. Tunneling magnetoresistance

The tunneling magnetoresistance was measured at RT in the cpp configuration (current perpendicular to the plane) with a four-point probe method for the sample annealed at 200 °C in magnetic field (1 kOe) with the electrode layer of Ni$_{80}$Fe$_{20}$ (1000 Å) deposited on the free layer of Co$_{70}$Fe$_{30}$ (25 Å). Figure 6 shows a typical high-field magnetoresistance hysteresis loop measured at RT for an annealed MTJ with the junction area of 250×250 μm^2. The major MR(H) loop originates from the magnetically hard electrode of Co$_{70}$Fe$_{30}$ (25 Å) pinned by the exchange biased coupling of antiferromagnetic IrMn$_3$ (100 Å) layer. The exchange biased field approaches H_{EB} of 1440 Oe. This value corresponds with unidirectional exchange biased energy 0.52 erg/cm^2 [22]. The minor MR(H) loop (as shown in Fig. 7) originates from the

free layer (top electrode) of $Co_{70}Fe_{30}$ (25 Å)/$Ni_{80}Fe_{20}$ (1000 Å). The coercive field of the free layer is about 3 Oe.
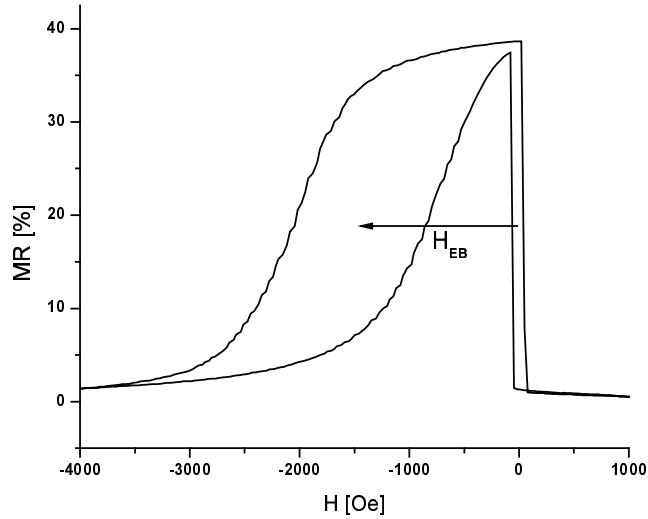
Fig. 6. High field MR-loop
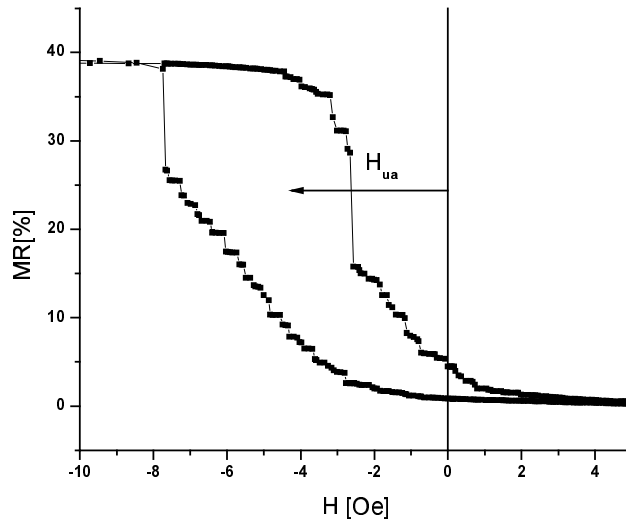
Fig. 7. Low field MR-loop

The minor loop is shifted about 5 Oe from zero magnetic field. The offset field (unidirectional anisotropy field H_{ua}), caused by the magnetic coupling between the pinned and free layers, has two components. The ferromagnetic coupling field, which is believed to result from the Néel "orange peel" coupling, is independent of the size of the junction and, on the other hand, the magnetostatic coupling which scales roughly in-

versely with the length of the junction is negligibly small, when the length of the pinned layer (i.e., the length of junction) is larger than 50 μm [20]. The minor MR(*H*) loop lies on the same side of the major MR(*H*) loop, indicating that the ferromagnetic "orange peel" coupling occurred between the free and pinned electrodes.

3.3. Local variation of magnetic parameters of free layer

In Figure 8, magnetooptical Kerr effect (MOKE) *M–H* loops are shown at several positions along the free-layer direction (the *y*-axis), as depicted in the inset of the figure. The *M–H* loop was measured under external magnetic field along the pinned-layer direction, i e. annealing field direction. There is no shift of the loop at the places located below the edge of the junction, as shown, for example, in Fig. 8. The shift due to the unidirectional anisotropy (bias) field H_{ua} increases as the measuring point moves to the junction centre, as shown in Figs. 8b–d, but then it decreases as the point moves away from the centre (Figs. 8e and f). One can also see a similar change of the coercive force H_c. Even though there are local variations of both H_c and H_{ua}, the squareness ratio of the loops is nearly constant.
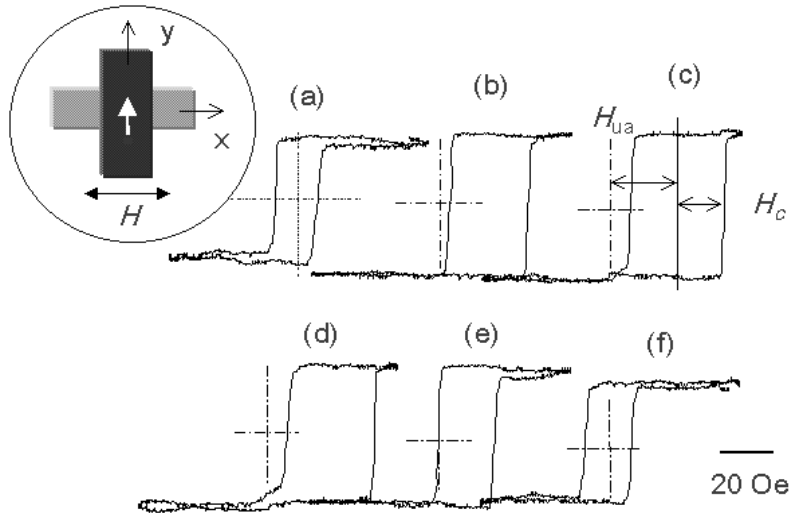
Fig. 8. MOKE *M–H* loops along the free-layer direction (the *y*-axis) at the positions:
0 (a), 105 (b), 130 (c), 165 (d), 205 (e), and 285 μm (f).
The starting point is 50 μm below the junction edge

Two-dimensional plots of maximum amplitude of the Kerr signal, obtained using a 20×20 scan, are shown in Figs. 9a, b for as-deposited and 200 °C-annealed junctions, respectively. The MOKE signal could be affected by the experimental parameters (e.g., the extinction coefficient of materials). Since the experimental parameters are fixed during the measurement, the maximum Kerr signal corresponds

with the maximum magnetization of a free layer. There is an irregular variation of the maximum Kerr signal in the as-deposited sample even near the centre of the free layer and also a gradual increase at the edge, and it reaches 90% of the centre value at 30 μm distance from the boundary. This variation is caused by the gradual change of film thickness (as shown in Fig. 10), arising from edge effects during deposition using a mask. After annealing, the irregular variation becomes smooth over the junction area except the edge region.
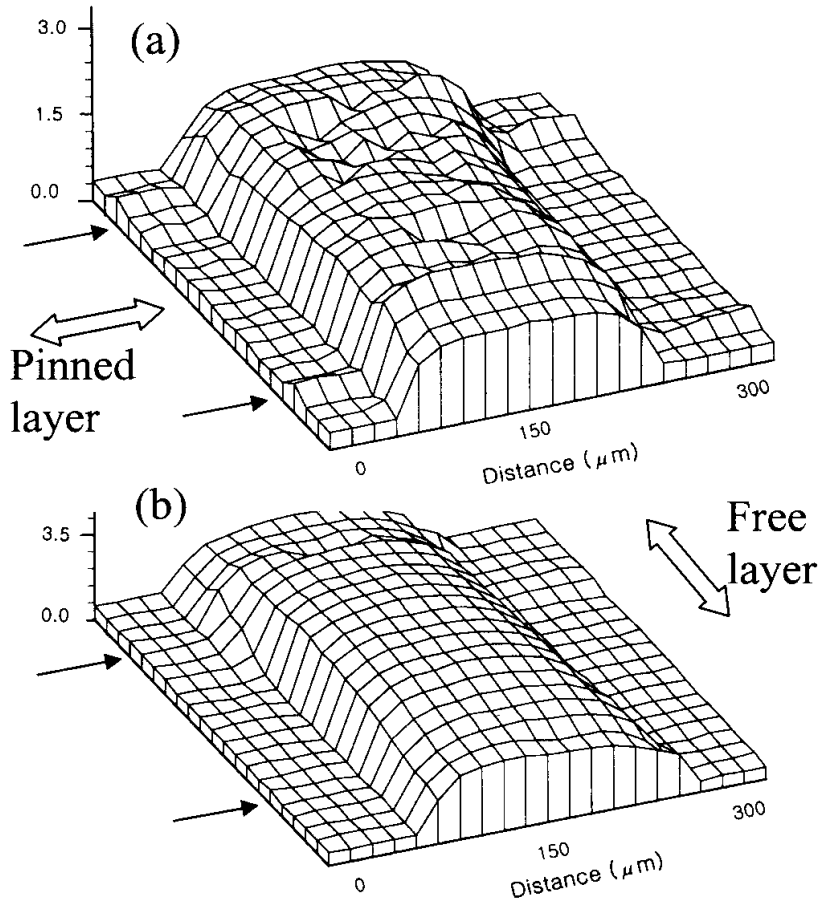
Fig. 9. Two-dimensional distribution of maximum magnetization in:
as-deposited (a) and annealed (b) samples

The variations of H_c and H_{ua} for an annealed sample are compared with those for an as-deposited one in Figs. 11a, b, respectively. H_c in the as-deposited sample is about 10 Oe outside the junction with maximum of 17.5 Oe at the junction centre. The local changes of H_c are quite irregular, as shown in Fig. 11a. As a whole, H_c is reduced after field annealing, while the local variation becomes smooth and symmetric

with respect to the centre of junction. Figure 11b shows an irregular change of H_{ua} with the maximum of 7.5 Oe at the junction centre in the as-deposited sample.
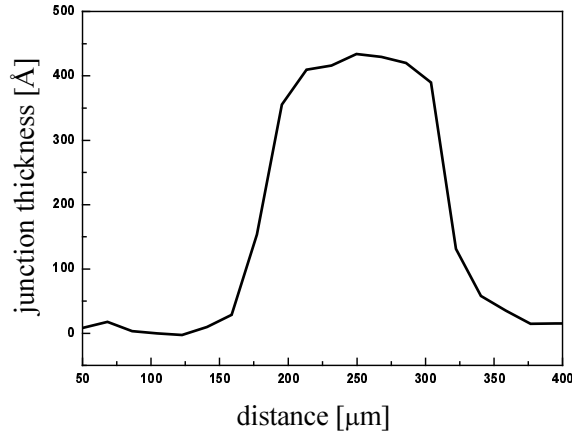
Fig. 10. α-step profile of the junction thickness

However, the field annealing enhances H_{ua} up to 20.5 Oe in the centre and, similarly to H_c variation, that of H_{ua} along the free layer becomes smooth (Fig. 11b). The enhancement of unidirectional anisotropy field and the smooth variations of H_{ua} and H_c after annealing are due to improvement of texture (111), increase of crystallites sizes, stress relaxation and alloying due to low-temperature diffusion [25].
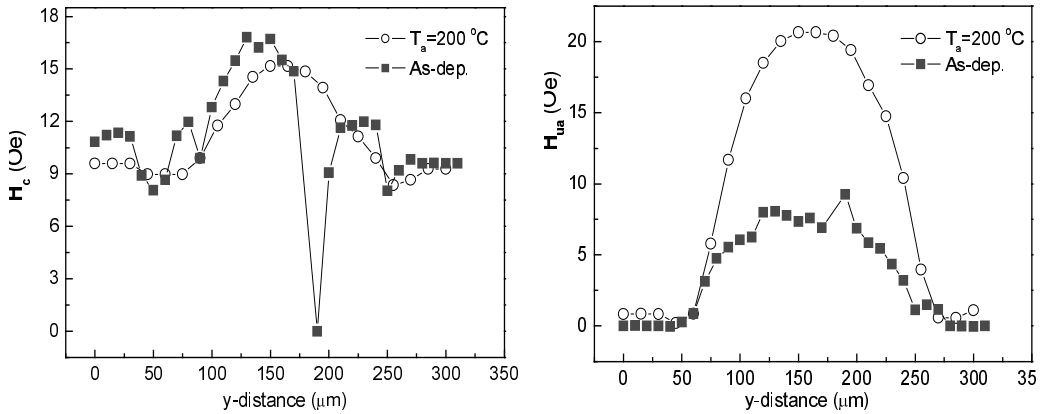
Fig. 11. Variation of coercive force H_c (a) and unidirectional bias field H_{ua} (b)
along the free-layer axis in as-deposited and annealed samples

As we describe later, magnetic dipole interaction between the free and pinned layers is an origin of H_{ua}. Thus, the above described changes of H_{ua} might be influenced by the changes of the exchange biased anisotropy of pinned layer during field annealing [22].
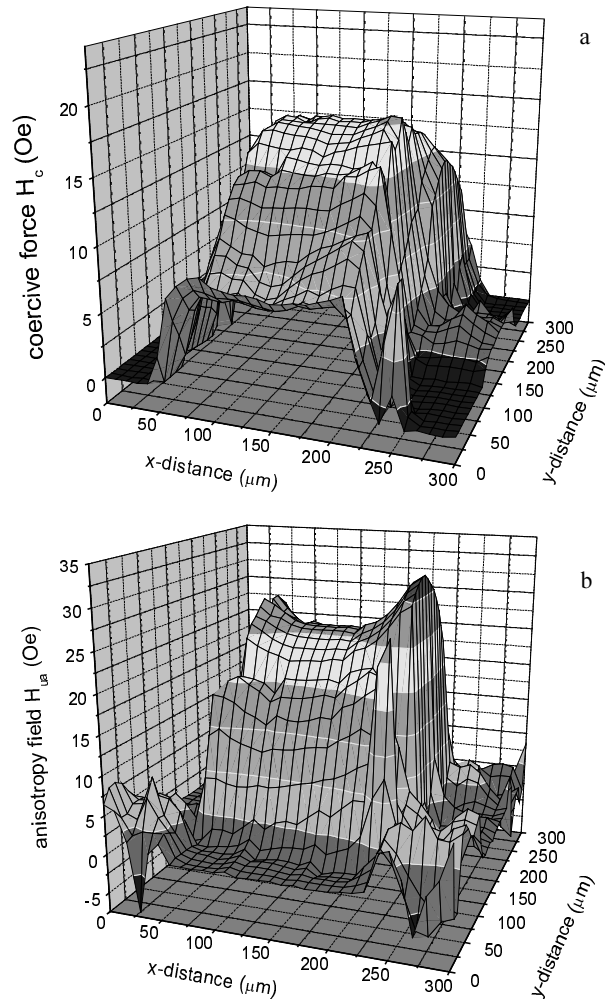
Fig. 12. Two-dimensional distribution of coercive force H_c (a) and unidirectional anisotropy field H_{ua} (b) in annealed sample: the x-axis: pinned layer, the y-axis: free-layer directions

In Figures 12a, b, two-dimensional plots of H_c and H_{ua}, respectively, are shown measured on the annealed sample, where measuring points are scanned over the entire junction area. Both H_c and H_{ua} show a saddle shape with its axis along the pinned-layer axis, where local variations along the pinned-layer axis are relatively small compared to those in the free-layer direction. As a whole, local variations of H_c and H_{ua} over the junction area are significant in comparison to the H_{ua} changes of magnetization (Fig. 9).

3.4. Surface roughness

Atomic force microscope (AFM) images across the pinned layer outside the junction are shown in Figs. 13a–d, at the measuring points $p1$–$p4$ depicted in the inset. At

C. KIM et al.

Pinned layer

P₁ P₃

P₂ P₄
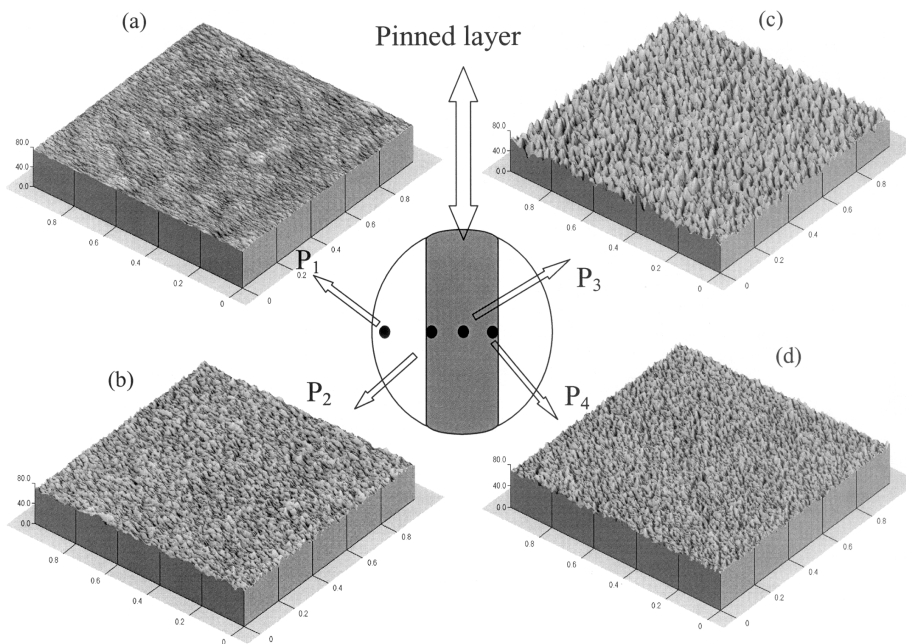
Fig. 13. AFM images across the pinned layer outside the junction: at the point $p1$, outside the layer (a); at point $p2$, near left edge (b); at point $p3$, centre (c) and at the point $p4$, near right edge (d). Scan area: 1×1 μm^2

Pinned layer

P₅ P₇

Free layer

P₆ P₈
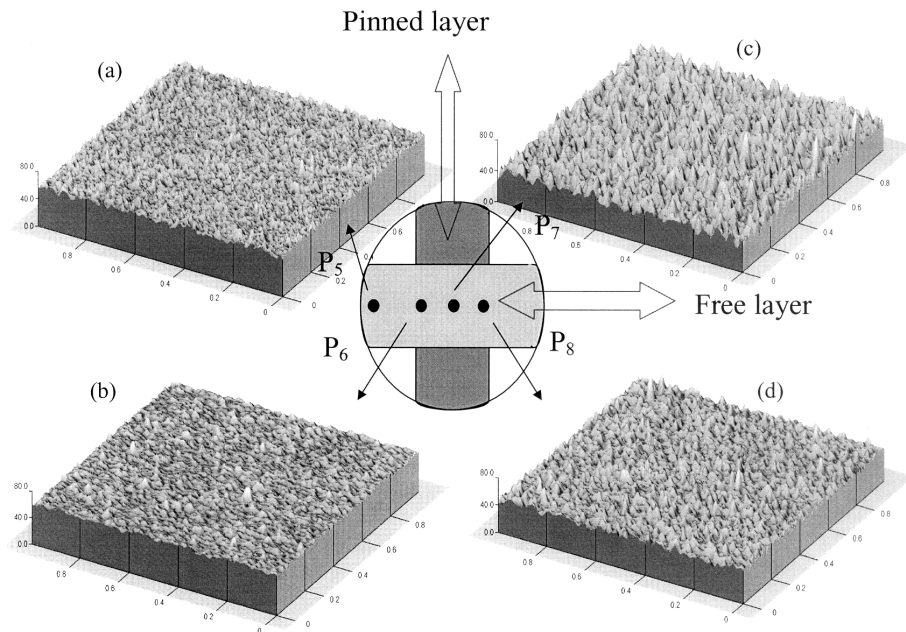
Fig. 14. AFM images along the free layer across the junction: at the point $p5$, outside the layer (a); at point $p6$, near left edge (b); at point $p7$, junction centre (c) and at the point $p8$, near right edge (d). Scan area: 1×1 μm^2

the point $p1$, outside the layer, the root mean square (RMS) roughness is 1.4 Å, corresponding to the surface roughness of the Si substrate. Within the layer, the roughness increases to 2.5 Å at $p2$ near the edge and to 5.5 Å at $p3$ near the centre of the layer, but then decreases to 2.7 Å near the left edge ($p4$).

In Figures 14a–d the AFM images are shown at several measuring points along the free layer across the junction. On the free layer outside the junction (point $p5$), RMS roughness is 3.3 Å, and becomes smaller, 2.3 Å at the near edge ($p6$). The roughness increases to 5.7 Å as the measuring point moves to the centre of the junction ($p7$), and then decreases as the point moves to the left edge ($p8$).

Figures 15a, b present the distribution of RMS roughness versus measuring distance, obtained from Figs. 13 and 14, respectively. The range of variation of RMS roughness is nearly the same (from 1.4 Å to 5.8 Å) and reveals symmetric variation with respect to the centre of the junction centre. However, the change near the edge is greater when roughness is measured on the free layer across the junction. These variations are quite similar to those of film thickness, as shown in the thickness profiles (given in Fig. 10). This may be a geometrical effect of the deposition process using a shadow mask.
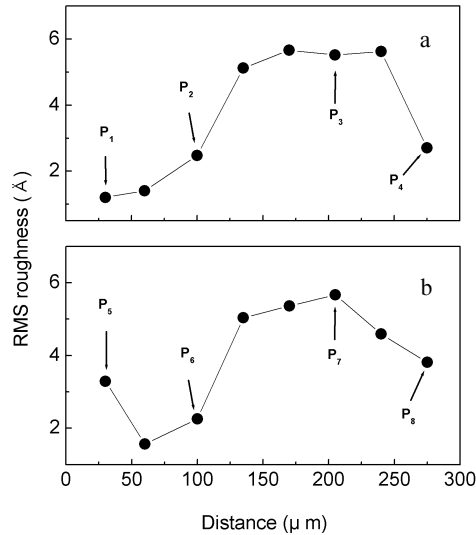
Fig. 15. Variation of average surface roughness
across the pinned layer (a) and along the free layer
across the junction (b)

In Figure 12, the H_{ua} distribution shape represents the exchange coupling field between free and pinned layers adjacent to the barrier of Al_2O_3. H_{ua} (~ 20 Oe) at the junction centre is about 4 times larger than that near the edge (~5 Oe). Ferromagnetic Néel's "orange peel" coupling by dipole interaction through tunneling barrier could be dominant over others such as RKKY-like interaction. In the Néel model,

a sinusoidal roughness profile is assumed and exchange coupling field H_N is expressed as [12]

$$H_N = \frac{\pi^2 h^2}{\sqrt{2} t_F \lambda} M_p \exp(-2\pi\sqrt{2} t_s / \lambda) \tag{1}$$

where h and λ are the amplitude and wavelength of the sinusoidal roughness profile, t_F and t_S are the thickness of the free layer and of the barrier layer, respectively, and M_p is the saturation magnetization of the pinned layer. Based on AFM measurement, the amplitude of the roughness profile is assumed to be 5.5 Å (RMS value at the junction centre). The wavelength of the roughness profile is reasonably assumed to be 100 Å as the grain diameter of the pinned $Co_{70}Fe_{30}$ layer as determined from XRD analysis [25]. Then, calculated from Eq. (1) the value of "orange peel" coupling is 22 Oe, being in reasonable agreement with the H_{ua} value at the junction centre.

M_p could be constant irrespective of the pinned layer thickness. When the thickness t_F is taken into account in denominator, the increase of H_{ua} at both edges, determined from measurements outside the junction, across the pinned layer (along the y-direction, Fig. 12b) where the roughness amplitude is small in relation to the centre (Figs. 13 and 15a), is described well by the decrease of t_F at the edges. But H_{ua} (Figs. 11b and 12b, along the x-direction), determined from the measurements inside the junction across the free layer, increases due to increasing roughness amplitude from the edge to the centre of junction (Figs. 14 and 15b). Because the exchange coupling field is given as a square function of the roughness amplitude h, the coupling at the junction centre along free layer is expected to be 4–5 times higher than that near the edge from the roughness shown in Figs. 14 and 15b. There is a good agreement between the measured and expected H_{ua} variations, suggesting that H_{ua} in the free layer is well described by dipole interaction between the free and pinned layers.

4. Conclusions

We have discussed the local variation of magnetization, coercive force and unidirectional anisotropy field of the free layer of MTJs in as-deposited and annealed samples. The XRD analysis revealed that highly oriented *fcc* (111) crystal planes of $IrMn_3$, Cu, $Ni_{80}Fe_{20}$ and $Co_{70}Fe_{30}$ grow parallel to the substrate plane. The annealing treatment improved the crystallinity and texture in the samples investigated which lead to smoother distributions of magnetization H_{ua} and H_c in annealed junction in comparison to as-deposited ones. Unidirectional anisotropy field H_{ua} should be uniform over the junction area when the thickness alone is taken into account in dipole interactions. However, roughness is also involved in dipole interactions, so the coupling at the junction centre is expected to be 4–5 times higher than that near the edge. There is a good agreement between the measured and expected H_{ua} variations, sug-

gesting that H_{ua} of the free layer is well described by dipole interaction in the term of Néel "orange-peel" coupling between the free and pinned layers. As a whole, the reversal magnetization is not uniform over the entire junction area and macroscopic properties are governed by the averages of the local distributions.

References

[1] MIYAZAKI T., TEZUKA N., J. Magn. Magn. Mater., 139 (1995), L231.

[2] MOODERA J.S., KINDER L.R., WONG T.M., MESERVEY R., Phys. Rev. Lett., 74 (1995), 3273.

[3] TSUNODA M., NISHIKAWA K., OGATA S., TAKAHASHI M., Appl. Phys. Lett., 80 (2002), 3135.

[4] PARKIN S.S.P., ROCHE K.P., SAMANT M.G., RICE P.M., BEYERS R.B., SCHEUERLEIN R.E., O'SULLIVAN E.J., BROWN S.L., BUCCHIGANO J., ABRAHAM D.W., LU YU, ROOKS P.L., TROUIL-LOUD M., WANER R.A., GALLAGHER W.J., J. Appl. Phys., 85 (1999), 5828.

[5] RICHTER R., BÄR L., WECKER J., REISS G., Appl. Phys. Lett., 80 (2002), 1291.

[6] MILLER M.M., SHEEHAN P.E., EDELSTEIN R.L., TAMANAHA C.R., ZHONG L., BOUNNAK S., WHIT-MAN L.J., COLTON R.J., J. Magn. Magn. Mat., 225 (2001), 138.

[7] SCHOTTER J., KAMP P.B., BECKER A., PÜHLER A., BRINKMANN D., SCHEPPER W., BRÜCKL H., REISS G., IEEE Trans. Magn., 38 (2002), 3365.

[8] SONG D., NOWAK J., LARSON R., KOLBO P., CHELLEW R., IEEE Trans. Magn., 36 (2000), 2545.

[9] JULLIERE M., Phys. Lett., 54A (1975), 225.

[10] SLONCZEWSKI J.C., Phys. Rev., B39 (1989), 6995.

[11] RUDERMAN M.A., KITTEL C., Phys. Rev., 96 (1954), 99.

[12] NÉEL L., C.R. Acad. Sci., 255 (1962), 1676.

[13] LEE C., BAIN J.A., CHU S., MCHENRY M.E., J. Appl. Phys., 91 (2002), 7113.

[14] STOBIECKI F., STOBIECKI T., OCKER B., MAASS W., POWROZNIK W., PAJA A., LOCH C., RÖLL K., Acta Phys. Polon., (A), 97 (2000), 523.

[15] MIURA S., TSUNODA M., TAKAHASHI M., J. Appl. Phys., 89 (2001), 6308.

[16] SHEN J.X., KIEF M.T., J. Appl. Phys., 79 (1996), 5008.

[17] PARK C.M., MIN K.I., SHIN K.H., IEEE Trans. Magn., 32 (1996), 3422.

[18] HOU C., CHEN J., KIEF M.T., GAO Z., MAO S., POKHIL T., Appl. Phys. Lett., 78 (2001), 237.

[19] HOU C., FUJIWARA H., UEDA F., J. Magn. Magn. Mater., 198–199 (1999), 450.

[20] SCHRAG B.D., ANGUUELOUCH A., XIAO G., TROUILLOUD P., LU YU, GALLAGHER W.J., PARKIN S.S.P., J. Appl. Phys., 87 (2000), 4682.

[21] LI K., WU Y., QIU J., HAN G., GUO Z., CHONG T., J. Magn. Magn. Mat., 241 (2002), 89.

[22] TSUNODA M., TSUCHIYA Y., HASHIMOTO T., TAKAHASHI M., J.Appl. Phys., 87 (2000), 4375.

[23] ANDERSON G., HUAI Y., MILOSLAWSKY L., J. Appl. Phys., 87 (2000), 6989.

[24] SCHMALHORST J., BRUECKL H., REISS G., GIERES G., WECKER J., J. Appl. Phys., 91 (2002), 6617.

[25] STOBIECKI T., KANAK J., KIM C.G., to be published.

Magnetic properties of Fe/Si and Co/Si multilayers

T. Luciński[1, 3*], M. Kopcewicz[2], A. Hütten[3],
H. Brückl[3], S. Heitmann[3], T. Hempel[3], G. Reiss[3]

[1]Institute of Molecular Physics, Polish Academy of Sciences,
Smoluchowskiego 17, 60-172 Poznań, Poland

[2]Institute of Electronic Materials Technology, Warsaw, Poland

[3]Faculty of Physics, University of Bielefeld, Bielefeld, Germany

Magnetic and structural properties of Fe/Si, Fe/Fe$_{33}$Si$_{66}$ and Co/Si multilayers have been studied. Very strong AF coupling $J = -1.93$ mJ/m^2 accompanied by saturation field of 1.5 T has been found for d_{Si} = 1.4 nm. The CEMS spectra recorded at room temperature consist of the Zeeman sextet characteristic of the pure Fe phase accompanied by two spectral components related to FeSi system: magnetic broad sextet and a quadrupole doublet. The broad sextet could originate from various Fe sites at the interface. The nonmagnetic QS doublet is most probably associated with the nonstoichiometric c-Fe$_{1-x}$Si$_x$ phase. Comparing the results obtained for Fe/Si and Fe/Fe$_{33}$Si$_{66}$ multilayers we conclude that the exchange coupling is distinctly stronger for nominally pure spacer layer. For Co/Si multilayers a very weak antiferromagnetic coupling and oscillatory $F_{AF}(d_{Si})$ behaviour was observed, most probably due to the formation of Co–Si nonmagnetic metallic phases replacing the nominally pure Si spacer layers. We have shown that AF coupled Fe/Si multilayers can be successfully applied as an antiferromagnets in the magnetoresistive (Fe/Si)$_{15}$/Fe/Co1/Cu/Co2 system.

Key words: *multilayers, interlayer coupling, magnetoresistance*

1. Introduction

Metal-semiconductor multilayers (Mls) have been extensively studied because of their potential application in electronics. Recently the investigations have been focused on Fe/Si/Fe coupled heterostructures, since they show a very strong antiferromagnetic (AF) interlayer coupling [1, 2]. In spite of many efforts, the origin of the interlayer coupling in Fe/Si system has not been clarified. Moreover, it is not well understood how the formation of iron silicides affects the interlayer coupling. Therefore the information about the interface structure and its correlation with magnetic

---

*Corresponding author, e-mail: Lucinski@ifmpan.poznan.pl.

properties of this system is of particular interest. Compared to the extensive studies of Fe/Si systems there are relatively few reports discussing Co/Si systems [3–5]. The interlayer coupling in Co/Si was found to be antiferromagnetic between 0.8 and 1.7 nm. In this contribution we present the results of the magnetic studies of Fe/Si and Co/Si Mls.

2. Experimental

The $\{Fe(d_{Fe})/Si(d_{Si})\}_{15}$ + $Fe(d_{Fe})$, $\{Fe(d_{Fe})/Fe_{33}Si_{66}(d_{Fe_{33}Si_{66}})\}_{15}$ + $Fe(d_{Fe})$, and $\{Co(d_{Co})/Si(d_{Si})\}_{15}$ + $Co(d_{Co})$ Mls were deposited by d.c. magnetron sputtering at room temperature (RT) onto SiO_x wafers. The crystalline structure of samples and their periodicity were examined using the high- and small-angle X-ray diffraction, HAXRD and SAXRD, respectively, whereas the interface structure of the Fe/Si Mls were studied by conversion electron Mössbauer spectroscopy (CEMS). Magnetization measurements were performed at RT using a vibrating sample magnetometer and magnetooptical Kerr effect (MOKE).

3. Results and discussion

3.1. Fe/Si and Fe/Fe$_{33}$Si$_{66}$ multilayers

Figure 1 shows examples of the field dependence of the Fe/Si magnetic moment of Mls with d_{Fe} = 3 nm for different Si thicknesses. As can be seen, the magnetic parameters like the remnant (M_R) to saturation (M_S) magnetization ratio (the so-called $F_{AF} = 1 - M_R/M_S$ parameter) and saturation field (H_S) are strongly influenced by Si spacer thickness. The F_{AF} parameter may indicate (or may be proportional to) the existence of the AF coupled fraction of Fe/Si Mls. $F_{AF}(d_{Si})$ dependence shows that the AF coupling occurs only for $1 \leq d_{Si} \leq 1.5$ nm and is centred at about $d_{Si} = 1.4$ nm where $F_{AF} = 0.9$ (Fig. 2). The same dependence and the occurrence of only single maximum of F_{AF} are reproduced by $H_S(d_{Si})$. For $d_{Si} = 1.4$ nm H_S reaches its maximum value of about 1.5 T which may be ascribed, according to the relation $J = (1/4)H_S M_S d_{Fe}$, to the occurrence of a very strong AF interlayer coupling $J = -1.93$ mJ/m^2. Above $d_{Si} = 1.4$ nm saturation fields decay exponentially and for thicker Si spacer no additional H_S peaks were found up to $d_{Si} = 5$ nm. For $d_{Si} > 1.5$ nm both F_{AF} and H_S values are strongly reduced, $F_{AF} < 0.5$ and $H_S < 0.1$ T. The reduction of F_{AF} and H_S values for $d_{Si} < 1.4$ nm points out that the neighbour Fe layers become gradually connected through pinholes. The observed non-oscillatory but exponentially decaying saturation field values (see inset in Fig. 2) seem to correspond to the quantum interference model of exchange coupling [6].

Figure 3 displays SAXRD and HAXRD spectra for $d_{Fe} = 3$ nm and $d_{Si} = 1.4$ nm. SAXRD pattern proves a very well layered structure of the Mls with four superlattice peaks indicating strong composition modulation along the growth direction. The in-

tense peak near 70° (and all underlined refraction indexes) in the HAXRD spectrum is due to the Si substrate. Only one weak satellite peak is visible near bcc (110), in contrast to Fullerton [6], who observed satellite peaks around the Fe (110). However, this is in agreement with Chaiken [7], who observed only one satellite peak on the low-angle side of Fe (110) peak.
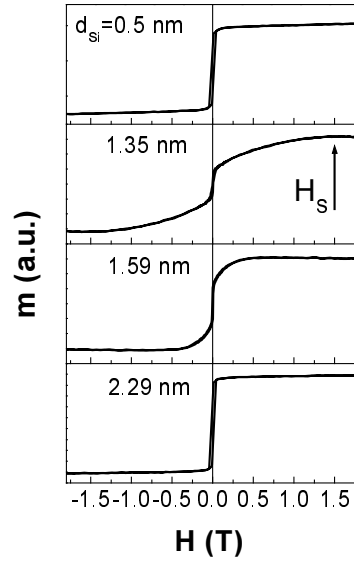
Fig. 1. Examples of the Fe/Si magnetic moment field dependencies of Mls with fixed $d_{Fe} = 3$ nm and different Si thicknesses
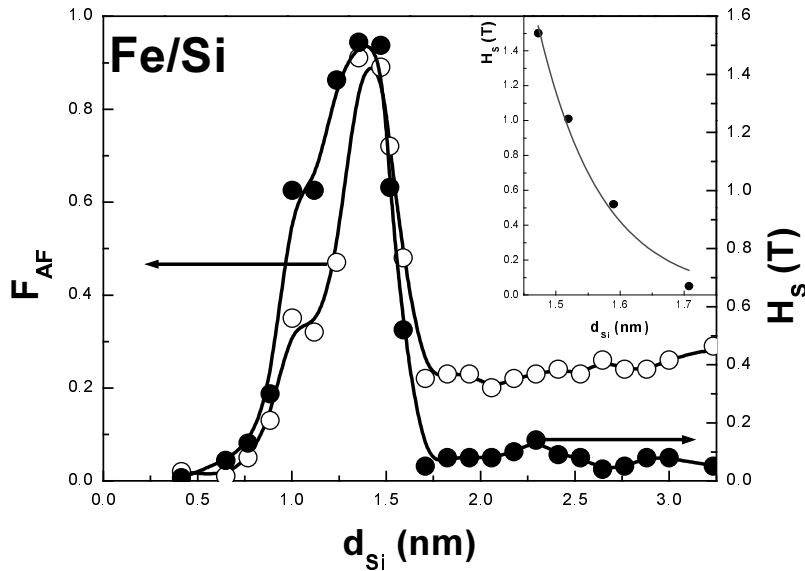
Fig. 2. Values of F_{AF} parameter, the saturation fields H_S versus d_{Si} for Fe/Si Mls with $d_{Fe} = 3$ nm. The inset shows the exponential decay of H_S as a function of d_{Si}
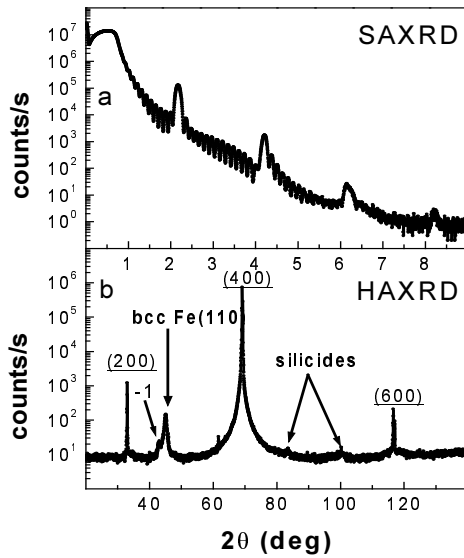
Fig. 3. Two typical small- (a) and high-angle (b) XRD spectra (SAXRD and HAXRD, respectively) for Fe/Si Ml with the strongest interlayer coupling (d_{Fe} = 3 nm and d_{Si} = 1.4 nm)

Our XRD measurements did not show any clear evidence of iron silicides formation at Fe/Si interfaces. Only two tiny peaks around 84° and 100° suggest the presence of Fe–Si phases. The absence of Fe–Si silicides in HAXRD spectra does not exclude their existence in Fe/Si Mls, but suggests that their volume fraction is very small. The possible candidates are nonmagnetic metallic phases of tetragonal α-FeSi$_2$ (and/or a semiconducting β-FeSi$_2$) and FeSi with CsCl structure.
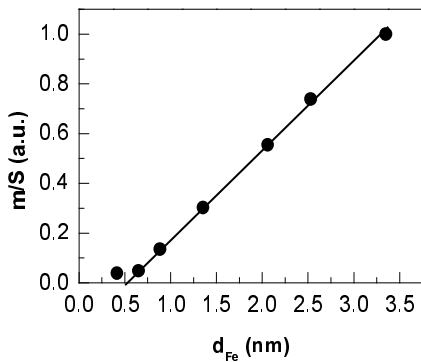
Fig. 4. Fe thickness dependence of magnetic moment per surface area (m/S) for Fe/Si Mls with constant d_{Si} = 2.5 nm

Figure 4 shows the Fe thickness dependence of magnetic moment per surface area (m/S) for Mls with d_{Si} = 2.5 nm. The relationship between m/S and d_{Fe} can be described by $m/S = M_0(1 - 2d_0/d_{Fe})$, where M_0 is an average magnetization of Fe layers and d_0 is an effective dead layer per single Fe/Si interface. The intercept of the straight line with d_{Fe} axis gives the thickness of nonmagnetic layers showing that about 0.25 nm thick nonmagnetic layer is formed at each Fe/Si interface. This may be ascribed to the intermixing of Fe and Si leading to the formation of thin nonmagnetic Fe–Si interfacial phases.
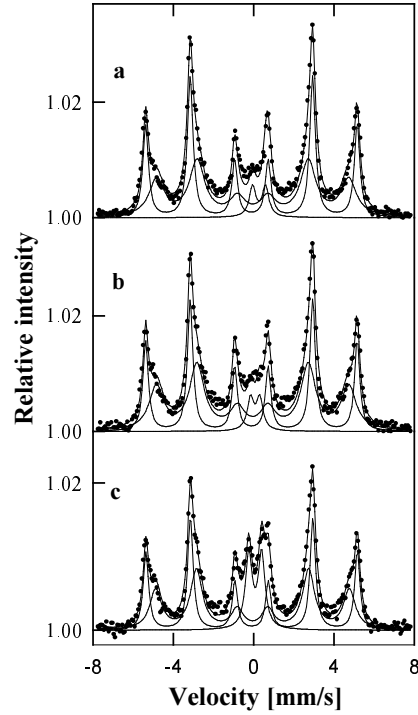
Fig. 5. CEMS spectra of Fe/Si Mls
with Si layer thickness of 1.2 nm (a),
1.4 nm (b) and 2.3 nm (c), respectively

To gain more information on the interface structure, CEMS measurements have been performed for the Fe/Si Mls with constant d_{Fe} = 3 nm and $1.2 \leq d_{Si} \leq 2.3$ nm. The CEMS spectra recorded at room temperature consist of the Zeeman sextet with narrow lines ($\Gamma \approx 0.32$ mm/s) and with the hyperfine field $H_{hf} \approx 32.8$ T and isomer shift IS = 0.00 mm/s, characteristic of the pure bcc-Fe phase, and of two spectral components related to the FeSi system: magnetic broad sextet and nonmagnetic quadrupole doublet (Fig. 5a–c). The broad sextet ($H_{hf} \approx 29$ T and $IS \approx 0.05$ mm/s) originates most probably from Fe atoms placed at various sites at the interface surrounded by Si atoms. The Fe atoms are located in a crystalline bcc phase surrounded by seven Fe atoms and one Si atom [8]. The spectral contribution of this sextet does not change significantly for various d_{Si} and contributes in about 50% to the total spectral area (Fig. 5). The nonmagnetic component, consisting of the quadrupole doublet (QS) with the quadrupole splitting of about 0.64 mm/s and isomer shift $IS \approx 0.20$ mm/s, could originate either from the ε-FeSi nonmagnetic small-gap semiconductor with a cubic symmetry or from the crystalline c-Fe$_{1-x}$Si$_x$ metallic metastable phase with a CsCl structure [9]. Stochometric c-FeSi phase, having a cubic structure, usually exhibits a single-line Mössbauer spectrum but, as shown by Strijkers [9], when Fe vacancies are introduced, a quadrupole splitting is observed. Furthermore, also strain in the layer reduces local symmetry introducing electric field gradient. Our spectral parameters of the QS doublet could also be related to the α-FeSi$_2$ or β-FeSi$_2$ phases. Our QS value of about 0.64 mm/s could correspond to the poorly resolved doublets with QS$_1$

= 0.47 mm/s and QS_2 = 0.73 mm/s of the α-FeSi$_2$ phase with a tetragonal structure [9, 10]. However, the QS values of β-FeSi$_2$ [11] are considerably smaller than those found in our CEMS spectra and therefore the presence of β-FeSi$_2$ phase could be excluded. The spectral contribution of the QS doublet increases from about 5.7% for $d_{Si} \leq$ 1.35 nm (Fig. 5a) to about 16% for d_{Si} = 2.3 nm (Fig. 5c). Since the QS doublet is a minor spectral component, it is difficult to identify clearly from the QS and IS values which FeSi-type phase appears in our Fe/Si Mls; however, the c-Fe$_{1-x}$Si$_x$ one seems to be more plausible.
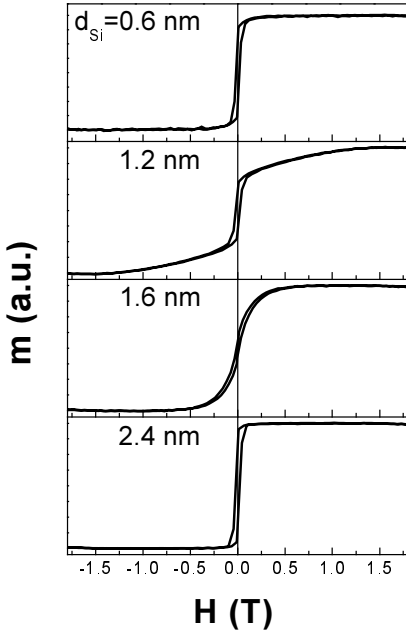
Fig. 6. Exemplary $m(H)$ loops for Fe/Fe$_{33}$Si$_{66}$ Mls for d_{Fe} = 3 nm and for different Fe$_{33}$Si$_{66}$-spacer layer thickness

In order to check the influence of Fe addition in Si spacer on H_S, we prepared {Fe($3nm$)/Fe$_{33}$Si$_{66}$($d_{Fe_{33}Si_{66}}$)}$_{15}$ + Fe($3nm$) Mls, with Fe$_{33}$Si$_{66}$ simulating the FeSi$_2$ phase. Figure 6 shows some examples of $m(H)$ loops and Fig. 7 displays the values of the F_{AF} and the H_S versus $d_{Fe_{33}Si_{66}}$. Comparing Fig. 2 and Fig. 7 one can realize that in the case of Fe$_{33}$Si$_{66}$-spacer layer, F_{AF} is reduced and its maximum is shifted towards thicker spacer layers values. Simultaneously, the position of the H_S maximum is almost unchanged; however, its value is visibly reduced from 1.5 (for Fe/Si Mls) to 1.3 T. The observed shift of the F_{AF} maximum value towards thicker spacer layers with unchanged position of H_S suggests the influence of pinholes for $d_{Fe_{33}Si_{66}} <$ 1.5 nm. Similarly to Fe/Si Mls saturation fields for $d_{Fe_{33}Si_{66}} >$ 1.2 nm decays exponentially (inset in Fig. 7) showing no oscillatory behaviour. Due to the appearance of ferromagnetic coupling at small spacer layer thickness (Fig. 2 and Fig. 7) attributable to the pinholes formation and very weak coupling observed above H_S peaks, the thickness dependence
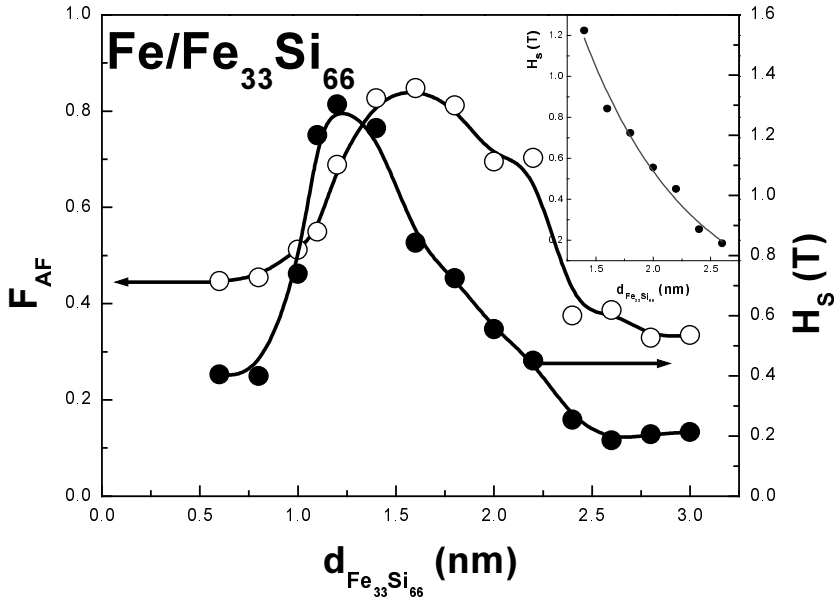
Fig. 7. The values of F_{AF} parameter and H_S field for Fe/Fe$_{33}$Si$_{66}$ Mls
as a function of $d_{Fe33Si66}$ for constant d_{Fe} = 3 nm.
The inset shows the exponential decay of $H_S(d_{Fe33Si66})$

of H_S across Si and Fe$_{33}$Si$_{66}$ spacers may be misread as a single maximum of an oscillation. Comparing the results obtained for Fe/Si and Fe/Fe$_{33}$Si$_{66}$ Mls we can conclude that the exchange coupling is distinctly stronger for nominally pure spacer layer.

3.2. Co/Si multilayers

In Co/Si Mls, a negative heat of mixing between Co and Si results in the formation of metastable amorphous phases and to the mutual solubility of constituents (see [4, 5] and references therein). This may be responsible for very complex and unusual magnetic behaviour. To our knowledge till now there was no detailed search for AF coupling in sputtered Co/Si Mls except the short information given in abstract [3] about the range of such a coupling.

Figure 8 displays examples of SAXRD and HAXRD spectra for d_{Co} = 3 nm and d_{Si} = 2.8 nm. SAXRD pattern proves a very well layered structure of the Mls with four superlattice peaks. All underlined refraction indexes in HAXRD are due to the Si substrate.

Figure 9 shows the MOKE loop shape variation of Co(d_{Co})/Si(2.4 nm) Mls for different d_{Co} in two magnetic field directions in Ml plane. One can immediately realize that character of the $m(H)$ traces depends on d_{Co}. We connect it with the evolution of the Co layer from superparamagnetic granular structures for $d_{Co} \leq 1$ nm through dis-

continuous granular Co layer for $1 < d_{Co} \leq 2$ nm and finally to continuous Co layer for $d_{Co} \geq 2.2$ nm. Figure 10 displays the Co thickness dependence of the sample moment per surface area (m/S). We have found that nominally about 0.25 nm thick layer per single Co/Si interface is magnetically inactive. However, in contrast to Fe/Si Mls, the character of the $m/S(d_{Co})$ is more complex revealing a drastic transition from discontinuous to continuous structure of Co layers at about $d_{Co} = 2$ nm. Such a behaviour suggests that the growth of Co on Si occurs in an island growth mode.
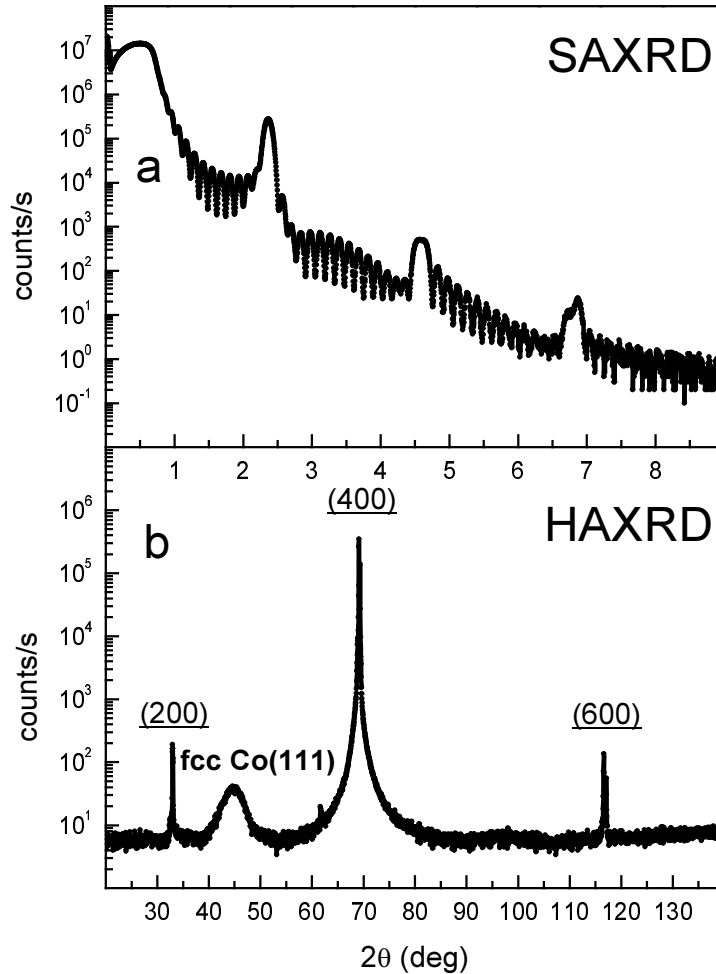
Fig. 8. Two typical small- (a) and high-angle (b) XRD spectra
(SAXRD and HAXRD, respectively) for Co/Si Ml with $d_{Fe} = 3$ nm and $d_{Si} = 2.8$ nm

Figure 11 shows the evolution of MOKE $m(H)$ loops for Co($3nm$)/Si(d_{Si}) versus Si thickness for selected samples. Such behaviour implies the existence of a weak
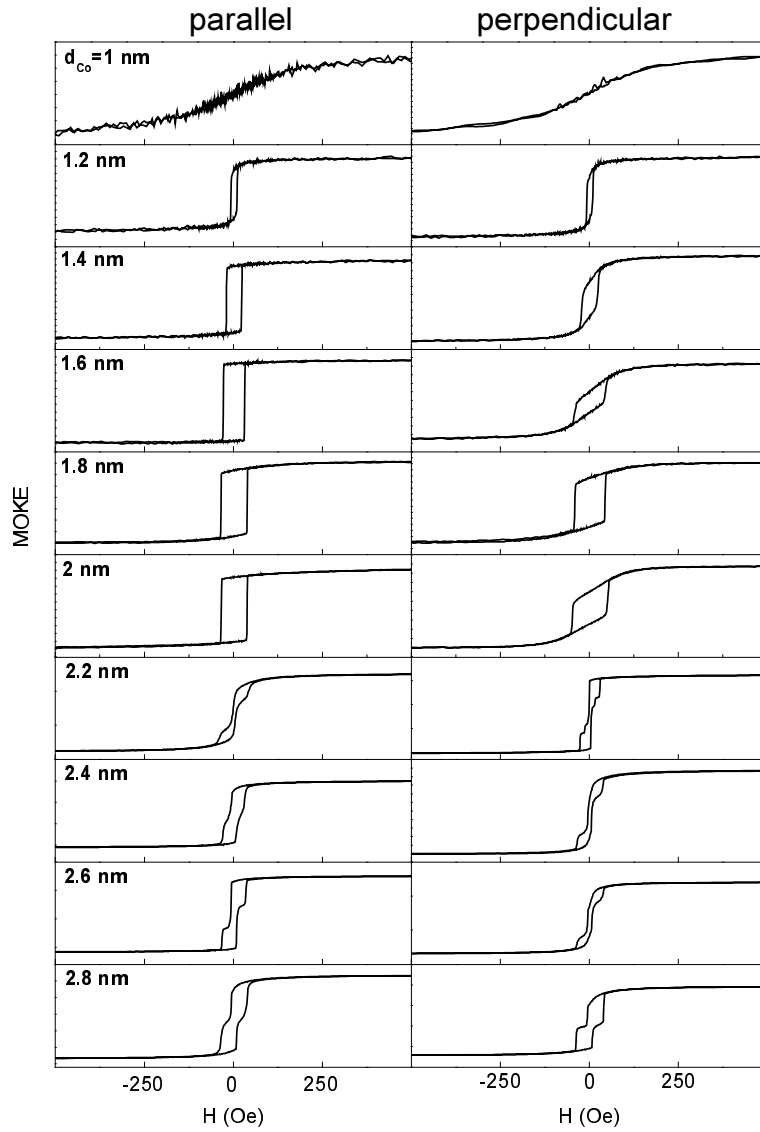
Fig. 9. The examples of $m(H)$ loops measured by MOKE
for two perpendicular magnetic field directions in the sample plane
for $Co(d_{Co})/Si(2.4\ nm)$ for different Co layer thickness

interlayer coupling that modifies the hysteresis loop shapes from square-like to step-like characterized by two "coercive" fields: H_{C1} and H_{C2}. This seems to be confirmed by the $F_{AF}(d_{Si})$ oscillatory dependence presented in Fig. 12a (top panel). Due to a very weak coupling the correct identification of the saturation fields was very difficult. Therefore in Fig. 12b we present the values of H_{C1} and H_{C2} fields as a function of Si
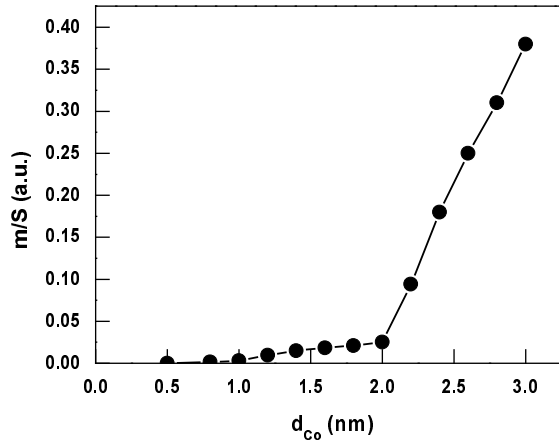
Fig. 10. Co thickness dependence of magnetic moment
per surface area (m/S) of Co/Si Mls with constant $d_{Si} = 2.8$ nm
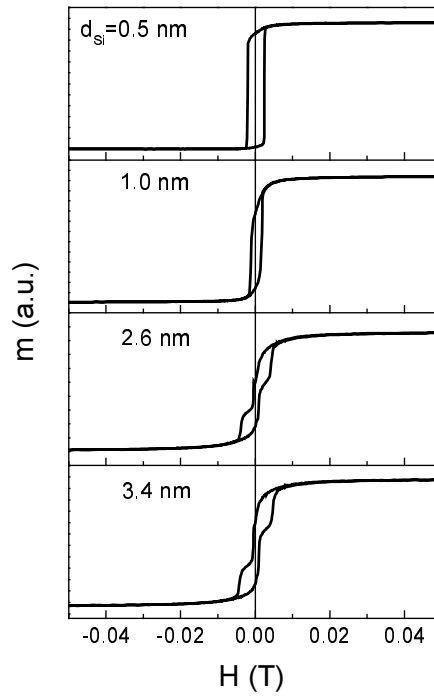
Fig. 11. The evolution of $m(H)$ loop shapes
as a function of Si sublayer thickness
for Co/Si Mls with $d_{Co} = 3$ nm

thickness. From this figure one can see that H_{C2} appears only for thicker Si layers, i.e.,
for $d_{Si} \geq 1.5$ nm. Below this Si thickness only single, almost square-shaped loops ap-

pear. Such $m(H)$ behaviour can be explained by a simple model describing the total magnetic energy of bilayer:

$$E = -M_S H d_{Co} (\cos \varphi_1$$
$$+ \cos \varphi_2) + J \cos(\varphi_1 - \varphi_2)$$
$$+ 0.25 K d_{Co} (\sin^2 \varphi_1 + \sin^2 \varphi_2)$$

where $\varphi_{1(2)}$ are the angles between the applied field H and magnetizations, and J and K denote the interlayer coupling and cubic anisotropy, respectively.
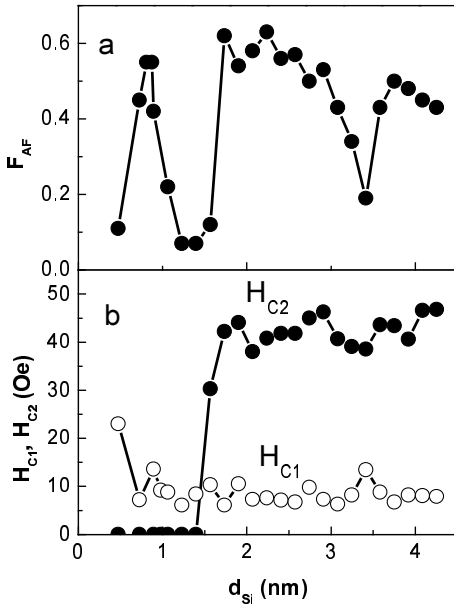
Fig. 12. Si thickness dependence of F_{AF} parameter (a) and two characteristic fields H_{C1} and H_{C2} (b) for Co/Si Mls
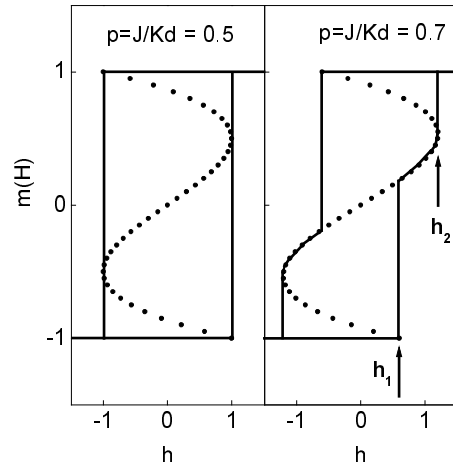
Fig. 13. Visualization of $m(H)$ model hysteresis loop shapes for different coupling to anisotropy J/Kd_{Co} ratios. h_1 and h_2 fields represent spin-flip and spin-flop fields, respectively. The dotted line represents $\partial E/\partial m = 0$ (see text)

It can be shown that for low interlayer coupling, i.e., for $p = J/Kd < 0.5$, the effective exchange coupling is so weak that the anisotropy controls the switching characteristics and as a result square loops appear (Fig. 13). For $0.5 < p = j/Kd < 1$, two characteristic fields emerge: $h_1 = -2(p - 1)$ and $h_2 = 8[(p + 1)/6]^{3/2}$, where $h = HM_S/K$. The dotted line in Fig. 13 represents $\partial E/\partial m = 0$ where $m = \cos(\varphi_1 - \varphi_2)$. Both small value of the F_{AF} parameter and simple square $m(H)$ loops observed for the sample in the vicinity of the first $F_{AF}(d_{Si})$ maximum suggest the presence of the magnetostatic coupling. Its source most probably is in the pinholes formation which reduces the AF exchange coupling in this d_{Si} range. The observed $F_{AF}(d_{Si})$ oscillatory behaviour suggests that the Co–Si nonmagnetic metallic phases replace nominally

pure Si-spacer layers, since the oscillatory behaviour points to the RKKY-like type of interlayer coupling via conduction electrons.

3.3. Application of strongly coupled Fe/Si multilayers

Since the strongest AF interlayer coupling in our Fe(3nm)/Si Mls has been found for d_{Si} = 1.4 nm, it was very interesting to find out whether it can be applied as an artificial antiferromagnet in magnetoresistive (Fe/Si)$_{15}$/Fe/Co1/Cu/Co2 pseudo-spin –valve (PSV) system. We used a Co1/Cu/Co2 trilayer as the magnetoresistive structure with Co1(2) and Cu thicknesses of about 1.5 nm and 2.5 nm, respectively.
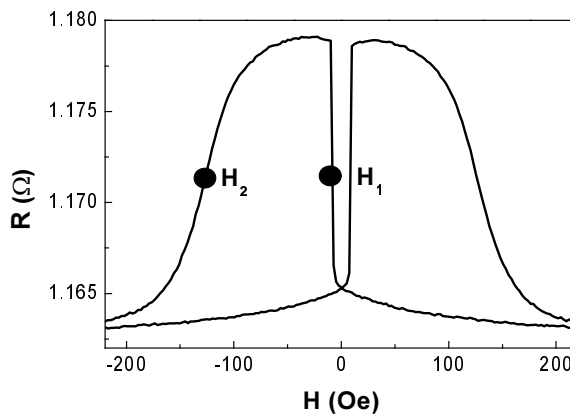
Fig. 14. Magnetoresistance effect of (Fe/Si)$_{15}$/Fe/Co1/Cu/Co2 pseudo-spin–valve system, where Fe/Si Ml was used as an artificial antiferromagnet

Since the last Fe and the Co1 layers are in the intimate contact, the Fe/Co1 bilayer behaves as a first magnetoresistive layer in the examined structure. The field depend-ence of the sample resistance, shown in Fig. 14, reflects a typical PSV giant magnetoresistance behaviour. As can be seen, there are two switching fields: H_1 re-lated to the magnetization reversal of the top Co2 layer and H_2 due to switching of the Fe/Co1 pinned bilayer magnetization to the direction of the external magnetic field at higher fields. Since Fe/Co1 bilayer is AF coupled to the rest of Fe/Si Ml structure, it reverses at higher fields – the top Co2 layer and an AF arrangement between magneti-zations of the Fe/Co1 bilayer and the Co2 layer occurs between H_1 and H_2.

4. Conclusions

Magnetic and structural properties of Fe/Si, Fe/Fe$_{33}$Si$_{66}$ and Co/Si Mls have been examined. For Fe/Si Mls very strong AF coupling (J = −1.93 mJ/m^2) has been found for Si thickness of about 1.4 nm and magnetic moment measurements revealed that

0.25 nm of Fe per single interface is magnetically inactive. The interface structure of Fe/Si Mls, studied by CEMS, suggests that the c-$Fe_{1-x}Si_x$ was formed at the interfaces. Comparing the results obtained for Fe/Si and $Fe/Fe_{33}Si_{66}$ Mls we conclude that the AF coupling is distinctly stronger for nominally pure spacer layer. In both kinds of Mls, only single H_S maximum versus spacer-layer thickness was observed and H_S values decay exponentially above the maximum. For Co/Si Mls a very weak AF coupling and oscillatory $F_{AF}(d_{Si})$ behaviour were observed most probably due to the Co–Si nonmagnetic metallic phases formation replacing nominally pure Si spacer layers. Magnetic moment measurements showed that the growth of the Co on Si occurs in an island-growth mode in contrast to Fe/Si Mls. We have shown that the evolution of magnetic loop shapes can be successfully explained by the interplay between J and Kd.

We have shown that AF coupled Fe/Si Mls can be applied as an artificial antiferromagnet in magnetoresistive pseudo-spin–valve system.

References

[1] GAREEV R.R., BÜRGLER D.E., BUCHMEYER M., OLLIGS D., SCHREIBER R., GRÜNBERG P., Phys. Rev. Lett., 87, (2001), 157202.

[2] GAREEV R.R., BÜRGLER D.E., BUCHMEYER M., SCHREIBER R., GRÜNBERG P., J. Magn. Magn. Mater., 240 (2002), 235.

[3] INOMATA K., SAITO Y., J. Appl. Phys., 81 (1997) 5344.

[4] GRUNDY P.J., FALLON J.M., BLYTHE H.J., Phys. Rev., B62, 9566 (2000).

[5] FALLON J.M., FAUNCE C.A., GRUNDY P.J., J. Appl. Phys., 88, 2400 (2000).

[6] FULLERTON E.E., MATSON J.E., LEE S.R., SOWERS C.H., HUANG Y.Y., FELCHER G., BADER S.D., PARKER F.T., J. Magn. Magn. Mater., 117 (1992), L301.

[7] CHAIKEN A., MICHEL R.P., WALL M.A., Phys. Rev., B 48 (1996), 5518.

[8] DUFOUR C., BRUSON A., MARCHAL G., GEORGE B., MANGIN PH., J. Magn. Magn. Mater., 93 (1991), 545.

[9] STRIJKERS G.J., KOHLHEPP J.T., SWAGTEN H.J.M., DE JONGE W.J.M., Phys. Rev., B 60 (1999), 9583.

[10] HELGASON O., SIFUSSON T.I., Hyperfine Interact., 45 (1989), 415.

[11] MILOSAVLJEVIC M., DHAR S., SCHAAF P., BIBIC N., HUANG Y.-L., STEIBT M., LIEB K.P., J. Appl. Phys., 90 (2001), 4474.

Rotational anisotropy
in exchange-biased NiFe/FeMn bilayers

DO-GUWN HWANG[*]

Department of Computer and Electronic Physics, Sangji University, Wonju 220-702, Korea

The anisotropic magnetoresistance (AMR) model was improved in order to determine the magnitude and direction of the rotational anisotropy in NiFe/FeMn bilayer structures having different thicknesses of the ferromagnetic and antiferromagnetic layers. There are two important parameters in the model, namely the ratios $\alpha = H_{\mathrm{rot}}/H_{ex}$ and $\beta = \theta_{\mathrm{rot}}/\theta_a$, where H_{rot} and θ_{rot} are the effective magnetic field and the angle of the rotational anisotropy and H_{ex} and θ_a are the exchange bias field and the angle of the field applied, respectively. These parameters describe the magnitude and direction of the rotational anisotropy. As the thickness of FeMn layer decreased up to 3.5 nm, the α value increased from about 0.15 to 0.55. This proves that the regions of a weak exchange coupling extended as the antiferromagnetic layer thickness decreases. The parameters α and β almost did not change as the NiFe layer thickness increased from 7 nm up to 15 nm; even though H_{ex} was then reduced from 170 Oe to 70 Oe.

Key words: *exchange biasing; rotational anisotropy; antiferromagnet*

1. Introduction

Exchange anisotropy is a phenomenon arising from the direct exchange coupling at the interface between a ferromagnet (FM) and an antiferromagnet (AF). The best-known property arising from this anisotropy is a shift in the hysteresis loop of a ferromagnet. The field by which the loop is shifted is defined as the exchange-biasing field H_{ex} [1]. To explain such a behaviour theoretically, several models focused on the domain structure of the AF layer for compensated and uncompensated interfaces were proposed in which a single domain state or uniform magnetization of the FM layers was assumed [2]. Although these theories can explain the magnitude of the loop shift in polycrystalline bilayers, they fail to account for the enhanced H_C and a non-vanishing rotational hysteresis in high magnetic fields due to instability in the polycrystalline AF layer [3]. Recent models suggested that there are stable AF grains,

---

which contribute to the unidirectional anisotropy, and unstable ones, which cause the rotational anisotropy [4, 5]. Magnetic domain observations in the AF/FM bilayers allowed concluding that the strength of H_{ex} varies at the microscopic scale across the sample [6].

In this work, we improved the AMR model introduced by Dahlberg et al. [7, 8] to determine the magnitude and direction of rotational anisotropy in the FeMn/NiFe and NiO/NiFe structures with a varying thickness of the AF layer. In our model, there are two important parameters of α and β, which represent the magnitude and the angle of rotational anisotropy. The influence of the applied magnetic field H_a on the parameters of the bilayer structures was also investigated.

2. Experimental

The bilayer films of NiFe (10 nm)/FeMn (3.5–20 nm) and NiFe (7–15 nm) /FeMn (20 nm) were deposited at a room temperature onto a Corning glass 7059 in an ion beam sputtering system. The base pressure was below 4.5×10^{-9} Torr. The ion gun was a 3-cm Kaufmann source using Ar gas at the pressure of 1.1×10^{-4} Torr. Ion beam voltage and current during deposition were equal to 800 V and 6 mA, respectively, and the thickness was monitored by a quartz set-up. An aligning field of 300 Oe was applied during the deposition of the ferromagnetic layers to induce uniaxial anisotropy. The magnetic properties were characterized considering the measured anisotropic magnetoresistance (AMR) curves in a 4-point terminal configuration.

The AMR curves varied in their shapes with the applied magnetic field. Particularly, the curves obtained at moderate fields close to H_{ex} have more complex shapes than those obtained at low and high magnetic fields. However, the AMR curve measured in the vicinity of $H_a = H_{ex}$ should be analyzed to understand better the phenomenon of rotational anisotropy in the biased bilayer structure. Three intensities of the applied field, namely $H_a = 0.5H_{ex}$, H_{ex} and $2H_{ex}$, were selected to compare the ratio of rotational and unidirectional anisotropy in the bilayers exhibiting different H_{ex}.

3. Results and discussion

Figure 1 shows the vector representation of our model, in which the rotational anisotropy is reflected by the effective anisotropy field H_{rot}. This field varies with the amplitude of H_a in both its strength and direction during AMR measurement, whereas the magnitude and direction of H_{ex} are fixed. Considering this representation, the magnetic energy density of the ferromagnetic layer in the field applied can be written as

$$E = -H_{ex}M\cos(\theta - \theta_{ex}) - H_{rot}M\cos(\theta - \theta_{rot}) - H_aM\cos(\theta_a - \theta) \qquad (1)$$

where M is the magnetization of the FM layer, and θ_{ex}, θ_a and θ_{rot} are the angles defining directions of H_{ex}, H_a, and H_{rot}, respectively. In Eq. (1), the demagnetizing

energy is neglected, because it was calculated that the demagnetizing field is smaller than 0.5 Oe for the geometry of the samples used. From the condition of the minimum total energy in the equilibrium state, we can determine the angle θ defining the orientation of the magnetization M. The resistance R of the bilayers is given by

$$R = R_0 + \Delta R \cos^2(\theta - \theta_a) \tag{2}$$

where R_0 is the resistance at $H_a = 0$ and ΔR is the change of resistance due to the AMR effect. Therefore, the AMR follows on the behaviour of $\cos^2\theta$ at $\theta_a = 0$.
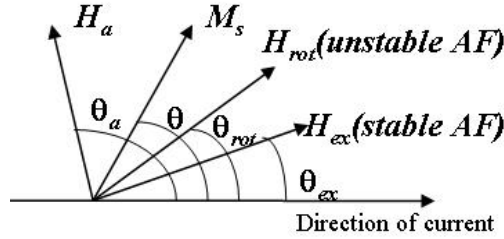
Fig. 1. Vector representation of the model

Minimizing the energy given by Eq. (1) and carrying out some algebraic transformations, one obtains

$$\cos^2\theta = \frac{\left[1 + \alpha\cos\beta\theta_a + \left(\dfrac{H_a}{H_{ex}}\right)\cos\theta_a\right]^2}{\left[1 + \alpha\cos\beta\theta_a + \left(\dfrac{H_a}{H_{ex}}\right)\cos\theta_a\right]^2 + \left[\{\alpha\sin\beta\theta_a + \left(\dfrac{H_a}{H_{ex}}\right)\sin\theta_a\right]^2} \tag{3}$$

where two introduced parameters $\alpha = H_{\rm rot}/H_{ex}$ and $\beta = \theta_{\rm rot}/\theta_a$.

Figure 2 shows the experimental points of AMR and the fitting curves as a function of the field applied and FeMn layer thickness in the NiFe(10 nm)/FeMn(4.2, 5, 14 nm) bilayers. As was mentioned earlier, the measurements were carried out at the field applied equal to $0.5H_{ex}$, H_{ex}, and $2H_{ex}$. At the field high enough, the AMR curve is symmetric, displaying two equal minima at 90 and 270 deg. These minima shift towards each other as H_a decreases, reaching $2H_{ex}$ (Fig. 2c). With a further decrease of the field, this shift becomes more pronounced and also a decrease of the central maximum is noticed (Fig 2b). As the field applied reaches a low intensity, the second minimum rises and the curve becomes asymmetric (Fig. 2a). At a very low field the curve becomes eventually periodic again [8]. The maximum peak shifts slightly to higher angles as the FeMn layer thickness decreases. All the AMR data of the FeMn bilayers were well fitted by Eq. (3), except the ones obtained at the low field for the FeMn (3.5 nm) bilayer which exhibited large coercive field.
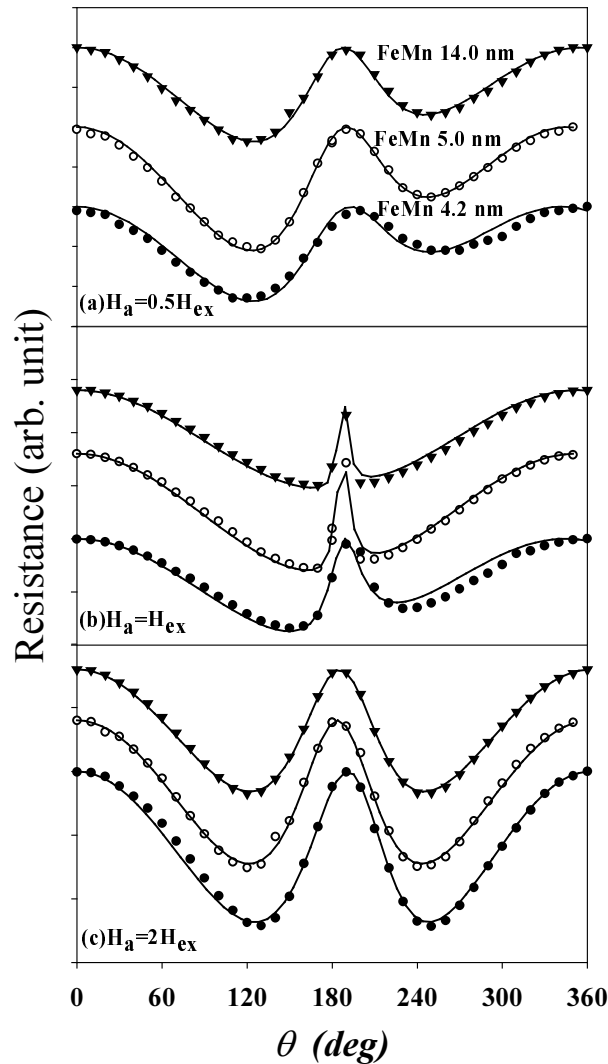
Fig. 2. Experimental dependencies of AMR on the direction
of magnetic field of different strength related to bilayer structures
of various thickness of FeMn layer (4.2 nm – solid circle;
5 nm – open circle; 14 nm – solid triangle).
Solid lines – fits to experimental points

Figure 3 shows the dependence of the α and β ratios on the FeMn-layer thickness with H_a as the parameter. The measured H_{ex} is also shown in this figure as a function of thickness. The α ratio for all H_a increases from about 0.15 to 0.55 with a decrease of the AF-layer thickness in its range of 3.5–14 nm. In the range of above 5 nm, the value of AMR almost does not change. The observed behaviour of the AMR curves confirms the expectation that a number of unstable AF grain, which account for rota-

tional anisotropy, increase as the AF-layer thickness decreases. The AMR curve for the 3.5 nm FeMn-bilayer measured at $H_a = 0.5H_{ex}$ cannot be fitted to Eq. (3). Since our model did not present the information on the hysteresis loss, the bilayer having high coercive field cannot be fitted. For example, the NiO(10, 30 nm)/NiFe(10 nm) bilayers have noticeably higher coercive field than NiFe/FeMn bilayer, therefore the measured AMR curves are not fitted at the central maximum peak.
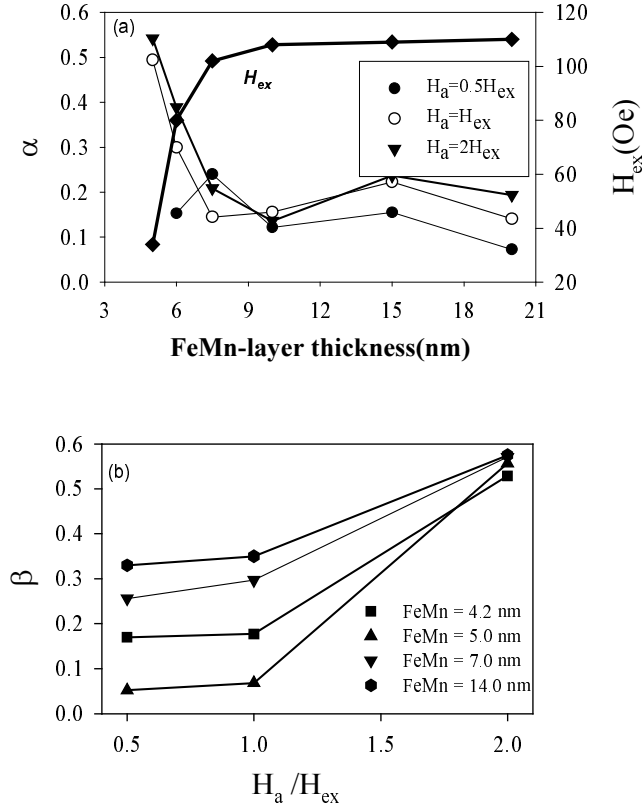
Fig. 3. Dependencies of measured exchange anisotropy field H_{ex} and calculated parameter α on the thickness of FeMn layer at various strengths of the applied field (a); dependence of the parameter β on H_a/H_{ex} at various thicknesses of FeMn layer (b)

The $\beta = \theta_{rot}/\theta_a$ means that the direction of rotational anisotropy lagged behind that of H_a. This ratio increases with H_a, as is shown in Fig. 3b. It is quite obvious that the direction of the rotational anisotropy strongly depends on the applied field. However, the β ratio was independent of the AF layer thickness.

Figure 4 shows the dependence of calculated α and β on the thickness of NiFe layer. As the NiFe thickness increases from 7 nm to 15 nm, H_{ex} decreases from 170 Oe to 70 Oe. However, α and β did not show any dependence. For all the exchange biased

systems, H_{ex} is inversely proportional to the thickness of FM layer, because exchange bias is an interface effect. Although H_{ex} decreases with the FM layer
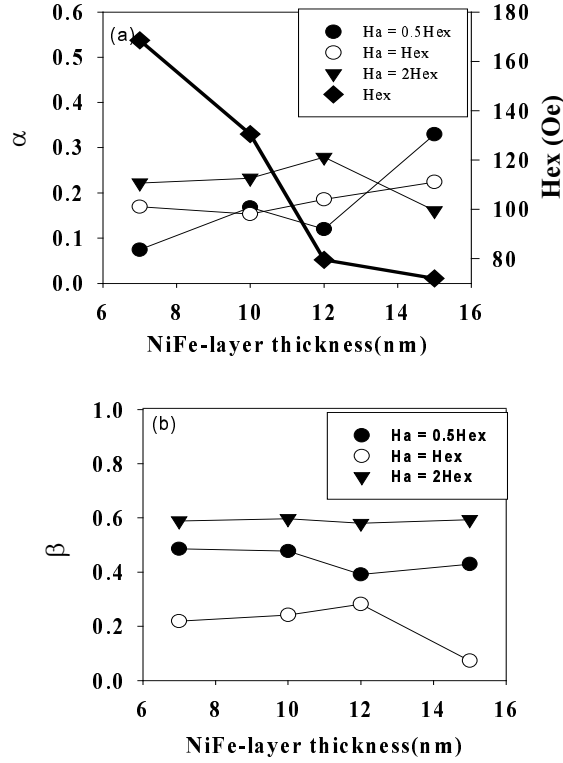
Fig. 4. Dependencies of measured exchange anisotropy field H_{ex}
and calculated parameter α on the thickness of NiFe layer
at various strengths of the field applied (a); dependence
of the parameter β on H_a/H_{ex} at various thicknesses of NiFe layer (b)

thickness, the stable AF grains generating the exchange anisotropy at interface do not change. Therefore, the α and β ratios do not depend on the FM layer thickness, but only do on the stability of AF layer.

4. Conclusions

We have improved the AMR model introducing the parameters α and β which express the magnitude and direction of the rotational anisotropy in the exchange biased bilayers of different thickness of the AF-layer. From the calculated values of these parameters, we found the relative magnitude of the rotational anisotropy, which increased from 15% to 55% of the exchange anisotropy with a decrease of the AF-layer

thickness. We also proved that its direction lagged behind the direction of the field applied by an angle less than a half of θ_a. As the thickness of ferromagnetic layer increased, the α and β parameters practically did not change. These parameters can explain the properties of rotational anisotropy due to unstable AF grains. However, the model cannot be applied to the bilayer structures exhibiting large hysteresis losses and large coercivity. Further modifications of the model are needed and such an attempt has already been undertaken.

References

[1] MEIKLEJOHN W.H., BEAN C.P., Phys. Rev., 102 (1956), 1413.
[2] BERKOWITZ A.E., TAKANO K., J. Magn. Magn. Mat., 200 (1999), 552.
[3] TAKAHASHI M., YANAI A., TAGUCHI S., SUZUKI T., J. Appl. Phys., 19 (1980), 1093.
[4] STILES M.D., MCMICHAEL R.D., Phys. Rev. B, 59 (1999), 3722.
[5] FUJIWARA H., HOU C., SUN M., CHO H.S., NISHIOKA K., IEEE Trans. Magn., 35 (1999), 3082.
[6] CHOPRA H.D., YANG D.X., CHEN P.J., BROWN H.J., SWARTZENDRUBER L.J., EGELHOFF W.F. Jr., Phys. Rev., B61 (2000), 15312.
[7] GREDIG T., KRIVOROTOV I.N., MERTON C., GOLDMAN A.M., DAHLBERG E.D., J. Appl. Phys., 87 (2000), 6418.
[8] BROWN H., DAHLBERG E.D., HOU C., J. Appl. Phys., 89 (2001), 7543.

Exchange coupling field in top, bottom, and dual-type IrMn spin valves coupled to CoFe

J. Y. HWANG, J. R. RHEE[*]

Department of Physics, Sookmyung Women's University, Seoul 140-742, Korea

A comparative study of $Co_{75}Fe_{25}/Ir_{22}Mn_{78}$ exchange biased top, bottom, and dual-type spin valves is presented. IrMn pinned spin valves were prepared by dc magnetron sputtering onto thermally oxidized Si (111) substrates at a room temperature under a magnetic field of about 100 Oe. For as-deposited top-type spin valves, the magnetoresistance (MR) ratio and exchange coupling field (H_{ex}) were 5.6% and 430 Oe, respectively. For bottom IrMn based spin valves, the H_{ex} values are much higher ($H_{ex} = 1180$ Oe) while MR ratio (3.6%) is reduced with respect to the top spin valves. The blocking temperatures (T_B) of the top and bottom SV were 250 ºC and 270 ºC, respectively. The results concerning magnetic properties together with structural investigations suggest that H_{ex} is mainly dependent on the quality of fcc (111) crystalline texture while MR ratio is sensitive to both crystalline texture and interface roughness. Dual-type spin valves, with the MR ratio of 7.6% and H_{ex} of 850/510 Oe, showed two exchange loops due to the differences in H_{ex} between the top and bottom pinning layers.

Key words: *spin valve; exchange coupling field; MR ratio; blocking temperature; crystalline texture*

1. Introduction

Various antiferromagnetic (AFM) materials have been investigated in order to obtain higher thermal stability [1, 2] and reliability of the pinned layer for use in spin valve (SV) giant magnetoresistance (GMR) heads in high-density magnetic recording [1, 3, 4]. IrMn has been identified as a promising AFM material for SV due to its high exchange coupling field (H_{ex}), high blocking temperature (T_B), and low critical thickness (~80 Å) [5, 6]. Therefore, exchange coupled IrMn (~80 Å)/CoFe bilayer is suitable for narrow gap head structure [3, 7], since IrMn shows a high H_{ex} at smaller layer thickness than other ordered AFM films, such as NiMn and PtMn [1, 8].

In this paper, we present a fabrication method of $Co_{75}Fe_{25}/Ir_{22}Mn_{78}$ exchange coupled top SV (TSV), bottom SV (BSV) and dual SV by dc magnetron sputtering. We

_____

[*]Corresponding author, e-mail: jrrhee@sookmyung.ac.kr.

focus on SV performance around the optimal IrMn thickness (~100 Å). The effect of cyclic annealing treatments on the magnetic, magnetoresistive, and structural properties of the devices has also been investigated.

2. Experimental

The GMR/SV films with the structures of top $Ta45/Ni_{80}Fe_{20}30/Co_{75}Fe_{25}20/Cu30$ $/Co_{75}Fe_{25}t/Ir_{22}Mn_{78}100/Ta45$, bottom $Ta45/Ni_{80}Fe_{20}20/Ir_{22}Mn_{78}100/Co_{75}Fe_{25}t/Cu30/Co_{75}$ $Fe_{25}20/Ni_{80}Fe_{20}30/Ta45$, and dual $Ta45/Ni_{80}Fe_{20}20/Ir_{22}Mn_{78}100/Co_{75}Fe_{25}t/Cu30/Co_{75}$ $Fe_{25}20/Ni_{80}Fe_{20}30/Co_{75}Fe_{25}20/Cu30/Co_{75}Fe_{25}t/Ir_{22}Mn_{78}100/Ta45$ (all thicknesses are given in angstroms) were deposited at a room temperature by the dc magnetron sputtering on thermally oxidized Si (111) substrates in a magnetic field of about 100 Oe. In BSV and dual SV, a $Ta/Ni_{80}Fe_{20}$ bilayer was used as a seed layer to obtain the exchange biasing of the overlaying CoFe by IrMn. The base pressure of the process was below 2×10^{-8} Torr and the argon (99.9995%) gas pressure was 2 mTorr. The deposition rates of IrMn, CoFe, and NiFe layers were 0.5~1 Å/s. The crystal structures were investigated by X-ray diffraction (XRD) (CuK_{α} line). In order to induce large H_{ex} between the IrMn layer and the pinned CoFe layer, a series of annealing cycles was applied under a static magnetic field of 1050 Oe in vacuum furnace with the pressure of 5×10^{-7} Torr. Each annealing cycle consisted of a 1-hour ramp to 250 °C, a 1-hour isothermal annealing at 250 °C and a 1-hour cooling down to a room temperature. The $\Delta R/R$ (MR ratio) was measured by the four-point method at a room temperature, with the magnetic field applied along the direction of H_{ex}. The magnetization curves were measured by a vibrating sample magnetometer (VSM). Atomic force microscopy was used to measure the surface roughness.

3. Results and discussion

3.1. Pinned layer thickness dependence of H_{ex} and MR ratio

Figure 1 demonstrates the pinned CoFe film thickness dependence of H_{ex} and MR ratio for both TSV and BSV annealed at 250 °C for 2 h. The MR ratios of TSV and BSV increase with increasing CoFe pinned layer thickness. The hyperbolic H_{ex} (t_{CoFe}) dependence indicates that IrMn/CoFe bilayers approximately follow the common equation [9] $H_{ex} = J/(M_s \times t)$, where J is interfacial exchange coupling energy, M_s and t are the saturation magnetization and the film thickness of the pinned ferromagnetic layer, respectively. In the remainder of this paper, pinned layer thickness of 12 Å will be applied for all SV.
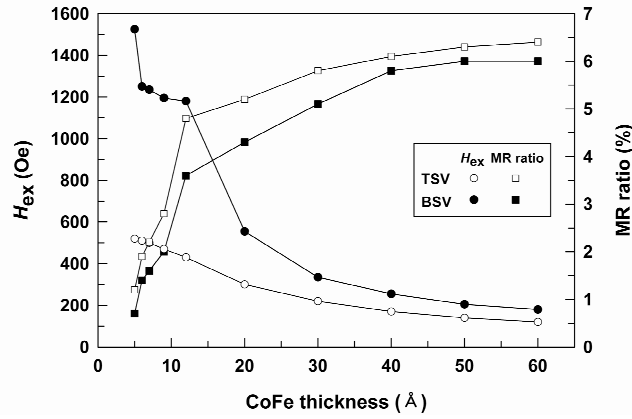
Fig. 1. The pinned CoFe film thickness dependence
of the H_{ex} and MR ratio for TSV
and BSV after the second annealing

3.2. Structural properties

Typical SV performances with an optimal IrMn thickness of 100 Å are shown in the table. In the as-deposited state, TSV shows a higher MR ratio than BSV system, it exhibits however a poor H_{ex}. For TSV, the annealing for 2 h at 250 $^{\circ}$C in vacuum results in an improvement of H_{ex}, while MR ratio is slightly reduced. For BSV, the annealing results in a higher H_{ex} and MR ratio, with H_{ex} being much higher and MR ratio being reduced compared to TSV. Dual SV with MR ratio of 7.6% shows two exchange loops, one at a lower field due to pinning on the top side and a second loop at a higher field due to the bottom side pinning.

Table. Spin-valve parameters for the TSV, BSV, and dual SV
evaluated (optimal IrMn thickness of 100 Å)

Spin Valve	R_s (Ω/sq.)	$\Delta R/R$ (%)	H_{ex} (Oe)	H_c (Oe)	H_{int} (Oe)
Top as-deposited	15.26	5.8	380	126	8.5
Top annealed	15.79	5.6	430	100	7.0
Bottom as-deposited	17.38	2.7	680	325	10.5
Bottom annealed	17.16	3.6	1180	150	12.0
Dual annealed	14.32	7.6	850/510	175/140	15.5

Figures 2a, 2b show the X-ray diffraction patterns of the samples: as-deposited and after annealing (two cycles) for the TSV and BSV, respectively. In these figures, we see the preferential (111) peak of the fcc-ordered IrMn accompanied by a peak attributed to the (111) of NiFe and the possible contributions from the (111) of Cu and CoFe. For the as-deposited TSV structure, lattice constants of a = 3.83 Å and 3.62 Å were

obtained from IrMn and CoFe/Cu/ CoFe/NiFe fcc (111) peak positions. For the annealed TSV, an increase in fcc (111) peak intensity indicates an improvement of the crystalline texture induced by annealing. The decrease of the MR ratio may be attributed to higher sheet resistance (R_s) due to interdiffusion, while the higher H_{ex} results from the improved (111) crystalline structure.
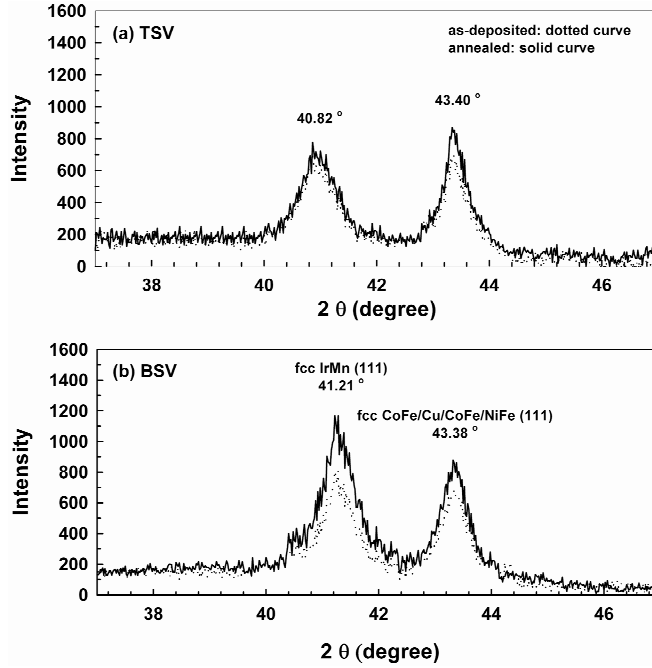
Fig. 2. X-ray diffraction scan patterns for the TSV (a) and BSV (b)
in the as-deposited state and after the second annealing

The IrMn (111) peak of annealed BSV shows a higher intensity and a higher 2θ position (a = 3.79 Å) than TSV, while the CoFe/Cu/CoFe/NiFe (111) peak position is unchanged. This indicates a higher perfection of the crystalline texture of IrMn layer in BSV than in TSV structures. In the TSV structure, the IrMn layer grows over a thicker and rougher underlayer of Ta/NiFe/CoFe/Cu/CoFe/NiFe with cumulative roughness [10] which reduces the IrMn texture and a larger average d spacing with a = 3.83 Å.

In contrast to the TSV case, the IrMn layer of BSV has a superior, more compact fcc (111) texture due to its growth on a thin and smooth underlayer of Ta45/NiFe20. The texture of IrMn layer can be further improved by annealing, leading to a more bulk-like microstructure and to higher H_{ex} values. However, since the CoFe/Cu/ CoFe/NiFe layers grow on the rougher IrMn surface with reduced grain size [10, 11] as seen in the (111) peak widths, this leads to a higher R_s, lower MR ratio due to more efficient grain boundary scattering, and a larger H_{int}, interlayer coupling field, compared to the TSV structure.

3.3. Magnetic and MR properties

Magnetic hysteresis loops and major MR curves measured parallel to an easy axis of the BSV structure are shown in Figs. 3 and 4 for as-deposited and annealed (two cycles) samples, respectively. The values of H_{ex} and coercivity (H_c) of the pinned layer of annealed BSV are found to be 1180 Oe and 150 Oe, respectively. A corresponding result is obtained from the major MR curve of Fig. 4a. The room temperature H_{ex} of the BSV film annealed at 250 °C for 2 h was about twice that of the as-deposited one.
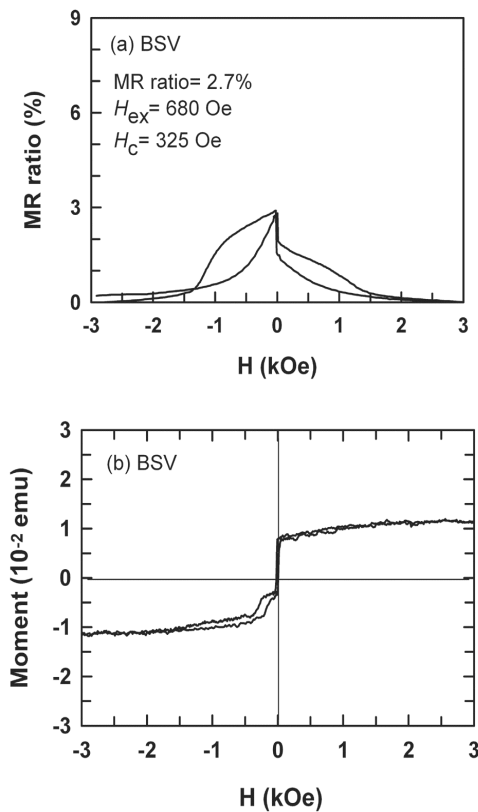
Fig. 3. Major MR (a) and magnetization (b) curves for as-deposited BSV
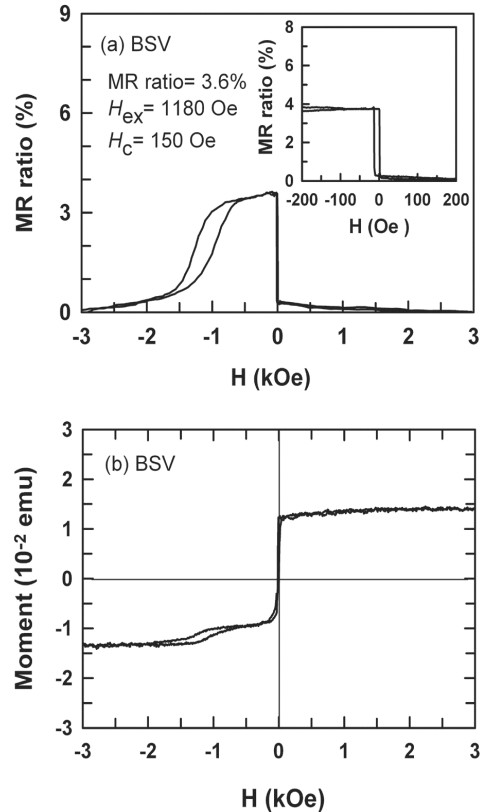
Fig. 4. Major MR (a) and magnetization (b) curves for BSV after the second annealing. The inset in (a) shows minor MR curve

From the minor MR curve (inset in Fig. 4a), it is found that the interlayer coupling field (H_{int}) between the free layer and the pinned layer is about 12 Oe, and the coercive field of the free layer is 5 Oe. In addition, we note that the pinned layer, which is critical for the operation of an SV head, shows stable MR properties. There is no change in its behaviour caused by the fields applied up to about 600 Oe.
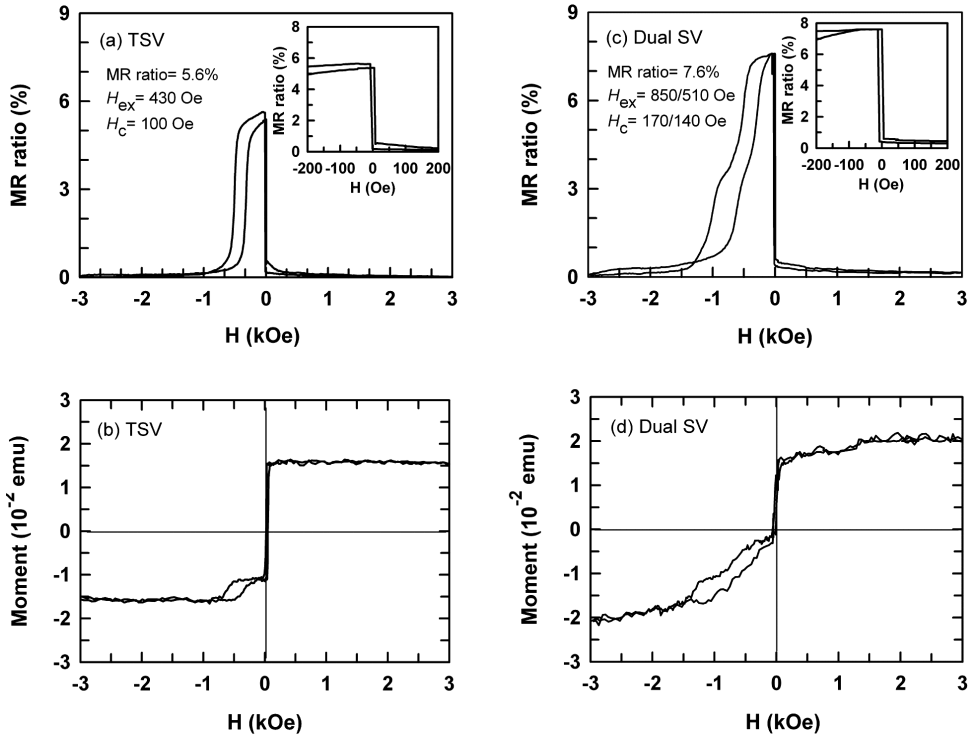
Fig. 5. MR (a) curves and magnetization curves (b) for TSV annealed at 250 °C for 2h,
(c) and (d) – dual SV. The insets in (a) and (c) show minor MR curves

Figure 5 shows the MR and magnetization curves for TSV and dual SV annealed at 250 °C for 2h. The TSV shows a higher MR ratio and lower H_{ex} value. Dual SV, with MR ratio of 7.6% and H_{ex} of 850/510 Oe, shows two exchange loops due to the difference in the H_{ex} between the top and bottom pinned layers.

3.4. Varying the number of annealing cycle

Figure 6 shows the dependence of H_{ex} and MR ratio of the BSV and TSV on the number of annealing cycles. The as-deposited sample shows H_{ex} of 680 Oe and MR ratio of 2.7% for BSV, H_{ex} of 380 Oe and MR ratio of 5.8% for TSV. The H_{ex} and MR ratio of TSV decrease gradually with the number of annealing cycles. For the BSV after one annealing cycle, the H_{ex} and MR ratio increase to about 1180 Oe and 4.3%, respectively. After the second annealing cycle, the MR ratio decreases to 3.6%, and the curves become relatively stable with H_{ex} values of 1180 Oe.

3.5. Thermal stability

For application in SV read head, the H_{ex} should be greater than 300 Oe, and H_{ex} and MR ratio should not be affected by the temperature of 200 °C during device pro-

duction, or temperature from 200 ºC to 250 ºC produced by electrostatic discharge or sensing current during device operation [12, 13]. This points out the importance of temperature dependence of the H_{ex}. Figure 7 shows the temperature dependence of H_{ex} for TSV and BSV previously subjected to two annealing cycles. The H_{ex} of TSV
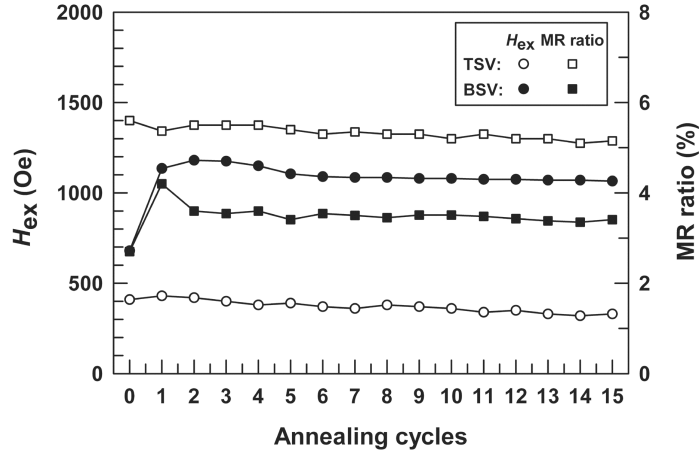
Fig. 6. Annealing cycle dependence of
H_{ex} and MR ratio for the BSV and TSV
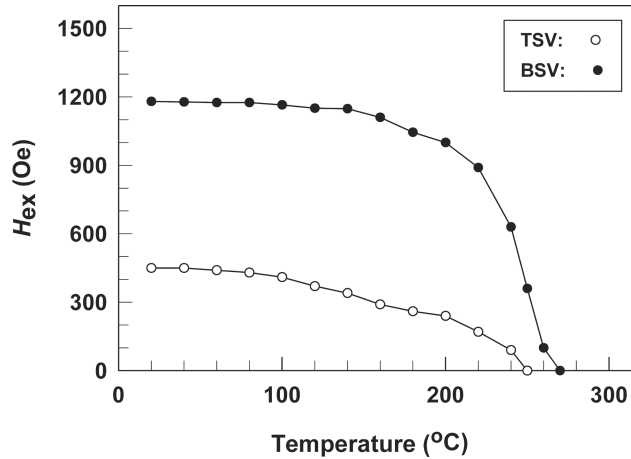
Fig. 7. Temperature dependence of the H_{ex}
for the BSV and TSV after the second annealing cycle

decreases gradually with the temperature increase, reaching zero at 250 °C. The H_{ex} of BSV remains constant at 1180 Oe up to 140 ºC, and then falls to zero at 270 ºC. In particular, the BSV (CoFe spin valves with IrMn) exhibits a higher blocking temperature of 270 °C, and a MR ratio of 3.6%, and an H_{ex} of 1180 Oe, which is the highest ever reported for other post-annealing AFM films, such as NiMn and PtMn [1, 8].

4. Conclusions

Top, bottom, and dual IrMn-based SV were investigated. The BSV shows a lower MR ratio and a higher H_{ex} than the TSV. The high H_{ex} has been attributed to a better IrMn (111) texture with smaller lattice constant ($a = 3.79$ Å). The reduced MR ratio is attributed to rougher interfaces in the CoFe/Cu/CoFe/NiFe layers with reduced grain size due to a rougher IrMn surface. This interpretation is based on an assumption that H_{ex} depends mainly on the degree of fcc (111) texture, while MR ratio is sensitive to both crystalline texture and interface roughness. Both BSV and TSV structures withstand thermal treatments up to above 250 ºC. The pinning field of the BSV remains constant up to 140 ºC and then decreases to zero at the blocking temperature of 270 ºC, while the pinning field of the TSV decreases gradually and falls to zero at 250 ºC. These results suggest that the MR ratios of SV can be enhanced by optimizing the thickness of pinned and free layer for the application of GMR/SV sensor with high thermal stabilities.

References

[1] MAO S., GANGOPADHYAYM S., AMIN N., MURDOCK E., Appl. Phys. Lett., 69 (1996), 3593.
[2] CHOI K.L., KIM K.M., LEE N.I., KIM M.Y., RHEE J.R., LEE S.S., HWANG D.G., PARK C.M., IEEE Trans. Magn., 35 (1999), 2943.
[3] FUKE H.N., SAITO K., KAMIGUCHI Y., IWASAKI H., SAHASHI M., J. Appl. Phys., 81 (1997), 4004.
[4] VAN DER HEIJDEN P.A.A., MAAS T.F.M.M., JONGE W.J.M., KOOLS J.C.S., ROOZEBOOM F., ZAAG P.J., Appl. Phys. Lett., 72 (1998), 492.
[5] IWASAKI H., SAITO A.T., TSUTAI A., SAHASHI M., IEEE Trans. Magn., 33 (1997), 2875.
[6] DEVASAHAYAM A.J., SIDES P.J., KRYDER M.H., J. Appl. Phys., 83 (1998), 7216.
[7] FUKE H.N., SAITO K., YOSHIKAWA M., IWASAKI H., SAHASHI M., Phys. Lett., 75 (1999), 3680.
[8] WONG B.Y., MITSUMATA C., PRAKASH S., LAUGHLIN D.E., KOBAYASHI T., IEEE Trans. Magn., 32 (1996), 3425.
[9] LINN T., TSANG C., FONTANA R.E., MAURI D., HOWARD J.K., IEEE Trans. Magn., 31 (1995), 2585.
[10] KOOLS J.C.S., KULA W., MAURI D., LIN T., J. Appl. Phys., 87 (1999), 4466.
[11] ANDERSON G., HUAI Y., MILOSLAWSKY L., J. Appl. Phys., 87 (2000), 6989.
[12] KOS A.B., RUSSEK S.E., KIM Y.K., CROSS R.W., IEEE Trans. Magn., 33 (1977), 3541.
[13] CROSS R.W., KIM Y.K., OTI J.O., RUSSEK S.E., Appl. Phys. Lett., 69 (1996), 3935.

Magnetometry of monoatomic layers and spin electronics elements

JERZY WRONA[*], TOMASZ STOBIECKI, MACIEJ CZAPKIEWICZ, ROBERT RAK

Department of Electronics, University of Mining and Metallurgy,
al. Mickiewicza 30, 30-059 Krakow, Poland

Two magnetometers: resonance vibrating sample magnetometer (R-VSM) and magnetooptical Kerr effect magnetometer (MOKE) designed for the measurements of hysteresis loops of ultra-thin films and spintronics elements are described. Both instruments have been built by the first author of this paper in the Department of Electronics. The measuring head of R-VSM is universal and can work in the Helmholtz coils as well as in an electromagnet. The frequency of R-VSM is about 75 Hz. Test measurements on MgO (001)/Fe (4, 3, and 2 ML)/50 Å Cr samples were performed and the sensitivity was estimated as 10^{-5} emu. The MOKE system with a differential amplifier (in contrast to lock-in detection technique) is especially recommended for rapid measurements up to 1.5 kHz. The calibration of the Kerr rotation angle was performed on the standard Fe-sputtered films (with thickness from 2 nm to 50 nm) and Fe-wedge sample, prepared by MBE-technique, within the range of thickness from 1 ML to 50 ML of Fe. Based on the measurement of 2, 3, 4, 5, 7 ML of Fe, the angle resolution of Kerr rotation was estimated as 0.001 min. The example measurement of hysteresis loop on the spin valve structure Si (100) Ta (52 Å)/Co(44 Å)/Cu (22 Å)/Co (44 Å)/FeMn (100 Å)/Ta (52 Å) is demonstrated.

Key words: *magnetometry; vibration sample magnetometer (VSM); magnetooptical Kerr effect (MOKE); magnetic monoatomic layers; spin electronics*

1. Introduction

Multilayers in the form of artificial superlattices in the range of thickness of several monoatomic layers consisting of different magnetic materials (e.g., soft or hard ferromagnets, antiferromagnets, semiconductors, insulators) form spin-nanosystems which may be applied as magnetoelectronic devices: cells of magnetic random access memory (M-RAM) [1], sensors [2] or read heads in hard disk drives [3]. Such very thin films deposited onto diamagnetic or paramagnetic substrate, where the volume of the ferromagnetic material is much smaller than the volume of the substrate, require

---

[*]Corresponding author, e-mail: wrona@agh.edu.pl.

very sensitive instruments and precise methods for measurement of hysteresis loops. In this paper, we demonstrate the construction and test measurements of two very highly sensitive magnetometers: resonance vibrating sample magnetometer (R-VSM) [4] and magnetooptical Kerr effect (MOKE) magnetometer [5]. Both arrangements, which were recently built in the Department of Electronics of the University of Mining and Metallurgy, are characterized by low-cost and sophisticated electronics solutions. We also show that for obtaining full information on magnetization reversal process in magnetic multilayers, both magnetometers should be used, because the methods are complementary. R-VSM measurements deliver information about averaged magnetization process from the whole volume of the sample, whereas magnetooptical information from MOKE magnetometer is local, limited by light-beam spot and penetration depth (for metals it is about 200 Å with an exponential decay).

2. Magnetometer R-VSM

The idea of R-VSM is based on the Faraday induction law and the original Foner solution [6] adopted for measurements of ultra-thin films. There are the following main advantages of R-VSM in relation to the Foner's VSM: the sample oscillates (with a maximum amplitude of 1 mm) parallel to the direction of external magnetic field, therefore it is always in the region of homogeneous field (in the Foner's VSM, the sample vibrates perpendicularly to the direction of external magnetic field), a configuration of pick-up coils in the form of small Smith coils is more favourable [7] than two pairs of pick-up coils connected adversely as in conventional Foner's VSM.

The block diagram of R-VSM is shown in Fig. 1. The magnetic thin film is attached to the end of a glass pipe-rod oscillating with the mechanical resonance frequency of the rod–sample system. The oscillations are forced by a piezoelectric transducer attached to the head (A). The piezoelectric transducer works far from its own resonance, in our case with the frequency equal approximately to 75 Hz. The sample placed in the magnetic field, produced by Helmholtz coils or electromagnet (B), oscillates between pick-up coils (C) inducing a signal which is transferred to the differential input of the lock-in amplifier. The capacity sensor (for electronics details see e.g. [8] or contact directly the first author) of the sample position (E) delivers the signal proportional to the amplitude of sample oscillations and supplies the voltage to the electronic system which generates a reference signal, further provided to the reference input of the lock-in amplifier. The output of digital-to-analog converter (DAC_{1out}) and digital output (D_{1out}) of the lock-in amplifier control the current flowing through the electromagnet and its direction, respectively.

The teslameter (Htm-11n), using a Hall sensor, measures magnetic field and the voltmeter measures the amplitude of the reference signal. The signal from the pick-up coils, detected by the lock-in amplifier, is measured as a function of the magnetic field and allows one to obtain the hysteresis loop of the examined sample.
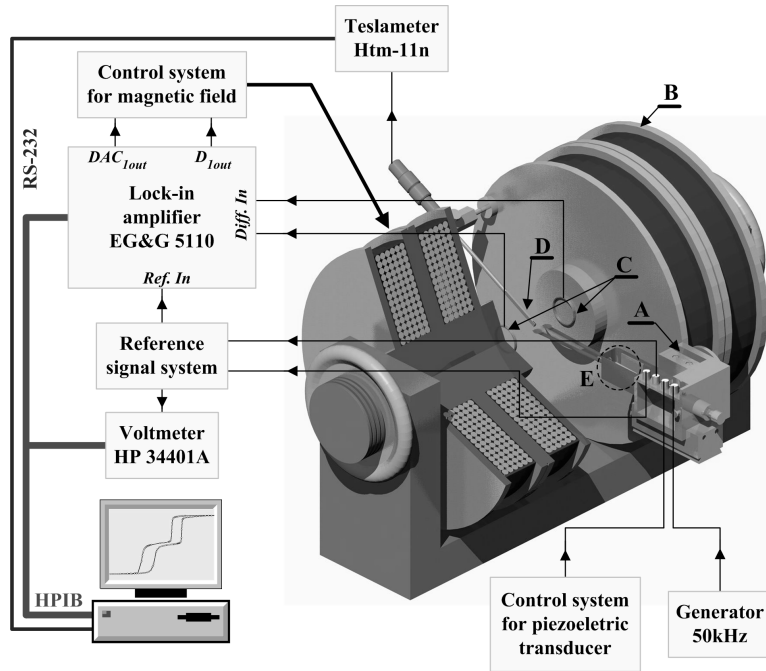
Fig. 1. Block diagram of R-VSM; A – head, B – electromagnet,
C – pick-up coils, D – Hall sensor, E – capacity sensor of position

For harmonic oscillations of the sample, the signal e induced in the pick-up coils is proportional to the amplitude of oscillations K, frequency of the sample oscillations ω and magnetic moment of the measured sample m:

$$e = \mu_0 K \omega m g \cos(\omega t)$$

The geometry of the applied pick-up coils and dimensions of the investigated sample are taken into account by a geometrical factor g [9], which depends on the sample position measured between pick-up coils. Designed pick-up coils should be characterized by a large factor g which should be independent of the position of the moving sample. In R-VSM, the Smith geometry was applied [10] for pick-up coils because of the largest value of the geometrical factor and the flattest dependence of $g(z/a_0)$, in the wide range of sample positions [7] (Fig. 2). From the analysis of g as a function of pick-up coils size (under the assumption that the sample has a form of a dipole), we can see that the largest g is for $z_0/a_0 = 0.5$, where $2z_0$ is the distance between pick-up coils, and a_0 is the radius of the coils applied. For $z_0/a_0 = 0.866$ and $z_0/a_0 = 0.9244$, relative changes of g do not exceed 1%, hence these values are recognized as optimal. The calibration of magnetometer was carried out by examining the geometrical factor g for different shapes of flat samples made of high-purity nickel foil. The main purpose of using R-VSM was to make measurements of the hysteresis loop, saturation magnetization, coercive force and anisotropy field.
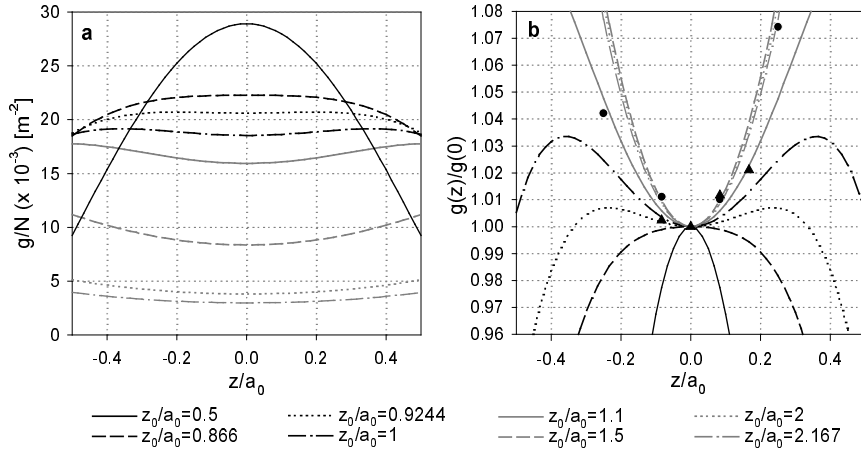
Fig. 2. Geometrical factor for one turn of coils (for dipole sample) (a)
and relative change of geometrical factor for dipole (b): ● – experimental data for Ni foil
with diameter of 0.2 mm and thickness of 20 μm for z_0/a_0 = 2.167 and ▲ – for z_0/a_0 = 244)
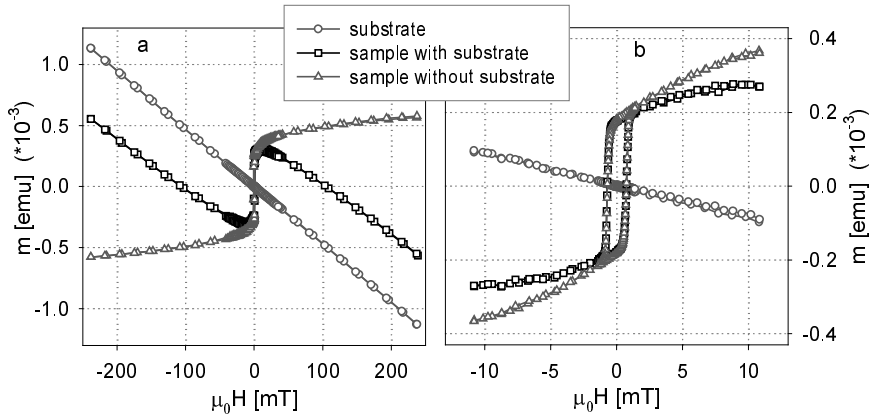
Fig. 3. High-field (a) and low-field (b) measurements
of the MgO (001)/Fe (4 ML)/Cr (50 Å) sample oriented epitaxially

In the case of very thin magnetic films, a signal from the substrate is comparable to the signal from the thin layer as shown in Fig. 3a. Test measurements were performed on monolayers of Fe, with variable thickness: 4 ML, 3 ML and 2 ML (1 ML of Fe = 1.45 Å), deposited by the molecular beam epitaxy (MBE) technique on the MgO (001) substrate and protected against oxidation by a 50 Å thick Cr layer. The volume of the substrate was by seven orders of magnitude higher than that of iron layer (the volume of MgO substrate – 10^{-7} m^3 and volume of 5.8 Å Fe layer – $5.8 \cdot 10^{-14}$ m^3). The signal from the diamagnetic MgO substrate is negative and varies linearly with magnetic field (Fig. 3a). The total signal from substrate and Fe (4 ML = 5.8Å)/Cr (50 Å) was measured in the electromagnet in high magnetic field (Fig. 3a) and in the Helmholtz

coils in low field (Fig. 3b), then the diamagnetic signal from the substrate was subtracted. Finally, the hysteresis loop in the hard direction was obtained (the easy axis is the [001] direction for Fe). A signal very weak, but sufficient to register the magnetic hysteresis, was obtained from 3 ML and 2 ML of Fe samples (Fig. 4).
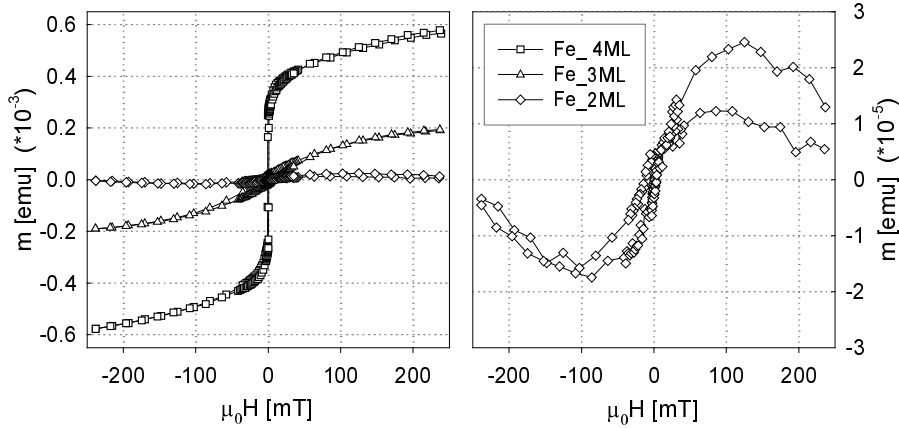
Fig. 4. Hysteresis loops for 2, 3 and 4 ML of Fe after subtracting the signal from the substrate

Based on these measurements, the sensitivity of R-VSM was estimated as 10^{-5} emu, but the magnetic moment resolution was equal to 10^{-6} emu. The resolution of magnetic moment measurement results from digital resolution of the signal measured by the lock-in amplifier.

3. Kerr magnetometer

A high-sensitivity magnetooptical Kerr magnetometer based on the differential amplifier, in contrast to lock-in detection technique, is especially recommended for rapid measurements up to 1.5 kHz. The arrangement for measurements of magnetooptical hysteresis loops is shown in Fig. 5. The coherent light from the He-Ne laser (Z), with 5 mW power and wavelength $\lambda = 633$ nm, is polarized by the Glan–Thompson prism polarizer (P) and is then reflected by the surface of the sample (S) placed in the centre of the Helmholtz coils (H) or an electromagnet. Next, it passes through the Wollaston prism (W) which splits the beam into two beams polarized linearly in mutually orthogonal planes. These beams are focused by the lens (L) on the photodiodes of differential amplifier (A) (for electronics details see [8]). The amplifier delivers both the common (U_C) and the differential (U_D) signals, proportional to the sum and difference of the light intensities of the beams, respectively. These signals are measured by a high-resolution (16 bit) and rapid (200 kHz) AD converter in PCI 6035 computer card. The computer controls the voltage of a programmable bipolar current source (KEPCO BOP 36-12M) which is used to drive the current through the Helmholtz coils (or the electromagnet) to provide a sweeping

holtz coils (or the electromagnet) to provide a sweeping magnetic field. The magnetic field is accurately calibrated before measurements of the hysteresis loop using a teslameter (Htm-11n).
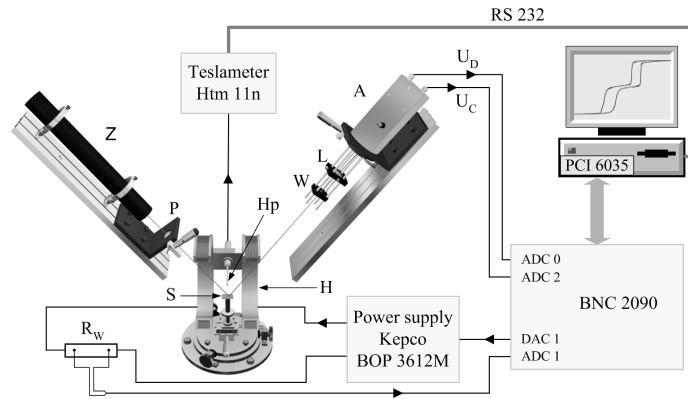
Fig. 5. Schematic layout of MOKE system arrangement: Z – laser, P – polariser,
Hp – Hall probe, W – Wollaston prism, L – lens, A – differential amplifier,
H – Helmholtz coils, E – capacity sensor of the sample position

The MOKE system is programmed using the LabView programming environment. The differential-to-common signal ratio measured as a function of the magnetic field gives hysteresis loop at the point of sample illuminated by the laser beam. For determination of the absolute value of the Kerr rotation angle, a calibration curve of
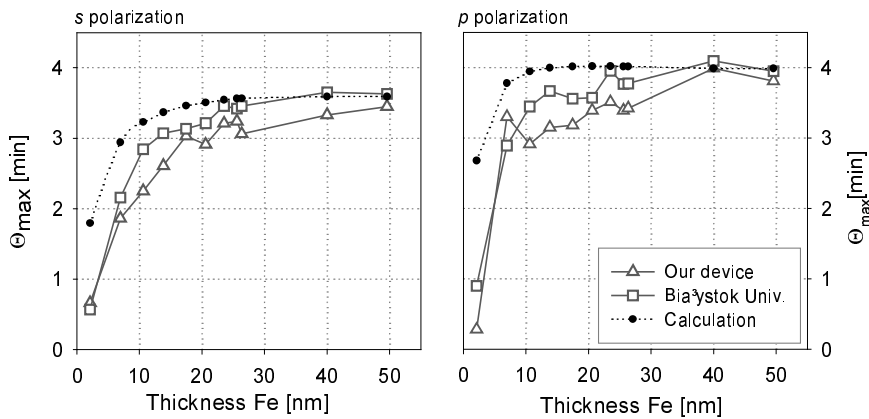
Fig. 6. Kerr rotation angle of Fe-sputtered films measured
in saturation field (0.5 T) vs. thickness of Fe

differential-to-common signal ratio as a function of the rotation angle of the polariza-tion plane $U_D/U_C = f(\Theta_K)$ was recorded. The calibration was done by rotation of

a holder in which the Wollaston prism, the lens and the amplifier with photodiodes are mounted together. Additionally, the calibration of the Kerr rotation angle was performed on standard sputtered Fe films with the thickness from 2 nm to 50 nm, using a Kerr spectrometer (in the Institute of Physics, University of Białystok) based
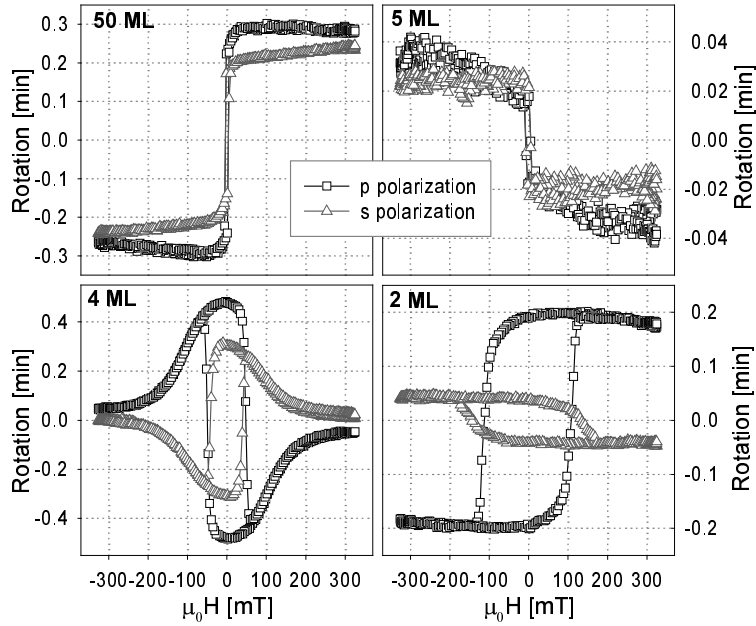
Fig. 7. Kerr rotation hysteresis loops
of 50, 4, 3, 2 ML of Fe for *s* and *p* polarization
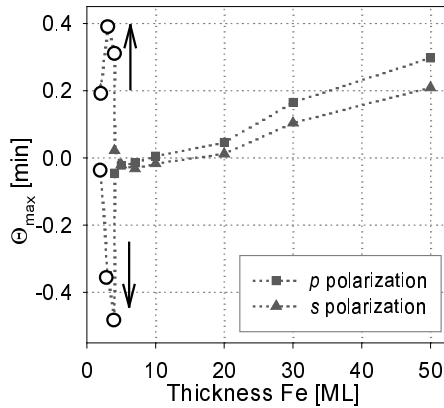
Fig. **8**. Kerr rotation angle of Fe-wedge sample prepared by MBE
vs. thickness for *p* and *s* polarization. The arrows indicate
the transition from in-plane to perpendicular anisotropy

on the polarization modulation technique. Figure 6 shows the experimental and calculated data [5]. We can see that above the thickness of 25 nm, the experimental and calculated data agree very well but below that value the difference between them increases with decreasing thickness of Fe due to the presence of a nonstoichiometric iron-oxide layer about 2 nm thick [8, 11]. The sensitivity of the magnetometer designed was determined on the basis of measurement of ultra-thin Fe wedge film, prepared by MBE technique on the 170 Å thick buffer layer of Au (001) grown on MgO single crystal substrate. The thickness of Fe ranged between 1 ML and 50 ML. The sample was capped with a 30 Å thick Au layer to prevent oxidation. Examples of Kerr rotation hysteresis loops for p and s polarization for 50, 5, 4, 2 ML are shown in Fig. 7. The longitudinal Kerr effect measurement proved the presence of the in-plane magnetic anisotropy for Fe thickness between 50 and 5 ML, showing a decrease of the Kerr rotation with decreasing Fe thickness (Fig. 8). Below the critical thickness (5 ML), a drastic increase of the Kerr rotation was observed due to the change of the easy magnetization axis in the direction perpendicular to the layer. This change was accompanied by the appearance of the polar contribution to the measured signal [12]. The measurements on Fe wedge sample prove that 2 ML Fe is still ferromagnetic at a room temperature (Fig. 7). On the basis of these measurements the angle resolution of the Kerr rotation was estimated as 0.001 min.

4. Test measurements using spintronic elements

The measurements of the hysteresis loops were performed on selected spin valve structures and on an array of magnetic dots [8]. The spin valve Ta (52 Å)/Co (44 Å) /Cu (22 Å)/Co (44 Å)/FeMn (100 Å)/Ta (52 Å) structure sputtered on Si(100) is demonstrated here as an example (Fig. 9). In contrast to the magnetization of R-VSM measurement, the signal of the magnetooptical hysteresis loop is higher for pinned layer (lying at the top of multilayer system) due to light absorption effect.
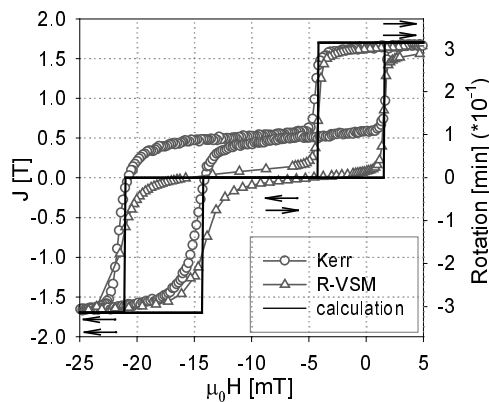
Fig. 9. Comparison of the spin valve hysteresis loops:
magnetization (R-VSM), Kerr rotation angle and calculated values

Nevertheless, the switching fields determined from magnetization and Kerr effect measurements are almost the same. The calculations of magnetization hysteresis loop agree very well with the measurements performed by means of R-VSM. The fitting parameters are the following: interlayer exchange energy $J_1 = 7.9 \cdot 10^{-6}$ J/m^2, exchange biased energy $E_{EB} = 113 \cdot 10^{-6}$ J/m^2 and uniaxial anisotropy of a free and the pinned layers are $K_{u1} = 2.05 \cdot 10^3$ J/m^3 and $K_{u2} = 2.4 \cdot 10^3$ J/m^3, respectively.

5. Conclusions

The magnetometers designed are highly sensitive and able to measure very thin films down to 2 ML of Fe. Due to simple operation methods, both instruments are recommended for a fast characterization of fundamental magnetic parameters of monoatomic layers, multilayers and spintronics elements. They are simple from the electronic point of view as well as from the mechanical one, the cost of constructing the two magnetometers being very low in relation to commercial devices.

References

[1] PARKIN S.S.P., ROCHE K.P., SAMANT M.G., RICE P.M., BEYERS R.B., SCHEUERLEIN R.E., O'SULLIVAN E.J., BROWN S.L., BUCCHIGANO J., ABRAHAM D.W., LU YU, ROOKS M., TROUILLOUD P.L., WANER R.A., GALLAGHER W.J., J. Appl. Phys., 85 (1999), 5828.

[2] TUMAŃSKI S., *Thin Film Magnetoresistive Sensors*, IOP Bristol and Philadelphia, 2001.

[3] SONG D., NOWAK J., LARSON R., KOLBO P., CHELLEW R., IEEE Trans. Magn., 36 (2000), 2545.

[4] WRONA J., CZAPKIEWICZ M., STOBIECKI T., J. Magn. Magn. Mat., 196–197 (1999), 935.

[5] WRONA J., STOBIECKI T., RAK R., CZAPKIEWICZ M., STOBIECKI F., UBA L., KORECKI J., ŚLĘZAK T., WILGOCKA-ŚLĘZAK J., ROTTS M., phys. stat. sol. (a), in press.

[6] FONER S., Rev. Sci. Instr., 30 (1959), 548.

[7] PACYNA A.W., J. Phys. E: Sci. Instrum., 17 (1984), 141.

[8] WRONA J., *Magnetometry of thin film structures*, PhD.Dissertation, University of Mining and Metallurgy, Kraków, 2002.

[9] ZIĘBA A., FONER S., Rev. Sci. Instrum., 53 (1982), 1344.

[10] SMITH D. O., Rev. Sci. Instr., 27 (1956), 261.

[11] POSTAVA K., BOBO J.F., ORTEGA M.D., RAQUET B., JAFFRES H., SNOECK E., GOIRAN M., FERT A.R., REDOULES J.P., PIŠTORA J., OUSSET J.C., J. Magn. Magn. Mat., 163 (1996), 8.

[12] LIU C., BADER S.D., J. Magn. Magn. Mat., 93 (1991), 307.

The effect of underlayers on grain orientation and magnetic properties of barium-ferrite thin film

DONG HYOUN KIM[1], IN TAK NAM[1*], YANG KI HONG[2]

[1]Kangwon National University, 192-1 Hyoja 2-dong, Chunchon, 200-701, Korea

[2]University of Idaho, Moscow, ID83844-3024, USA

The effect of employing various sputtered underlayers has been studied in order to optimize the characteristics of barium ferrite (BaM) thin films for magnetic recording media. BaM thin films and underlayers (Fe, Cr, Al_2O_3, Fe_2O_3, $ZnFe_2O_4$, TiO_2) were prepared by rf/dc magnetron sputtering on (100) oriented bare Si substrate, and were crystallized by post-annealing. All the BaM films, except the BaM/Fe/Si film, attained nearly the same perpendicular and in-plane coercivities. Perpendicular anisotropy was observed in BaM/Fe/Si film. The BaM/TiO_2/Si exhibits the highest coercivity. However, regardless of the underlayer, BaM grains are oriented at random. By adopting $ZnFe_2O_4$ as an underlayer, the interdiffusion of Si from substrate was prohibited to some degree. The microstructure of BaM in BaM/TiO_2/Si was strongly dependent on both the microstructure of TiO_2 underlayer and the total sputtering gas pressure. The control of an underlayer microstructure is one of the important factors to control grain size and shape of the BaM layer.

Key words: *BaM film; underlayer; anisotropy; coercivity; microstructure*

1. Introduction

Hexagonal barium ferrite (BaM) thin film is considered to be an attractive magnetic recording medium because of its large coercivity, corrosion resistance, high-anisotropy field, mechanical hardness, and chemical stability. The mechanical hardness and stability of BaM film may make it possible to achieve a low flying height without an overcoat [1]. The preparation of BaM films with a uniaxial magnetic anisotropy in the out-of-plane direction is problematic when BaM is deposited directly onto amorphous substrates such as Si wafers with a thermally oxidized surface layer (SiO_2 /Si) or a fused quartz slide [2]. It has been shown that the microstructure and magnetic properties of BaM thin film can be improved using an underlayer [3]. Hyl-

---

ton, Parker, and Howard [4] have reported that interdiffusion between the BaM film and the substrate strongly affects the magnetic properties. They suggests the need for applying a buffer layer between the film and substrate. In-plane magnetocrystalline anisotropy, high coercivity, and remanence have been reported in BaM films deposited on sapphire [5] and other buffer layers [6]. The anisotropy was raised because the *c*-axis of BaM crystallites was dominantly oriented in the film plane. This is attributed to the uniaxial magnetic anisotropy with easy axis in the plane of the film. General criteria for selection of substrate and appropriate underlayer materials are low cost, mechanical hardness coupled with the ability to withstand high-temperature annealing, chemical stability, and limited interdiffusion while providing good adhesion with the BaM film [4]. Wee et al. [6] employed various underlayers such as Al_2O_3, Cr_2O_3, SiO_2, CuO, and TiO_2 to optimize the characteristics of BaM thin films for magnetic recording applications. Both high coercivity (400 kA/m) and squareness (about 0.92) were achieved using Al_2O_3 as an underlayer, while the TiO_2 underlayer exhibited the lowest coercivity (28 kA/m) of all underlayers studied. In contrast to earlier work [6], we report in this article the dependence of microtexture, microstructure, and magnetic properties of barium-ferrite thin films on the kind of the underlayer.

2. Experimental

BaM thin films were prepared using an rf/dc magnetron-sputtering system onto the (100) oriented bare silicon substrates. All films were deposited in-situ. The targets for the deposition of the BaM and $ZnFe_2O_4$ underlayers were sintered ferrite disks with

Table 1. Sputter deposition conditions for underlayer and barium-ferrite thin films

Thin film		Method	Sputtering gas	Substrate temp.	Total gas pressure (mm Hg)	Thickness (nm)
Underlayer	Fe	DC	Ar	room temp.	10,000	100
	Cr	DC	Ar	room temp.	10,000	100
	Fe_2O_3	RF	Ar + 10% O_2	room temp.	10,000	50
	Al_2O_3	RF	Ar + 10% O_2	room temp.	10,000	100
	$ZnFe_2O_4$	RF	Ar + 10% O_2	room temp.	5,000	50
	TiO_2	DC	Ar + 30% O_2	room temp.	5,000 10,000	70
Magnetic layer	BaM	RF	Ar + 10% O_2	room temp.	5,000 10,000	60

the stoichiometric composition of $BaFe_{12}O_{19}$ and $ZnFe_2O_4$. The Fe_2O_3 and TiO_2 underlayers were reactively sputtered with oxygen gas. All other underlayers were deposited using Cr, Fe and Al_2O_3 targets. After having evacuated the sputter chamber to a pressure below 2×10^{-6} mm Hg (TiO_2 – below 3×10^{-7} mm Hg), argon and oxygen gases were introduced into the chamber. The total gas pressure was maintained at either 5,000 mm Hg or 10,000 mm Hg. The deposition conditions for the underlayers and the BaM layer are given in Table 1. All as-deposited films were annealed in the range of 700–850 °C for 10 min using a rapid thermal annealing furnace oven to achieve a magnetic crystallization BaM phase. The crystallographic structure and microstructure of the annealed films were characterized by means of X-ray diffraction (XRD) and field-emission scanning electron microscope (FESEM), respectively. The magnetic properties of the films were measured by a vibrating sample magnetometer.

3. Results and discussion

Figure 1 shows XRD patterns of BaM films with various underlayers. The basal planes, which are (006) and (008) peaks, as well as other planes such as (107) and (114) peaks were observed. The relative intensities of (107) and (114) peaks, which correspond to the inclined *c*-axis orientation, are higher than those of (006) and (008) peaks. These results indicate that the grains of all the BaM films are favourably crystallized and developed the random orientation of crystal structure. On the other hand, all major peaks for the BaM crystalline phase disappeared for the $BaM/TiO_2/Si$ film except for the (116) and (302) peaks. In the case of $BaM/ZnFe_2O_4/Si$ film, the intensity of Si peak, originating from Si substrate, was extremely weak compared to those of BaM films with other underlayers. This result supports the conclusion that the $ZnFe_2O_4$ underlayer prevented, to some degree, the interdiffusion of Si from the substrate to the BaM film.

Table 2. Coercivity values of barium-ferrite
thin films with various underlayers

Underlayer	Coercivity (kA/m)	
	Longitudinal	Perpendicular
Fe	16	88
Cr	350	366
Fe_2O_3	263	247
Al_2O_3	287	287
$ZnFe_2O_4$	183	151
TiO_2	374	350

The coercivity values of BaM films with various underlayers are summarized in Table 2. All films revealed nearly the same coercivity in both in-plane and out-of

-plane directions except for BaM/Fe/Si film, indicating that all the films do not possess crystalline magnetic anisotropy. This is consistent with the results of XRD. With regard to the effect of underlayer thickness on coercivity, the Fe_2O_3 underlayer, thinner than all other underlayers, exhibits almost the same coercivity as those of the films with other underlayers. This suggested that about 26 kA/m of coercivity is achievable with the 50 nm thick Fe_2O_3 underlayer compared to the other underlayers 100 nm thick. It was suggested that Fe_2O_3 underlayer was effective in reducing thickness for obtaining desirable coercivity of BaM film. In contrast to Wee's results [6], BaM/TiO_2/Si films exhibit the highest coercivity of all films with underlayers.
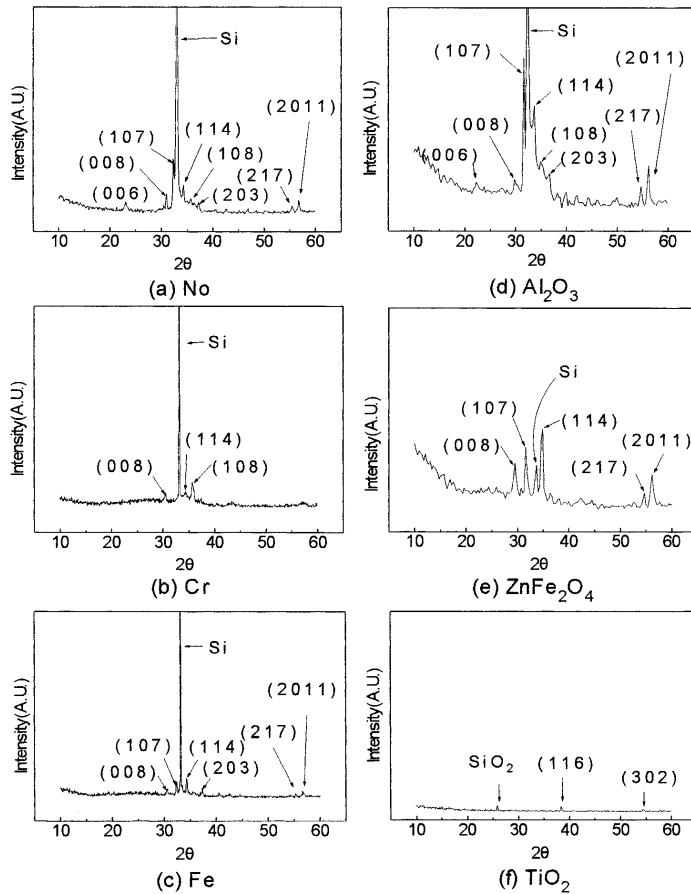
Fig. 1. X-ray diffraction patterns of barium-ferrite thin films with various underlayers

The BaM/Fe/Si film shows the hard magnetic property (88 A/m) for the out-of-plane direction compared to the soft magnetic behaviour (16 A/m) for the in-plane direction (Fig. 2). The saturation magnetization (225 emu/cm^3) for the in-plane direction is about three times larger than that for the out-of-plane direction. The high

perpendicular coercivity is not attributed to the magnetic crystalline anisotropy of the BaM layer because BaM grains are randomly oriented, which is evidently shown by X-ray diffraction pattern. Morisako et al. [3] have reported that during a post-annealing process, both Ba and Fe diffused into the substrate, and the Fe atoms diffused deeper into the substrate than Ba atoms, consequently changing the Ba/Fe ratio in the BaM film. This change may cause a large increase in both the in-plane saturation magnetization and the perpendicular coercivity of the BaM film.
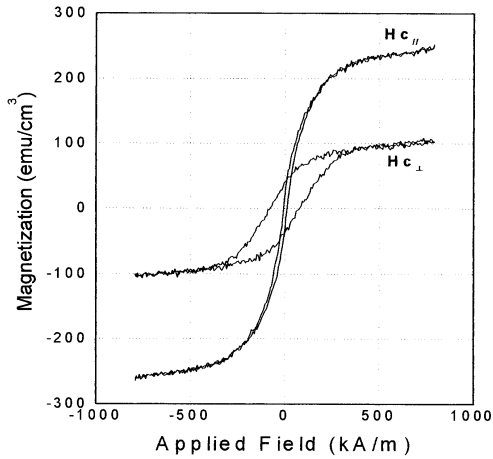
Fig. 2. Magnetization hysteresis of barium-ferrite thin films with Fe underlayer, post-annealed at 850 °C for 10 min
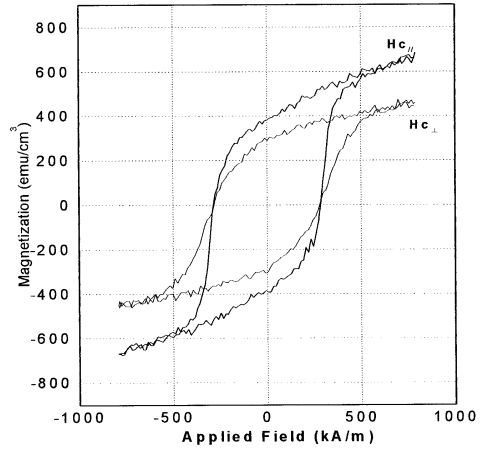
Fig. 3. Hysteresis loops of the BaM/Al$_2$O$_3$/Si thin films post-annealed for 10 min at 850 °C
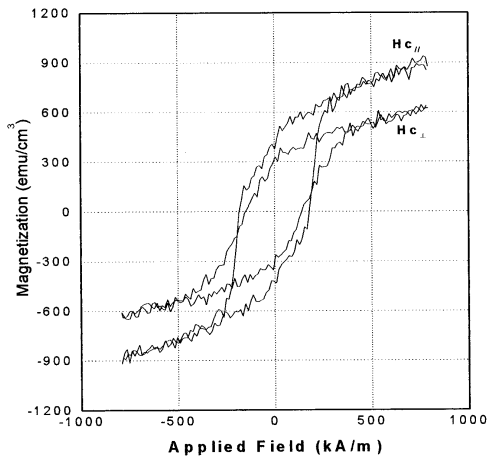
Fig. 4. Hysteresis loops of the BaM/ZnFe$_2$O$_4$/Si thin films post-annealed for 10 min at 850 °C
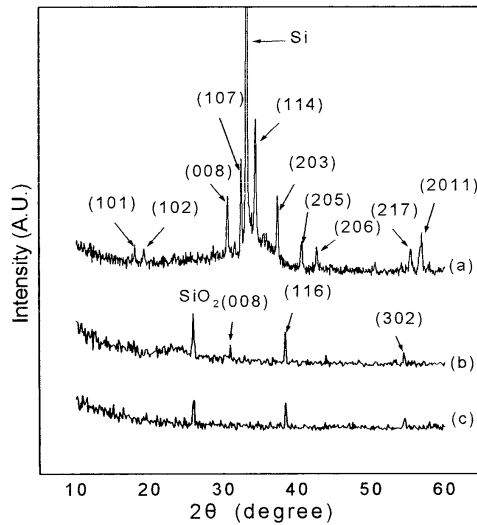
Fig. 5. XRD patterns for BaM thin films without or with TiO$_2$ underlayer: a) no underlayer, 850 °C, b) TiO$_2$ underlayer, 800 °C, c) TiO$_2$ underlayer, 750 °C

The hysteresis loops of the BaM/Al$_2$O$_3$/Si and BaM/ZnFe$_2$O$_4$/Si thin films are shown in Figs. 3 and 4. Longitudinal recording media have been successfully achieved by deposition on sapphire substrate [5]. However, the high cost of sapphire limits the commercial application of these films. Therefore, we investigated the effect of polycrystalline Al$_2$O$_3$ underlayer on the BaM thin film. As shown in Fig. 4, BaM/Al$_2$O$_3$/Si thin films reveal that the coercivities in perpendicular and in-plane direction are the same and equal to 287 A/m. It was reported that when BaM film was deposited onto the sputtered ZnO underlayer, ZnFe$_2$O$_4$ was formed between BaM and ZnO layers. ZnFe$_2$O$_4$ is the product of the reaction of BaM with ZnO, which reduces the lattice mismatch between these layers [7]. It is expected that ZnFe$_2$O$_4$ underlayer can improve perpendicular c-axis orientation of BaM film deposited onto it. However, the hysteresis loops shown in Fig. 5 have similar shapes and reduced coercivities in both in-plane and out-of-plane directions.

Figure 5 shows X-ray diffraction diagrams of BaM films with or without TiO$_2$ underlayer. BaM/TiO$_2$/Si thin film deposited on the Si substrate at a room temperature was amorphous. In the BaM/Si thin film of Fig. 5a, the basal planes, which are (008), as well as other planes such as (107) and (114) reflections were observed after annealing. The relative intensities of (107) and (114) peaks, which correspond to the inclined c-axis orientation out of the film plane, were higher than those of the (008) peak. These results indicate that the BaM films were favourably crystallized and developed the random orientation of crystal structure. In addition, the absence of those peaks in Fig. 5b, c associated with the underlayers confirms the amorphous state of the underlayer film. For the BaM/TiO$_2$/Si film, the diffraction of merely (116) and (302) peaks was observed when BaM/TiO$_2$/Si thin film was crystallized at 750 °C by post-annealing. On the other hand, BaM/Si films with no underlayer were well crystallized at 850 °C. There was no significant increase in the peak intensity as the annealing temperature increased to 800 °C. This result suggests that TiO$_2$ underlayer is effective in lowering the annealing temperature of as-deposited BaM film.

Figure 6 shows micrographs of post-annealed BaM/Si, TiO$_2$/Si and BaM/TiO$_2$/Si films. The grain shapes of BaM/Si film are indicative of epitaxial growth of the film. The grains of a small size (about 20 nm) with elongated shape are present, in which BaM grows with the c-axis parallel to the film plane. However, as shown in Fig. 6c, the platelet and elongated grains were observed in BaM/TiO$_2$/Si film. The growth of BaM films was significantly influenced by a TiO$_2$ underlayer. As shown in Fig. 7, BaM/TiO$_2$/Si thin film was crystallized at 750 °C by post-annealing. For most of BaM/TiO$_2$/Si thin films, the coercivity values of the films prepared at 750 °C were higher than those of the films prepared at 800 °C. The microstructure of BaM in BaM/TiO$_2$/Si films was strongly dependent on the total Ar/O$_2$ gas pressure. Although acicular grains are usually grown in BaM film without underlayer [8], pop-corn type grains were observed at 10,000 mm Hg, and elongated grains at 5,000 mm Hg. It was evident that the BaM reproduces the microstructure of the TiO$_2$ underlayer (Fig. 6).

The selection of underlayer should be considered to optimize magnetic properties and microstructure of BaM films.

a)

b)

c)
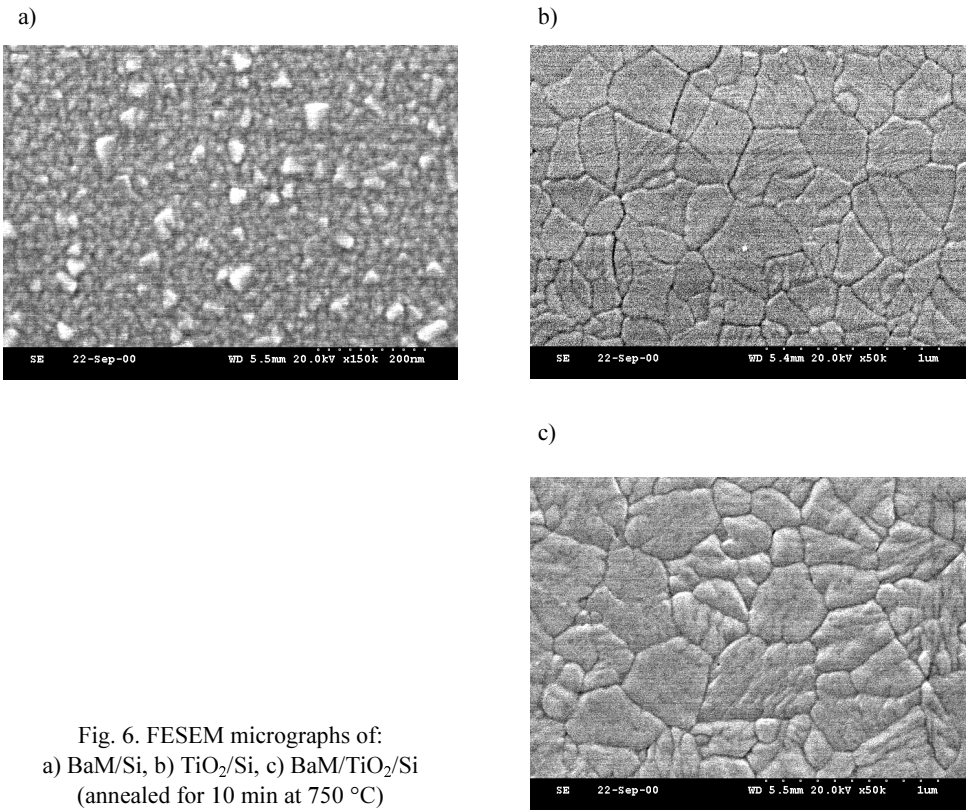
Fig. 6. FESEM micrographs of:
a) BaM/Si, b) TiO$_2$/Si, c) BaM/TiO$_2$/Si
(annealed for 10 min at 750 °C)

a)

b)
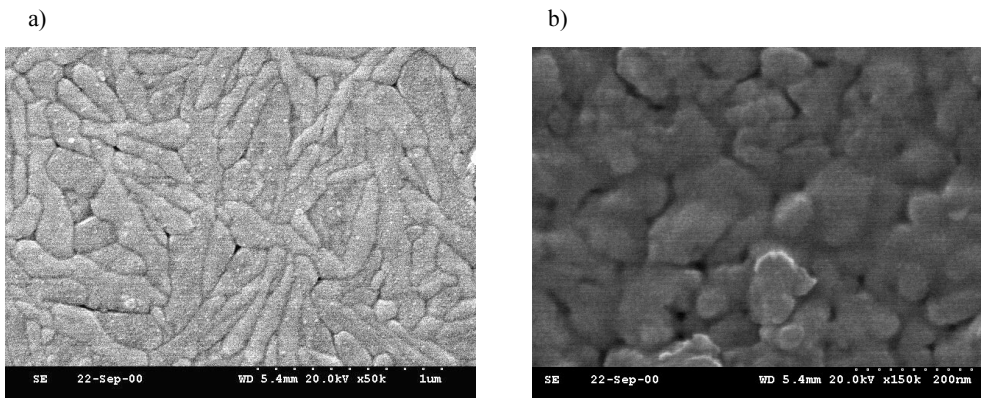
Fig. 7. FESEM micrographs of BaM/TiO$_2$/Si thin films deposited at: a) 5,000 mm Hg, b) 10,000 mm Hg

4. Conclusions

All the films with various underlayers, except for BaM/Fe/Si film, showed nearly the same out-of-plane and in-plane coercivities, indicating random orientation of BaM grains. BaM/Fe/Si thin film exhibited a strong out-of-plane magnetic anisotropy. Comparing with underlayer thickness, the coercivity of BaM/Fe$_2$O$_3$/Si film was almost the same as those of BaM films with other underlayers. By adopting ZnFe$_2$O$_4$ as an underlayer, the interdiffusion of Si from substrate was prohibited to some degree. The microstructure of BaM/TiO$_2$/Si film was strongly dependent on both the microstructure of the TiO$_2$ underlayer and the total gas pressure. The control of the underlayer microstructure is one of the important factors to control the grain size and shape of the BaM layer.

References

[1] WONG B.Y., SUI X., LAUGHLIN D.E., KRYDER M.H., J. Appl. Phys., 75 (1994), 5966.
[2] KAKIZAKI K., HIRATSUKA N., J. Magn. Soc. Jpn., 21 (1997), Suppl. 1, 65.
[3] MORISAKO A., LIU X., MATSUMOTO M., NAOE M., J. Appl. Phys., 81 (1997), 4374.
[4] HYLTON T.L., PARKER M.A., COFFEY K.R., UMPHRESS R., HOWARD J.K., J. Appl. Phys., 75 (1994), 5960.
[5] HYLTON T.L., PARKER M.A., HOWARD J.K., Appl. Phys. Lett., 61 (1992), 867.
[6] WEE A.T., WANG J.P., HUAN A.C.H., TAN L.P., GOPALAKRISHNAM R., TAN K.L., IEEE Trans. Magn., 33 (1997), 2986.
[7] LI J., SINCLAIR R., ROSENBLUM S.S., HAYASHI H., J. Mater. Res., 10 (1996), 2343.
[8] ISHIKAWA A., TANAHASHI K., FUDAMOTO M., J. Appl. Phys., 79 (1996), 7080.

Magnetism of nanocrystalline and bulk $Fe_xNi_{23-x}B_6$ ($x = 0, 1, 22$ and 23) alloys − experiment and theory

B. IDZIKOWSKI[*], A. SZAJEK

Institute of Molecular Physics, Polish Academy of Sciences,
M. Smoluchowskiego 17, 60-179 Poznań, Poland

Formation of the nanostructure composed of a metastable magnetically ordered fcc-$Fe_xNi_{23-x}B_6$ phase with large lattice constant ($a = 1.051$–1.082 nm) from amorphous $Fe_{81-y-z}Ni_yZr_7B_{12}Au_y$ ($y = 10$–$40, 64$; $z = 0, 1$) precursors due to the thermal treatment has been studied. Annealing of the $y \geq 20$, $z = 0$ samples at temperatures of 420–580 °C leads to an increase of $Fe_xNi_{23-x}B_6$ fraction embedded in amorphous matrix with grain sizes from a few to tens of nanometres. The structure transformations have been investigated by the DSC, XRD and TEM techniques. Magnetic behaviour of $Fe_xNi_{23-x}B_6$ ($x = 0, 1, 22$ and 23) phases has been studied theoretically using the spin polarized tight binding linear muffin-tin orbital (TB-LMTO) method. Anomalously high magnetic moments of Fe atoms have been found in some non-equivalent positions in the crystal structure.

Key words: *amorphous alloys; nanocrystallization; density of states; local magnetic moments*

1. Introduction

Investigations of crystallization processes of amorphous precursors have attracted a lot of attention in recent years because some of them form nanocrystalline structure. Such a reduction of the grain sizes influences drastically the physical behaviour of materials. The search continues for new nanocrystalline alloys with improved magnetic and mechanical properties, convenient for technical applications. Up to now these alloys, produced by a partial crystallization of amorphous precursors, have exhibited a two- or more-phase structure with body-centred cubic (*bcc*) nanocrystalline grains dispersed in a residual amorphous matrix. All known soft magnetic nanocrystalline alloys consist of nanosized *bcc*-Fe(Si) [1], *bcc*-Fe [2] or *bcc*-(FeCo) [3] grains with 3–15 nm in diameter. During the devitrification processes, the amorphous part of alloys becomes inhomogeneous, showing significant gradients of compositions.

_____

[*]Corresponding author, e-mail: Bogdan.Idzikowski@ifmpan.poznan.pl.

The crystallization of Ni-containing amorphous alloys was studied earlier (e.g., [4, 5]) but those alloys were unsuitable for the formation of nanocrystalline alloys. However, the nanocrystalline grains were found in rapidly heated amorphous $Fe_{15}Ni_{60}Si_{10}B_{15}$ and $Fe_{20}Ni_{55}Si_{10}B_{15}$ systems [5]. The only Ni-containing amorphous system, $Fe_{40}Ni_{38}Mo_4B_{18}$, in which the nanostructured phase was clearly formed, was studied by the XRD technique [6]. In this case, the presence of Mo atoms in the alloy plays crucial role in the process of nanostructure formation because of the grains growth blocking. Extremely fine nanocrystalline structure is expected if small additions of e.g., Cu or Au are present in the amorphous precursor. Recently, Nakamura et al. [7] reported on the crystallization of amorphous $Fe_{70}Nb_{10}B_{20}$ alloy – the final product is *fcc*-$Fe_{23}B_6$ phase with a large lattice parameter. The authors observed in this system the nanometer-sized metastable $Fe_{23}B_6$ precipitates in the amorphous matrix before creation of the equilibrium *bcc*-Fe and boride phases in final crystallization state [7].

We prepared nickel-rich amorphous alloys $Fe_{81-y-z}Ni_yZr_7B_{12}Au_y$ (y = 10–40, 64; z = 0, 1) in which the nanostructure can be formed, as usually, by a controlled annealing but the significant presence of Ni in this alloys results in the formation of a metastable *fcc*-phase containing both transition elements (Ni and/or Fe) and boron. Because obtaining a pure single phase $TM_{23}B_6$ (TM = Fe, Ni) compounds by standard methods is difficult, we have also performed theoretical study of their magnetic behaviour.

2. Experimental

Fully amorphous ribbons with the nominal compositions $Fe_{81-y-z}Ni_yZr_7B_{12}Au_y$ (y = 10–40, 64; z = 0, 1) were prepared by the single roller (40 cm in diameter) technique in Ar protective atmosphere. High-purity elements (minimum 3N) were used to make starting pre-alloys. Each ingot was turned over several times and melted in the induction furnace water cooled boat to assure homogeneity. Long ribbons obtained were 2–3 mm wide and 0.35–0.45 µm thick. The structure of the samples was characterized by X-ray diffraction (XRD) analysis in a Seifert diffractometer using Cu-Kα radiation. The crystallization behaviour of as-quenched ribbons was examined with differential scanning calorimetry using DSC 404 made by Netzsch. For the transmission electron microscopy (TEM) studies, the samples were prepared by argon ion milling using 10 keV ions. TEM investigations were done using a Philips CM20 microscope (TWIN configuration, accelerating voltage: 200 kV), equipped with a Noran Voyager EDS system with Ge (Li) detector.

3. Results of measurements

Structural changes of amorphous precursors induced by thermal treatment were characterized by the differential scanning calorimetry (DSC) and X-ray diffraction (XRD) measurements. DSC linear-heating curves of all Ni-rich alloys investigated

show two crystallization stages. Such behaviour is typical of amorphous alloys serving as the precursors for the formation of the nanocrystalline alloys [8]. The crystallization temperature of the first stage is in the range of 460–520 °C. DSC measurements (not shown here) were carried out with 20 K/min heating rate. For samples $y \leq 20$ the nanocrystalline phase, which precipitates around the first exothermic peak, is *bcc*-Fe. If $y > 20$, the nanocrystallization product is *fcc*-(Fe,Ni)$_{23}$B$_6$. A similar crystallization behaviour was observed by Nakamura et al. in Fe$_{70}$Nb$_{10}$B$_{20}$ alloys where the average lattice constant $a = 1.067$ nm for the Fe$_{23}$B$_6$ fraction was assumed [7]. This lattice parameter (as well as other properties [9]) could differ from the values of bulk alloy because of two reasons: (i) interface of small grains can influence local crystal structure, (ii) relative large atoms of such elements as Nb or Zr could be placed inside the grain.
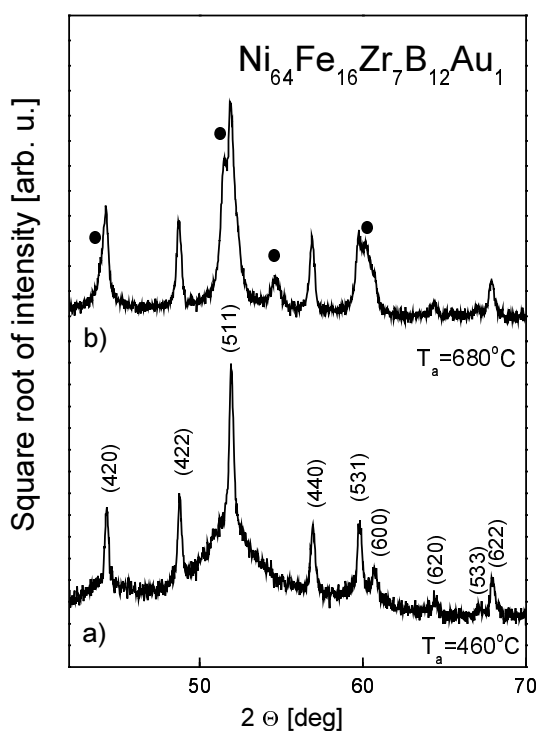
Fig. 1. X-ray diffraction (XRD) patterns for Ni$_{64}$Fe$_{16}$Zr$_7$B$_{12}$Au$_1$
ribbon after annealing at 460 °C and 680 °C for one hour

The as-quenched samples are fully amorphous, as found by XRD, with a broad diffuse peak around 43 degrees on 2Θ axis. Figures 1a and 1b show the structure of Ni$_{64}$Fe$_{16}$Zr$_7$B$_{12}$Au$_1$ partially crystallized after one-hour annealing at 460 °C and 680 °C, respectively. As a result of the annealing, grains of magnetically ordered cubic Fe$_x$Ni$_{23-x}$B$_6$ phase appear in the amorphous matrix. All peaks have been identified

and all of them belong to the C_6Cr_{23}-type structure described by the space group $Fm(-3)m$. As shown in Fig. 1b, the increase of annealing temperature is connected with the decrease of the amount of the 23:6 phase, and the appearance of a new $(FeNi)_3B$ phase is marked by large black points.
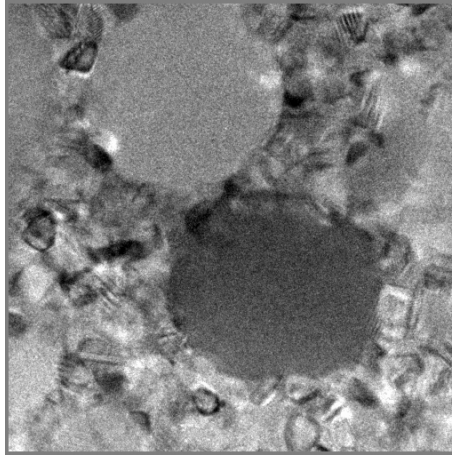
Fig. 2. Transmission electron micrograph of $Ni_{42}Fe_{40}Zr_7B_{12}$
alloy after annealing at 640 °C for one hour

TEM picture of $Ni_{42}Fe_{40}Zr_7B_{12}$ alloy heat treated at 640 °C is shown in Fig. 2. A fraction of very small grains (several nanometers in diameter) is present among relatively big grains. The chemical composition of small and big grains is the same, as has been confirmed by electron microdiffraction investigations (not shown here). The annealed nanocrystalline ribbons became magnetically soft because of exchange interaction between these small grains. A very similar mixture of majority small and minority big grains was found in HITPERM-type soft magnetic alloys.

4. Details of band structure calculations

The spin-polarized tight binding linear muffin-tin orbital (TB-LMTO) method in the atomic sphere approximation (ASA) [10, 11] was used to compute the electronic band structure of $Fe_{23}B_6$ and $Ni_{23}B_6$ compounds. In this approximation, the crystal is divided into space-filling spheres, therefore with slightly overlapping spheres centred on each of the atomic sites. The standard combined corrections for overlapping [10] were employed to compensate ASA errors. In the calculations reported here, the Wigner–Seitz (WS) sphere radii are such that the overlap is below 10%. The total volumes of all spheres S_j ($j = 1, ..., N$) are equal to the volume (V) of the unit cell. The values of lattice constants of $Fe_{23-x}Ni_xB_6$, for $x = 0, 1, 22$ and 23, are extrapolated from the experimental data taken for $x = 0$ [12] and $x = 4.5$ [13] (see Fig. 3). The sys-
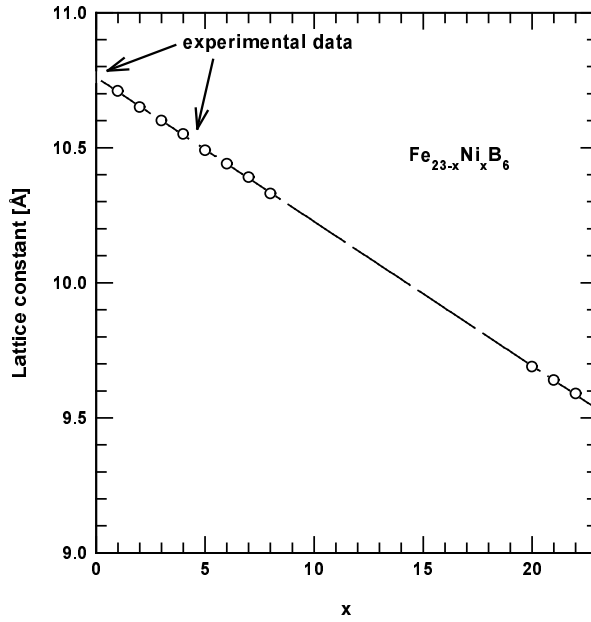
Fig. 3. Lattice constants for Fe$_{23-x}$Ni$_x$B$_6$ as a function of x.
Data for $x = 0$ and 4.5 are taken from the literature

Table 1. Structural parameters of Fe$_{23-x}$Ni$_x$B$_6$ compounds
(a = 1.0761, 1.071, 0.959 and 0.953 nm for x = 0, 1, 22 and 23) and *WS* radii S_j [Å]

Atom (position)	x	y	z	S_j			
				$x = 0$	$x = 1$	$x = 22$	$x = 23$
Fe or Ni (4a)	0	0	0	1.7007	1.6922	1.5177	1.5213
Fe or Ni (8c)	¼	¼	¼	1.5576	1.5498	1.3897 (1/2) 1.4040 (1/2)	1.3942
Fe or Ni (48h)	0	0.1699	0.1699	1.3852	1.3788	1.2286 (1/2) 1.2429 (1/4) 1.2286 (1/4)	1.2205
Fe or Ni (32f)	0.3809	0.3809	0.3809	1.3543	1.3480	1.2152(Ni; 1/8) 1.2152(Fe; 1/8) 1.2009(Ni; 3/8) 1.2009 (Ni; 3/8)	1.1930
B (24e)	0.2765	0	0	1.1908	1.1847	1.0615 (1/2) 1.0758 (1/2)	1.0683

tem has a cubic symmetry (for $x = 0$ and 23: *Fm*(–3)*m* space group, No. 225). Its unit cells accommodate four formula units with $N = 116$ atoms. There are four non-equivalent positions of Fe(Ni) atoms (see Table 1) in the Ni$_{23}$B$_6$ and Fe$_{23}$B$_6$ compounds. The single atom impurities (Ni or Fe for $x = 1$ and 22, respectively) in

$Fe_{23-x}Ni_xB_6$ were located one after another in 4a, 8c, 48h, and 32f positions. The broken symmetry gives additional non-equivalent positions within 8c, 48h, 32f, and 24e sites for $x = 22$. They are presented in Table 1 for $x = 22$ together with their occupancy (in parentheses) within particular sites.

As starting, the following atomic configurations were assumed: core [Ar] + $3d^6 4s^2$ for Fe, core [He] + $2p^2 2s$ for B, and core [Ar] + $3d^8 4s^2$ for Ni. The fully relativistic approach for the core electrons and scalar relativistic approximation for the valence electrons were used. The Min–Jang [14] scheme for calculating the spin-orbit effects was employed. The exchange-correlation potential was chosen in the form proposed by von Barth–Hedin [15]. Self-consistent calculations were performed for 8000 k-points in the Brillouin zone. The tetrahedron method [16] was used for integration over the Brillouin zone. The iterations were repeated until the accuracy of the energy eigenvalues within the error of 0.01 mRyd was achieved.

5. Results of calculations

The TB LMTO ASA method allows differentation of the ions in the cell but the effect of disorder caused by Ni or Fe substitution is neglected. In the case of the C_6Cr_{23}-
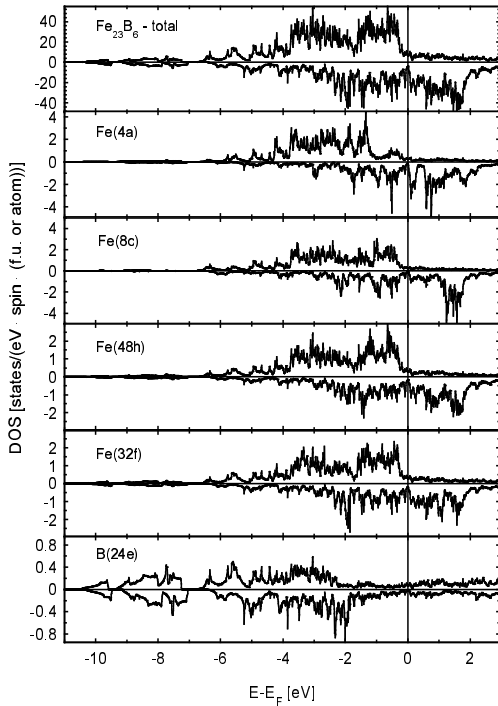
Fig. 4. Total and local density of states
(DOS) plots for $Fe_{23}B_6$ compound
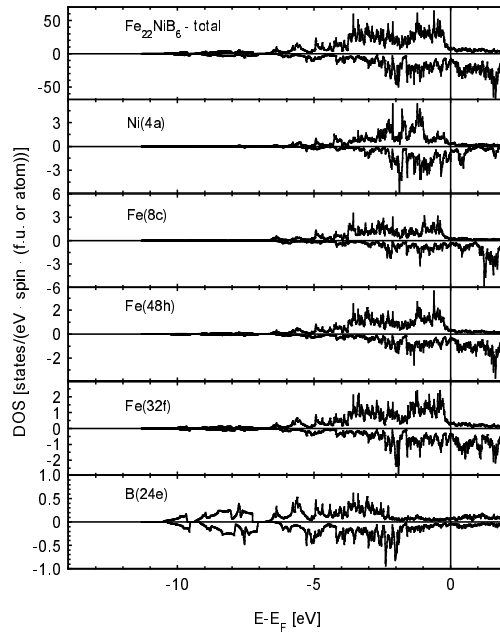
Fig. 5. Total and local density of states
(DOS) plots for $Fe_{22}NiB_6$ compound
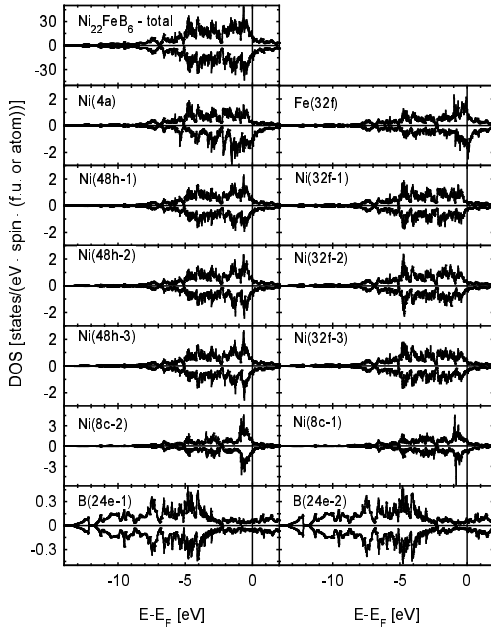
Fig. 6. Total and local density of states
(DOS) plots for Ni$_{22}$FeB$_6$ compound
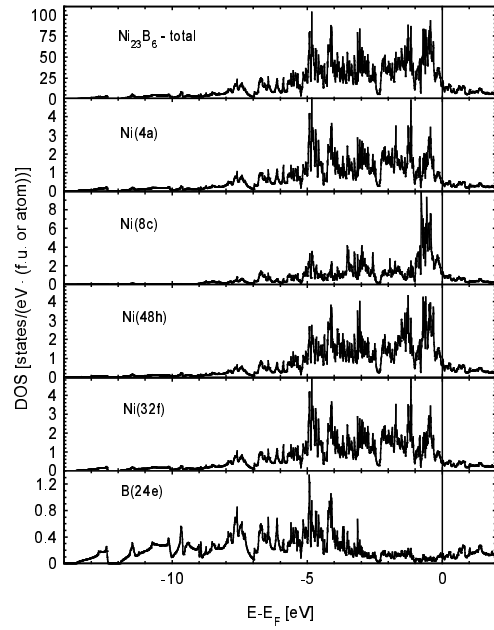
Fig. 7. Total and local density of states
(DOS) plots for Ni$_{23}$B$_6$ compound

type structure the 4a, 8c, 48h, and 32f positions for Fe/Ni atoms have to be considered. Our total energy calculations show that in the case of Fe$_{22}$NiB$_6$ the Ni atoms prefer 4a position and in the case of Ni$_{22}$FeB$_6$ the Fe atoms prefer 32f sites. The results presented below concern the most stable localizations of the impurities, which minimize total energy. The total and local densities of states (DOS) for Fe$_{23-x}$Ni$_x$B$_6$ are presented in Figs. 4–7.

The shape of DOS plots depends on the type of the atom, its localization and local environment. The values of total DOS at the Fermi level (EF) are equal to 10.589, 25.184, 20.705 and 17.502 states/(eV f.u.) for $x = 0$, 1, 22 and 23, respectively. Because of a large number of d electrons that type of electrons provides the main contribution to the total DOS for E = E_F: about 90%. The exact values of site and l-decomposed spin-projected DOS at the Fermi level are collected in Table 2.

The calculated total magnetic moments for Fe$_{23}$B$_6$ and Ni$_{23}$B$_6$ compounds are equal to 48.758 and 0.742 μ_B/f.u. Local contributions provided by particular atoms are collected in Table 3.

Particularly high values of magnetic moments, for Fe$_{23}$B$_6$, are located on Fe(4a) and Fe(8c) atoms, higher than for the bulk *bcc*-Fe system (about 2.2 μ_B/atom). The values of magnetic moments depend on the local environment of Fe atoms. Increasing number of the neighbouring boron atoms reduces the magnetic moment of iron. In the case of Ni$_{23}$B$_6$ compound, the magnetic moments are reduced almost to zero, below 3×10^{-4} μ_B/atom.

Table 2. DOS at the Fermi level (states/(eV spin (atom or f.u.)))
of $Fe_{23-x}Ni_xB_6$ compounds ($x = 0$, 1, 22 and 23)

Atom (position)	Site and spin projected DOS (per atom)		Type of DOS	Total and l-decomposed spin projected DOS (per f.u.)	
	spin ↑	spin ↓		spin ↑	spin ↓
$Fe_{23}B_6$:			Total	6.577	4.012
Fe (4a)	0.227	0.140			
Fe (8c)	0.239	0.104	Total for:		
Fe (48h)	0.270	0.176	s electrons	0.310	0.030
Fe (32f)	0.281	0.182	p electrons	0.923	0.147
B (24e)	0.064	0.016	d electrons	5.344	3.835
$Fe_{22}NiB_6$:			Total	8.744	11.920
Ni (4a)	0.377	1.182			
Fe (8c)	0.308	0.534	Total for:		
Fe (48h)	0.363	0.477	s electrons	0.369	0.087
Fe (32f)	0.366	0.455	p electrons	1.074	0.742
B (24e)	0.079	0.051	d electrons	7.298	11.099
$Ni_{22}FeB_6$:			Total	9.570	11.135
Ni (4a)	0.245	0.997			
Ni (8c-1)	0.648	0.652	Total for:		
Ni (8c-2)	0.603	0.785	s electrons	0.240	0.226
Ni (48h-1)	0.394	0.410	p electrons	0.724	0.681
Ni (48h-2)	0.398	0.476	d electrons	8.606	10.228
Ni (48h-3)	0.389	0.407			
Ni (32f-1)	0.244	0.239			
Ni (32f-2)	0.251	0.266			
Ni (32f-3)	0.301	0.355			
Fe (32f)	1.091	1.211			
B (24e-1)	0.059	0.050			
B (24e-2)	0.060	0.043			
$Ni_{23}B_6$:			Total	8.751	8.751
Ni (4a)	0.253	0.253			
Ni (8c)	0.646	0.646	Total for:		
Ni (48h)	0.400	0.400	s electrons	0.228	0.228
Ni (32f)	0.253	0.253	p electrons	0.906	0.906
B (24e)	0.064	0.064	d electrons	7.617	7.617

Table 3. Local magnetic moments for Fe, Ni, and B atoms in $Fe_{23-x}Ni_xB_6$ compounds ($x = 0, 1, 22$ and 23)

Compound	Magnetic moments [μ_B/atom] for given position				
	4a	8c	48h	32f	24e
$Fe_{23}B_6$	2.982	2.553	2.222	1.877	−0.167
$Fe_{22}NiB_6$	0.719(Ni)	2.512 (Fe)	2.198 (Fe)	1.829 (Fe)	−0.168
$Ni_{22}FeB_6$	0.140	0.186 (1/2) 0.077 (1/2)	0.053 (1/2) 0.044 (1/4) 0.032 (1/4)	0.008 (Ni; 1/8) 0.575 (Fe: 1/8) 0.024 (Ni; 3/8) 0.045 (Ni; 3/8)	−0.010 (1/2) −0.002 (1/2)
$Ni_{23}B_6$	0.000	0.000	0.000	0.000	0.000

6. Conclusions

Band structure calculations showed that the local magnetic moments of Fe and Ni atoms in $Fe_{23}B_6$ and $Ni_{23}B_6$ compounds depend on their local environments. The iron magnetic moments are enhanced up to about 3 μB/atom, being reduced for nickel, even to zero. Calculations of the total energy show that in $Fe_{22}NiB_6$ the Ni atoms are located in the 4a position and in $Ni_{22}FeB_6$ the Fe atoms preferably locate at 32f sites. The investigations presented in this contribution will be continued for all x substitutions in $(Fe_{1-x}Ni_x)_{23}B_6$ systems to determine the dependence of magnetization on concentration of Ni impurities and their site preference.

In the nanocrystalline state, Ni-rich alloys show good mechanical properties compared with the FINEMET, NANOPERM or HITPERM. The improved magnetic properties and reduced brittleness of the samples offer attractive possibilities for applications of this alloy. It is of particular interest to study such alloys and to attempt understanding details of the complex crystallization process leading to the formation of new *fcc*-based soft magnetic nanostructured alloys.

References

[1] YOSHIZAWA Y., OGUMA S., YAMAUCHI K., J. Appl. Phys., 64 (1988), 6044.
[2] SUZUKI K., KTAOKA N., INOUE A., MAKINO A., MASUMOTO T., Mat. Trans. JIM, 31 (1990), 743.
[3] WILLARD M.A., LAUGHLIN D.E., MCHENRY M.E., THOMA D., SICKAFUS K., CROSS J.O., HARRIS V.G., J. Appl. Phys., 84 (1998), 6773.
[4] HERZER G., Phys. Scr., T49 (1993), 307.
[5] MIZGALSKI K.P., INAL O.T., YOST F.G., KARNOWSKY M.M., J. Mater. Sci., 16 (1981), 3357.
[6] LI J., SU Z., WANG T.M, GE S.H., HAHN H., SHIARI Y., J. Mater. Sci., 34 (1999), 111.

[7] NAKAMURA T., KOSHIBA H., IMAFUKU M., INOUE A., MATSUBARA E., Mater. Trans., 43 (2002), 1918.

[8] KONDORO J.W., CAMPBELL S.J., Hyperfine Inter., 55 (1990), 993.

[9] ŚLAWSKA-WANIEWSKA A., GRENECHE J.M., Phys. Rev., B56 (1997), R8491.

[10] ANDERSEN O.K., JEPSEN O., ŠOB M., *Electronic Structure and its Applications*, M.Yussouff (Ed.), Springer, Berlin (1987), p. 2.

[11] KRIER G., JEPSEN O., BURKHARDT ANDERSEN O.K., *The TB-LMTO-ASA Program (source code, version 4.7)*.

[12] KHAN Y., WIBBEKE H., Z. Metalkd., 82 (1991), 703.

[13] AYEL M., RIVIERE R., MONNIER G., Compt. Rend., 264C (1967), 862.

[14] MIN B.I., JANG Y.-R., J. Phys.: Condens. Matter, 3 (1991), 5131.

[15] BARTH U., HEDIN L., J. Phys., C5 (1972), 1629.

[16] BLÖCHL P., JEPSEN O., ANDERSEN O.K., Phys. Rev., B49 (1994), 16223.

Effective magnetostriction in nanocrystalline alloys

A. ŚLAWSKA-WANIEWSKA[*]

Institute of Physics, Polish Academy of Sciences, al. Lotników 32/46, 02-668 Warszawa, Poland

Magnetostriction is one of the most important properties of magnetic materials considering both basic research and technical applications. In this paper, a review of the experimental results (both of the crystalline fraction and temperature) and theoretical models (two-component and three-component Reuss-type approximations as well as the effective-medium model) of the magnetostriction in soft magnetic nanocrystalline alloys is presented.

Key words: *nanocrystalline materials; magnetostriction; interfaces, soft magnets*

1. Introduction

Nanocrystalline alloys, produced by the controlled devitrification of the amorphous ribbons, are composed of two main magnetic phases – nano-sized crystallites embedded in a residual amorphous matrix. They exhibit exceptionally soft magnetic properties, which arise from a substantially reduced magnetic anisotropy as well as a very small effective saturation magnetostriction [1–3]. The interpretation of the magnetostrictive effects in such heterogeneous magnetic systems is a difficult problem: the properties of respective phases, complex states of the internal stresses and strains as well as magnetoelastic interactions and high density of topological defects arising at the interfaces should be considered.

In the paper, experimental results of the effective magnetostriction in the nanocrystalline alloys as well as the review of the existing phenomenological models, which are usually used to interpret the experimental dependencies, are presented.

2. Phenomenological models of the effective magnetostriction

The simplest model of the effective magnetostriction of alloys at the different stages of crystallization has been proposed by Herzer [2, 3]. It is based on the Reuss-

---

[*] E-mail: slaws@ifpan.edu.pl.

type approximation, which assumes that the stress is the same in the whole material, both in the particles and in the matrix. In this model, the effective magnetostriction λ_s^{eff} is interpreted as a volumetrically weighted balance between the positive contribution from the residual amorphous matrix and the negative one from the crystallites according to

$$\lambda_s^{\text{eff}} = p\lambda_s^{cr} + (1-p)\lambda_s^{am} \tag{1}$$

where p is the volume fraction of the crystalline phase and λ_s^{am} and λ_s^{cr} are the saturation magnetostrictions of the amorphous and crystalline phases, respectively. However, the changes in composition of the residual amorphous phase, which occur with the evolution of the crystalline fraction (leading to its enrichment with B and Nb or Zr), indicate that λ_s^{am} is not a constant value, but it is in fact a function of p. Moreover, in the Finemet-type alloys, the composition of Fe–Si crystallites, created under various annealing conditions, can be different and, therefore different λ_s^{cr} values, corresponding to the appropriate Si concentration, should be considered. The $\lambda_s^{am}(p)$ values can be found either from the measurements of the amorphous materials with the composition similar to that estimated for the residual amorphous matrix [4] or from phenomenological models [5, 6]. In the latter case, Eq. (1) can be presented in the form [6]

$$\lambda_s^{\text{eff}} = p\lambda_s^{cr} + (1-p)\left(\lambda_{so}^{am} + kp\right) \tag{2}$$

where λ_{so}^{am} is the saturation magnetostriction of the amorphous precursor and k is the parameter that expresses changes of the magnetostriction in the residual amorphous phase with the evolution of the crystalline phase.

It should be noted that this simple two-component Reuss-type approximation ignores the effects connected with the reduction of size of such systems to the nanoscale and relevant to the matter in hand, an increasing role of the interfaces. As was shown by means of the Mössbauer spectroscopy [7, 8], the properties of atoms at the interfaces differ from those located inside the crystalline and amorphous phases. In the nanocrystalline alloys, the interfacial atoms, having neither short nor long range order, create in fact an additional phase which is characterized by a high density of topological defects. When the size of the crystallites decreases, their surface-to-volume ratio dramatically increases and then the atoms situated at the interfaces play important and sometimes even dominant role in the overall behaviour of the material.

The existence of the interfacial phase in the nanocrystalline alloys, where the magnetoelastic coupling differs from those in the bulk of the two main constituent phases, as confirmed by theoretical modelling [9], led to the modification of the simple model by introducing into Eq. (2) the term that describes the interfacial contribution and depends on the surface-to-volume ratio S/V for individual crystallites [10–12]

$$\lambda_s^{\text{eff}} = p\lambda_s^{cr} + (1-p)(\lambda_{so}^{am} + kp) + p\lambda_s^s \frac{S}{V} \tag{3}$$

where λ_s^s is the saturation magnetostriction of the interfacial layer.

For spherical grains, with the average radius R, Eq. (3) transforms to the form

$$\lambda_s^{\text{eff}} = p\lambda_s^{cr} + (1-p)(\lambda_{so}^{am} + kp) + 3p\frac{\lambda_s^s}{R} \tag{4}$$

In this approximation, just as in the simplest model, the stresses are assumed to be the same in all phases, which is not exactly fulfilled in the nanostructures considered. Moreover, the interfacial magnetostriction constant λ_s^s used in this model was introduced by analogy to the surface magnetostriction considered for thin films and superlattices and it has the units of length [13]. The question remains whether the thickness of the interfacial layer, which is a parameter well estimated e.g. by means of the Mössbauer spectroscopy, should also be considered in this model.

The most general approach to the analysis of the effective magnetostriction in the nanocrystalline alloys has recently been proposed by Ce-Wen Nan et al. [14] who assumed that additional magnetoelastic stresses are localised at the surface of the crystallites, due to their limited radius. In this model, the interface regions surrounding the crystallites are considered as clusters of atoms having various interatomic distances. The interfacial effects are described using an effective-medium type method based on the Green-function technique [15]. It has been shown that, assuming the equal shear moduli in the whole material, the effective magnetostriction of the nanocrystalline magnetic system can be described as

$$\lambda_s^{\text{eff}} = p\left[1 - \left(\frac{3\delta}{R}\right)^2\right]\lambda_s^{cr} + \left[1 - \frac{3\delta}{R}\right]\lambda_s^{am} + p\left(1 + \frac{3\delta}{R}\right)\frac{3\delta}{R}\lambda_s^i \tag{5}$$

where δ is the thickness of the interfacial layer and λ_s^i is its saturation magnetostriction with $\lambda_s^s = \delta\lambda_s^i$. If the thickness of the interfacial layer is negligibly small in comparison with the particle radius, i.e. $\delta/R \to 0$, this equation reduces to the three-component Reuss-type approximation given by Eq. (4).

3. Experimental results

3.1. Dependence of the effective magnetostriction on the crystalline fraction

The most widely studied nanocrystalline materials are the Finemet-type (Fe–Nb–Cu–Si–B) and Nanoperm-type (Fe–Zr–B–Cu) alloys. The typical room-temperature

experimental data for the effective magnetostriction in these alloys show that in the as-quenched state and after annealing at sufficiently low temperature (after structural relaxation) the saturation magnetostriction is positive and it is around $(20–30)\times10^{-6}$ in Finemet-type alloys [1–3] and $(2–8)\times10^{-6}$ in Nanoperm-type ones [10, 16]. After annealing at higher temperature, with the evolution of the crystalline fraction p, the magnetostriction rapidly decreases and in the fully nano-crystallized state it is close to zero. It has been shown that even the simplest two-component approximation, described by Eq. (1), gives a qualitative explanation of the $\lambda_s^{\mathrm{eff}}(p)$ dependencies and a number of room temperature experiments show that λ_s^{eff} is roughly a linear function of p [4, 17]. In turn, more accurate approximation, given by Eq. (2), used by Twarowski et al., revealed a quadratic $\lambda_s^{\mathrm{eff}}(p)$ dependence in $Fe_{73.5}Cu_1Nb_3Si_{15.5}B_7$ nanocrystalline alloys [6]. However, for $Fe_{76.5–x}Cu_1R_xSi_{15.5}B_7$ (R = V, Mo, W, Ta, Nb) alloys and for Fe–Zr–B–(Cu) materials Müller et al. [4, 5] and Ślawska-Waniewska et al. [10], respectively, have shown that the parabolic dependence for the effective magnetostriction does not fit the experimental results of $\lambda_s^{\mathrm{eff}}(p)$ (see also the dotted curve in Fig. 1(b)), indicating that in many cases the effective magnetostriction of nanocrystalline materials cannot be described as a balance between the crystalline and amorphous contributions.
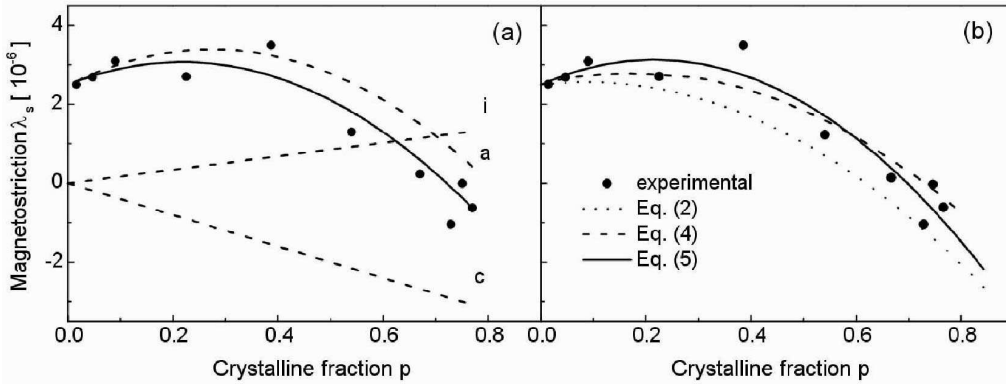
Fig. 1. Effective magnetostriction in $Fe_{85}Zr_7B_6Cu_2$ nanocrystalline alloys vs. crystalline fraction: a) broken lines correspond to crystalline c, amorphous a and interfacial i contributions, solid line calculated from Eq. (4); b) comparison of the experimental data and fitted curves by using two-component Reuss-type approximation (Eq. (2)), three-component Reuss-type approximation (Eq. (4)) and the effective medium model (Eq. (5) [13])

The Reuss-type approximation, which considers the interfacial effects (Eq. (3) or (4)), has been applied to analyse the experimental $\lambda_s^{\mathrm{eff}}(p)$ dependencies measured both in Finemet-type [11, 12] and Nanoperm-type [8,10] alloys. The exemplary results, obtained for $Fe_{85}Zr_7B_6Cu_2$ nanocrystalline samples, are shown in Fig. 1(a). In this figure, the contributions to the effective magnetostriction originating from the individ-

ual phases: crystalline, amorphous and interfacial are shown as broken lines (curve *c*, *a* and *i*, respectively), whereas the solid line represents the fitted $\lambda_s^{\text{eff}}(p)$ curve. In $Fe_{85}Zr_7B_6Cu_2$ nanocrystalline samples, in which the simple α-Fe crystallites are formed, the fitting of the experimental data to Eq. (3) have been performed for $\lambda_s^{cr} = -4\times10^{-6}$ (i.e., the value usually assumed for the polycrystalline iron). The parameters of this fit are as follows: $\lambda_s^s S/V = 1.71\times10^{-6}$, $k = 12.1\times10^{-6}$. The positive value of the *k*-parameter indicates that the magnetostriction of the amorphous phase increases with a decrease of Fe-content, being in an agreement with the experimental results [10]. For spherical crystallites with their radius $R \approx 5$ nm, the magnetostriction constant that describes the interface was estimated to be $\lambda_s^s \approx 2.85\times10^{-6}$ nm.

Interpretation of the $\lambda_s^{\text{eff}}(p)$ dependencies obtained for Finemet-type alloys using the model given by Eq. (4) shows that the value of the magnetostriction constant, which characterizes the crystal-amorphous interface, is in the range of $4.4\times10^{-6} \leq \lambda_s^s \leq 6.1\times10^{-6}$ nm [11, 12].

The model with the effective medium description of interfacial effects, given by Eq. (5), has been applied to the analysis of $\lambda_s^{\text{eff}}(p)$ dependence in the $Fe_{85}Zr_7B_6Cu_2$ nanocrystalline alloys and the results obtained are shown in Fig. 1b – solid line [14]. In this figure, the comparison of the experimental data and $\lambda_s^{\text{eff}}(p)$ curves, calculated using the three models described above (Eq. (2), Eq. (4) and Eq. (5)) is presented. It is seen that the simple balance of the crystallites and amorphous matrix contributions (Eq. (2)) does not appropriately describe the experimental data. The approximation is definitely improved when the interfacial effects are taken into account. The Reuss-type approximation (Eq. (4)) gives a lower estimate for the interface magnetostriction, $\lambda_s^i = \lambda_s^s/\delta \approx 4.5 \times10^{-6}$ (where $\delta = 0.6$ nm, as was shown in [8, 12]) than the effective-medium approach (Eq. (5)) which gives $\lambda_s^i \approx 8\times10^{-6}$ [14]. This difference is mainly caused by the underestimation of the volume fraction of the interface layer by taking $\delta/R \rightarrow 0$ in the former model, which is too rough assumption for the nanostructure studied, where $\delta/R = 0.12$. Though both of these models can well approximate the experimental data, it seems that more reliable values for the interface magnetostriction constant can be obtained from the effective-medium approach.

3.2. Thermal evolution of the effective magnetostriction

The characteristic feature of the temperature dependencies of the effective magnetostriction in Finemet-type alloys is the appearance of a compensation temperature, defined as the temperature at which the magnetostriction becomes zero [6, 18, 19]. The experimental data obtained for selected $Fe_{73.5}Cu_1Nb_3Si_{15.5}B_7$ samples are presented in Fig. 2(a). The most surprising results regarding $\lambda_s^{\text{eff}}(T)$ dependence are

obtained at temperatures above the Curie point of the amorphous matrix $T_C\,(am)$. In-stead of negative magnetostriction, expected from the balance (Eq. (1)) between the negative contribution of Fe-Si grains and vanishing contribution from the residual amorphous matrix, Nielsen et al. [20] revealed that at $T > T_C\,(am)$ the experimentally observed λ_s^{eff} values were either close to zero or positive. This indicated again that the effective magnetostriction of the nanocrystalline materials is more complex than that described by the simple two-component Reuss-type model given by Eq. (1).
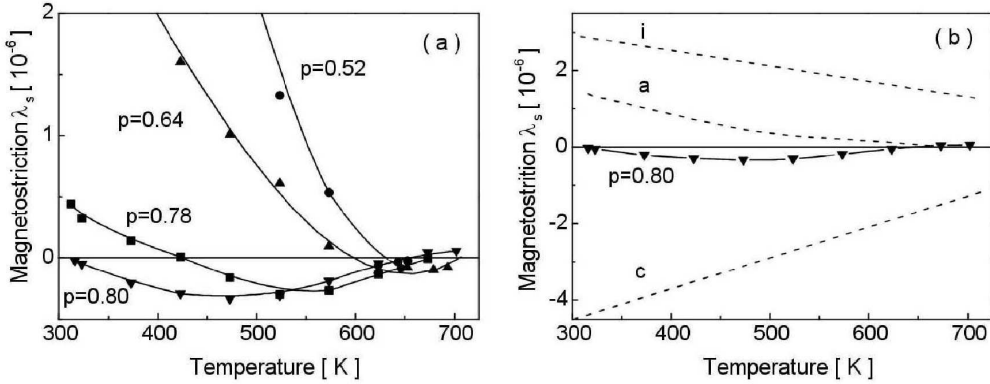

Fig. 2. Temperature dependencies of the effective magnetostriction in $Fe_{73.5}Cu_1Nb_3Si_{15.5}B_7$
nanocrystalline alloys: a) with different crystallite content; b) for $p = 0.80$; broken lines
correspond to crystalline c, amorphous a and interfacial i contributions calculated
by using the three-component Reuss-type approximation (Eq. (4))

The most detailed studies of the thermal evolution of the effective magnetostriction in the Finemet-type alloys were conducted by Grössinger et al. [18, 19] who have also measured the temperature dependencies of the saturation magnetostriction in the micro-crystalline Fe-Si alloys and used these results as reference data to model the behaviour of the crystalline phase in nanocrystalline alloys. The interpretation of the effective magnetostriction was made within the framework of the model described by Eq. (1), whereas the thermal dependencies for the individual components were de-scribed by the critical exponent method. The exemplary experimental data, obtained for $Fe_{73.5}Cu_1Nb_3Si_{16.5}B_6$ nanocrystalline alloy, containing about 78% of $Fe_{80}Si_{20}$ crys-talline phase, as well as those for the micro-crystalline $Fe_{80}Si_{20}$ are shown in Fig. 3a. The apparent magnetostriction of the residual amorphous phase λ_s^{am}, presented in this figure, was calculated from Eq. (1) using for λ_s^{cr} the values obtained for the micro-crystalline counterpart. In this sample, as well as in many other Finemet-type alloys of $Fe_{96-z}Cu_1Nb_3Si_yB_w$ compositions ($y = 14.5, 15.5, 16.5, 17.5, 18.5$ and $w = 5, 7$) with $p(Fe_{80}Si_{20}) \approx 70\%$, Grössinger et al. [18, 19] have found remarkable and positive λ_s^{am} values (Fig. 3b) – at temperatures above the usually determined Curie temperature of

the amorphous phase ($T_c^{am} \sim 575$ K). The observed $\lambda_s^{am}(T)$ behaviour was ascribed to an enhancement of the Curie temperature of the remaining amorphous phase after annealing due to an exchange, driven polarization of the matrix by ferromagnetic grains, postulated by Hernando [21]. A simple linear regression of the $\lambda_s^{am}(T)$ dependencies presented in Fig. 3b indicates that λ_s^{am} does not vanish up to the Curie temperature of the crystalline phase (~870 K) (see the dotted line in Fig. 3a); therefore, the increase of the Curie point of the amorphous phase should exceed 250 K. It ought to be noticed that such an enhancement of T_c^{am}, estimated from the magnetostriction measurements [18, 19], is neither supported by the magnetization nor by Mössbauer spectroscopy measurements and has never been observed in the nanocrystalline alloys.
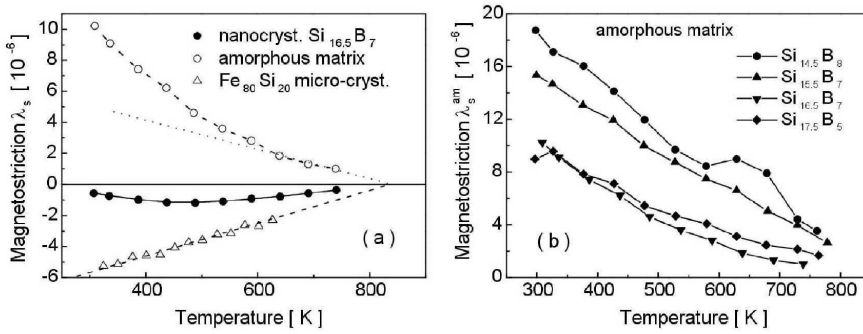

Fig. 3. Temperature dependencies of the saturation magnetostriction:
a) measured in $Fe_{72.5}Cu_1Nb_3Si_{16.5}B_7$ nanocrystalline alloy with $p = 0.74$ (closed circles) [18],
$Fe_{80}Si_{20}$ microcrystalline alloy (open triangles) [19] and λ_s^{am} calculated from Eq. (1) (open circles);
the dotted line represent the possible interfacial magnetostriction; b) of the residual amorphous matrix
calculated from Eq. (1) for $Fe_{96-z}Cu_1Nb_3Si_yB_w$ alloys annealed at 813 K for 1 h (after [18])

The interpretation of the $\lambda_s^{eff}(T)$ dependencies becomes clearer when considering the additional positive contribution from the interfacial phase. Since the interfaces exhibit a magnetic ordering at elevated temperatures (far above the Curie point of the amorphous alloy), as was shown by the Mössbauer spectroscopy investigations [7, 12], this interfacial contribution can account for the observed $\lambda_s^{eff}(T)$ dependencies. The three-component Reuss-type approximation given by Eq. (4) was applied to analyse the experimental data presented in Fig. 2a, and the exemplary results obtained for the sample with $p = 0.8$ are presented in Fig. 2b. The crystalline, amorphous and interfacial contributions are shown as broken lines (curve *c*, *a* and *i*, respectively). The contribution from the crystalline phase was estimated based on the temperature dependence of the saturation magnetostriction reported by Grössinger et al. [18, 19] in $Fe_{80}Si_{20}$ microcrystalline ribbon (see also open triangles in Fig. 3a). The contribution from the inter-

faces was calculated assuming that at a room temperature λ_s^s has a value obtained from $\lambda_s^{\text{eff}}(p)$ fitting in the Finemet-type alloys ($\lambda_s^s \approx 6 \times 10^{-6}$ nm) and decreases with increasing temperature. The contribution from the residual amorphous matrix obtained from the three-component model given by Eq. (4) is small and, moreover, vanishes at $T \approx T_c^{am}$ which seems to have more physical meaning than the $\lambda_s^{am}(T)$ results shown in Fig. 3b and found from the two-component model (Eq. (1)). Considering the above, the apparent large, positive magnetostriction of the amorphous phase $\lambda_s^{am}(T)$, found even at the highest temperatures applied ($T \gg T_c^{am}$) [18, 19] (Fig. 3b), should be interpreted as originating, in fact, from two terms: a contribution from the residual amorphous matrix (much reduced in comparison with the results presented in this figure) and a contribution from the interfacial phase which becomes dominant with increasing temperature and is responsible for the positive values of the effective magnetostriction observed at high temperatures (the dotted line in Fig 3a).

4. Conclusions

Three phenomenological models of the effective magnetostriction in nanoncrystalline alloys are presented: one considers only the crystalline and amorphous matrix contributions and two others take additionally into account a contribution from the interfaces formed at crystallite–matrix boundaries, i.e. the Reuss-type approximation and the effective medium model. Application of these models to the analysis of the experimental dependencies of the effective magnetostriction on the crystalline fraction as well as on the temperature show that the simple two-component model is not sufficient to describe the experimental data and only the models which take into account the interfacial effects can well approximate the dependencies $\lambda_s^{\text{eff}}(p)$ and $\lambda_s^{\text{eff}}(T)$. The most important outcome of the analysis carried out within these models is that the interfacial magnetostriction has positive values, while the saturation magnetostrictions of the corresponding bulk crystals are negative. Although both of these models give satisfactory fitting of the experimental curves, it seems that a more complex model based on the effective medium description, in which local magnetoelastic effects (characteristic of individual phases) as well as the thickness of the interfacial layer are considered, gives more reliable values of the saturation magnetostriction.

References

[1] YOSHIZAWA Y., OGUMA S., YAMAUCHI K.J., Appl. Phys., 64 (1998), 6044.

[2] HERZER G., Mater. Sci. Eng., A133 (1991), 1.

[3] HERZER G., Physica Scripta, T49 (1993), 307.

[4] MÜLLER M., MATTERN N., KÜHN U., J. Magn. Magn. Mater., 157/158 (1996), 209.

[5] MÜLLER M., MATTERN N., J. Magn. Magn. Mater., 136 (1994), 79.

[6] TWAROWSKI K., KUŹMIŃSKI M., ŚLAWSKA-WANIEWSKA A., LACHOWICZ H.K., HERZER G., J. Magn. Magn. Mater., 150 (1995), 85.

[7] ŚLAWSKA-WANIEWSKA A., GRENECHE J.M., Phys. Rev., B 56 (1997), R8491.

[8] ŚLAWSKA-WANIEWSKA A., ROIG A., MOLINS E., GRENECHE J.M., ŻUBEREK R., J. Appl. Phys., 81 (1997), 4652.

[9] SZUMIATA T., ŻUBEREK R., GONZALEZ J., ŚLAWSKA-WANIEWSKA A., SZYMCZAK H., J. Magn. Magn. Mater., 203 (1999), 262.

[10] ŚLAWSKA-WANIEWSKA A., ŻUBEREK R., NOWICKI P., J. Magn. Magn. Mater., 157/158 (1996), 147.

[11] ŚLAWSKA-WANIEWSKA A., ŻUBEREK R., Electron Techn., 31 (1998), 29.

[12] ŚLAWSKA-WANIEWSKA A., J. Phys. IV, 8 (1998), 11.

[13] SZYMCZAK H., ŻUBEREK R., Acta Phys. Polon., A83 (1993), 651.

[14] CE-WEN NAN, JIN H.HUANG, WENG G.J., J. Magn. Magn. Mater., 233 (2001), 219.

[15] CE-WEN NAN, WENG G.J., Phys. Rev., B 60 (1999), 6723.

[16] INOUE A., MIYAUCHI Y., MAKINO A., MASUMOTO T., Mater. Trans. JIM, 37 (1996), 78.

[17] GUTIERREZ J., GORRIA P., BARANDIARAN J.M., GARCIA-ARRIBAS A., *Nanostructured and Non-Crystalline Materials*, World Sci. Publ., Singapore, 1995, p.500.

[18] GRÖSSINGER R., TURTELLI R.S., DUONG V.H., KUSS CH., POLAK CH., HERZER G., Mater. Sci. Forum, 307 (1999), 135.

[19] TURTELLI R.S., DUONG V., GRÖSSINGER R., SCHWETZ M., FERARA E., PILLMAYR N., IEEE Trans. Magn., 36 (2000), 508.

[20] NIELSEN O., PETERSEN J., HERZER G., IEEE Trans. Magn., 30 (1994), 1042.

[21] HERNANDO A., NAVARRO I., GORIA P., Phys. Rev., B 51 (1995), 3281.

Micromagnetic simulation
of multiphase nanocrystalline material
with different boundary conditions

O. NEDELKO[1*], A. ŚLAWSKA-WANIEWSKA[1], Y. LABAYE[2]

[1]Institute of Physics, Polish Academy of Sciences, al. Lotników 32/46, 02-668 Warsaw, Poland

[2]Laboratoire de Physique de l'Etat Condensé, UMR 6087 CNRS,
Université du Maine, F-72085 Le Mans, France

The micromagnetic formalism was used to study the magnetic behaviour of an assembly of single-domain ferromagnetic particles, with random easy axes of anisotropy, embedded in a weakly magnetic matrix. The results for various boundary conditions are compared.

Key words: *micromagnetic simulations; nanocrystalline material; hysteresis loop*

1. Introduction

Numerous magnetic materials used in modern technological applications are composed of fine magnetic particles either isolated or embedded in a non-magnetic or magnetic matrix. The analysis of multiphase systems is a difficult task, which has to include experimental studies as well as theoretical modelling. The complexity of the theoretical description of multiphase magnetic materials usually requires a numerical treatment. One of the possible approaches is the numerical micromagnetics that experiences the renaissance from the early 90th. The mathematical background of the micromagnetics [1] consists in the minimization of the magnetic free energy of a ferromagnetic material under certain conditions. Those "certain conditions" include parameters: (i) of the external environment influence such as applied field, temperature, stress; (ii) of the material (exchange integral, anisotropy constant, saturation magnetisation, etc.); (iii) of the system geometry that describe the sample (and in the case of non-uniform material its inner structure) as well as the boundary conditions for the micromagnetic problem.

---

*Corresponding author, e-mail: nedel@ifpan.edu.pl.

The calculations presented in this paper were performed for a peculiar nanostructure composed of randomly oriented crystalline grains, exhibiting high magnetic moment and strong uniaxial anisotropy, embedded in a weakly magnetic isotropic matrix.

2. Micromagnetic model

The system under consideration is a cube of the edge size D divided into $N{\times}N{\times}N$ cubic elements with the linear size d (see Fig. 1). Our calculations were performed for $N = 32$ or 64 and $d = 7$ nm. Various boundary conditions were considered: free, periodic in two dimensions and periodic in three dimensions. In the case of the free boundaries, the linear sample size is D and can be calculated by simple multiplying the size of the discretisation element by the number of elements, i.e., $D = dN$. However, for periodical boundary conditions the edge size D means the period size of the model and has nothing to deal with the sample physical size. In this case, the cube of linear size D is replicated infinite number of times in two or three dimensions. Thus, the periodical boundary conditions allow us to implement the infinite sample size in the model. The assumption of the "infinite size" gives two main advantages: there are no finite size effects and it is possible to compare the results achieved with experimental data of a corresponding bulk material.
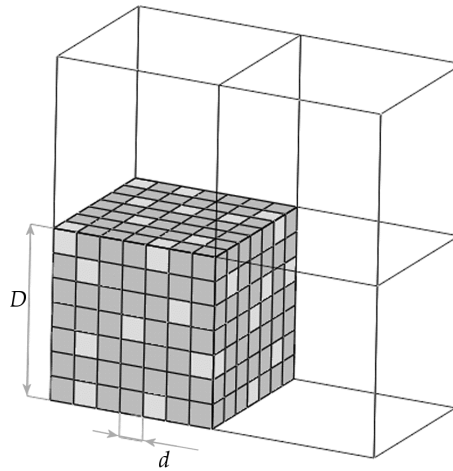

Fig. 1. Cubic discretisation procedure: D is the period size,
d is the size of the discretisation element. Light cubes represent
the grains embedded in matrix which is represented by dark cubes

Here and below, we consider the whole specimen as a finite or infinite regular mesh of closely packed interacting cubic elements [2]; discretisation cubic elements refers to mesh cells.

The mesh used for numerical calculations is a two-phase system that consists of crystalline particles with uniaxial anisotropy randomly embedded in a weakly magnetic isotropic matrix with the 10% packing density of grains. The size of each particle is the same and equals the cell size *d*. The directions of easy axes of particles are generated randomly with a uniform distribution of the direction cosines.

Since the size of the mesh cells is sufficiently small to meet the assumption of the micromagnetics (i.e., it is smaller than the exchange characteristic length), the magnetisation in each of them can be substituted for a classical vector. All calculations are carried out for low temperatures, where the thermal fluctuations can be neglected.

The considered magnetic free-energy functional includes the energy contributions from the field applied, uniaxial anisotropy, exchange and magnetostatic interactions

$$E_{\text{tot}} = E_{\text{app}} + E_{an} + E_{ex} + E_{\text{mag}}$$

The external field energy E_{app} and uniaxial anisotropy energy E_{an} terms are used in their classical forms [3]. The exchange energy is calculated by means of the Heisenberg-like term. The magnetostatic energy contribution E_{mag} is calculated using the explicit expression for demagnetising field presented by Nakatani et al. [4] and summed over the specimen by means of the Fast Fourier Transform (FFT) technique [5] with the aid of numerical routines called the Fastest Fourier Transform in the West [6].

Defining the magnetisation vector in the *i*-th mesh cell as

$$\mathbf{M}_i = M_S^\sigma \mathbf{m}_i$$

where M_S^σ denotes the saturation magnetisation of the σ sort of material, i.e., grain or matrix; $\mathbf{m}_i$ is the unitary vector parallel to magnetisation of the *i*-th cell, the total energy density of a sample in a uniform field applied is a sum of the energy densities of the mesh cells and can be written as

$$e = \sum_i e_i = -\sum_i \left[\left(\mathbf{H}_{\text{app}} \mathbf{M}_i \right) + K_1^\sigma \left(\mathbf{n}_i \mathbf{m}_i \right)^2 + \frac{1}{d^2} \sum_{\delta i} A_{i,\delta i} \left(\mathbf{m}_i \mathbf{m}_{\delta i} \right) - \frac{1}{2} \left(\mathbf{H}_i^D \mathbf{M}_i \right) \right]$$

where $\mathbf{H}_{\text{app}}$ is the applied field, K_1^σ – anisotropy constant and *n* is the easy-axis direction vector; $A_{i,\delta i}$ – exchange constant, where δi means the number of neighbours to the *i*-th node; $\mathbf{H}^D$ – demagnetising field.

The minimization procedure is provided by the Jacobi iterative scheme based on the Landau–Lifshitz equation of motion for magnetic moments without a precession term [7], i.e.

$$\frac{d\mathbf{m}_i}{dt} = -\mathbf{m}_i \times (\mathbf{m}_i \times \mathbf{h}_i^{\text{eff}})$$

where the time scale includes the factor preceding the vector product, and $\mathbf{h}^{\text{eff}}$ is the effective field defined as

$$\mathbf{h}_i^{\text{eff}} = -\frac{\partial e_i}{\partial \mathbf{M}_i}$$

The condition for the equilibrium state of magnetisation is the requirement that for every node the magnetisation vector should be parallel to the appropriate effective field that gives a minimum of the magnetic free energy. Thus, to achieve the equilibrium one should recalculate the effective field and use the Landau–Lifshitz equation to gain the next transition state for each iteration step.

3. Results

The material parameters used for the appropriate calculations are presented in the table. These parameters were chosen so as to approximately correspond to the recently produced and experimentally studied $Co_{66}Nb_9Cu_1Si_{12}B_{12}$ nanocrystalline material, obtained by the isothermal annealing of the amorphous alloy [8]. We have already used this material as a basis for the comparison of numerical results with the experimental data that revealed a good qualitative agreement [9].

Table. Material parameters used for the micromagnetic calculations

	A, erg/cm	K_1, erg/cm^3	M_S, emu/cm^3
Grains	10^{-6}	2.7×10^6	1360
Matrix	0.2×10^{-6}	0	160
Matrix–grain interface	0.2×10^{-6}	–	–

The hysteresis loops obtained for the nanostructure studied in the case of the free boundary conditions as well as periodic in 2 and 3 dimensions are presented in Fig. 2 and Fig. 3 for the mesh sizes $N = 32$ and 64, respectively.

It has been already shown that in such a nanostructure, due to the exchange coupling between the highly anisotropic crystallites and the surrounded isotropic matrix, the material is combined into randomly oriented weakly related clusters [9]. The results of the simulations of magnetisation processes indicate that during the magnetisation reversal process the clusters reverse sequentially in a reversal field, which can be considered as an external field modulated by a magnetostatic field from the neighbouring clusters. For clusters which are preferentially adjacent parallel to the applied field the reversal field is enhanced, whereas for transversally adjacent clusters it is reduced. This results in a step-like shape of the hysteresis loops presented in Figs. 2 and 3. Depending on the strength of the exchange coupling via the grain–matrix interface and the anisotropy constant of the grains, one can obtain a cluster structure that is stable during the whole reversal process (as in this work) or unstable clusters for which the magnetisation of the matrix tears off from the grains in high enough reversal field [9].
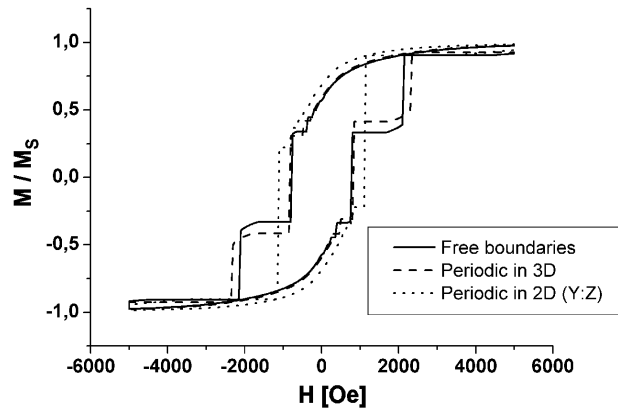
Fig. 2. Hysteresis loops calculated for different boundary conditions.
Sample mesh size is 32×32×32 nodes.
The direction of the external field is parallel to the *z*-axis

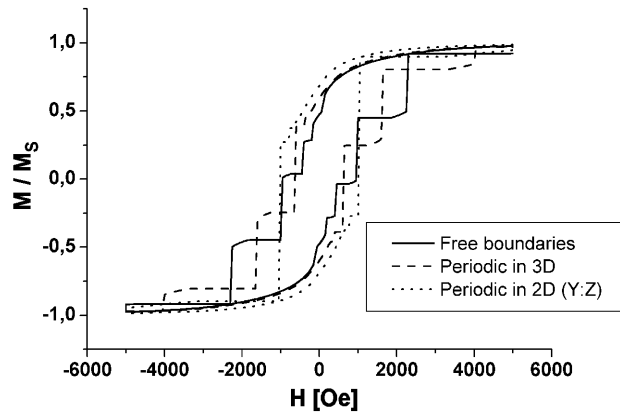
Fig. 3. Hysteresis loops calculated for different boundary conditions.
Sample mesh size is 64×64×64 nodes.
The direction of the external field is parallel to the *z*-axis

For a certain mesh size, the different shapes of the calculated loops are the consequences of the various levels of the finite-size effects. In the case where there is at least one non-periodic dimension, on the free faces of a nano-sample the surface magnetic poles can appear. These additional magnetic poles increase the demagnetising field, which, in turn, modifies the magnetisation reversal. The periodicity removes these finite-size effects, so the resulting hysteresis loop can be compared to the experimental one measured for a macro-sample. The 2*D* periodic boundary conditions can be applied to modelling thin magnetic films. However, this approximation is not sufficient for bulk materials for which the rotational processes, which occur at higher fields, are lost. The increase of the mesh size leads to the refinement of the loop shape due to the improved averaging of the magnetisation over larger number of grains. In

this case, one can obtain a better approximation of the experimental results but, on the other hand, the increase of the mesh size substantially increases the calculation time.

4. Conclusions

It has been shown that the magnetic properties of the system consisting of ferromagnetic particles with high uniaxial anisotropy strongly depend on the magnetic state of the matrix in which they are dispersed. The presence of a small matrix magnetic moment and weak, both in-matrix and matrix-crystallite, exchange couplings lead to cluster-like inner magnetisation patterns. The magnetisation reversal in such nanostructure proceeds by sequential rotation of magnetic moments within the clusters. The shape of the calculated hysteresis loop, which represents this magnetisation process, strongly depends on the boundary conditions, which should carefully be chosen for the simulation of the real experiment.

References

[1] Brown W.F. Jr., *Micromagnetics*, Wiley, New York, 1963.
[2] Della Torre E., IEEE Trans Magn., MAG-22 (1986), 484.
[3] Bertotti G., *Hysteresis in Magnetism*, Academic Press, San Diego, 1998.
[4] Nakatani Y., Uesaka Y., Hayashi N., Jpn. J. Appl. Phys., 28 (1989), 2485.
[5] Hayashi N., Saito K. Nakatani Y., Jpn. J. Appl. Phys., 35 (1996), 6065.
[6] http://www.fftw.org
[7] Berkov D.V., Ramstöck K., Hubert A., Phys. Stat. Sol.(a), 137 (1993), 207.
[8] Didukh P., Nedelko O., Ślawska-Waniewska A., Mater. Sci. Forum, 373–376 (2001), 273.
[9] Nedelko O., Didukh P., Ślawska-Waniewska A., J. Magn. Magn. Mater., 254–255 (2003), 281.

Influence of indium dilution level on magnetic properties and photoconductivity of $Cd_{1-y}Cr_{2-2x}In_{2x+y}Se_4$ magnetic semiconductors

B.T. Cięciwa[*], L.J. Maksymowicz, M. Lubecka,
H. Jankowski, J. Sokulski, Z. Sobków

Department of Electronics, University of Mining and Metallurgy, 30-059 Kraków,
al. Mickiewicza 30, Poland

Magnetic semiconductors of $CdCr_2Se_4$ diluted by indium belong to the class of soft magnetic materials. The amount of indium alters the energetic structure of chalcogenide spinel. For $CdCr_2Se_4$:In magnetic semiconductor the state with reentrant transition (REE) is achieved. In the case of $Cd_{1-y}Cr_{2-2x}In_{2x+y}Se_4$ dilution, the spin glass (SG) state and the randomly canted state is obtained. Chalcogenide spinel could be used as the element of a near-infrared detector. Then the photoconductivity properties – the voltage sensitivity versus the light wavelength – are of interest. This parameter is also affected by the dilution level. The polycrystalline $Cd_{1-y}Cr_{2-2x}In_{2x+y}Se_4$ thin films obtained by rf-sputtering technique were studied. It was found that the dependence of voltage sensitivity of the photoresponse on the wavelength differs significantly for samples with REE and in the SG state. For both types of magnetic ordering, the photoresponse below the critical magnetic temperature is larger than above it.

Key words: *magnetic semiconductor; reentrant transition; spin glass; photoconductivity*

1. Introduction

The energy-band structure of $CdCr_2Se_4$ magnetic semiconductors is influenced by long-range magnetic order. The top of the valence band and the bottom of the conduction band are split due to "spin up" and "spin down" configurations (Fig. 1) [1]. There is a non-zero density of states in the forbidden gap of the doped $CdCr_2Se_4$: In, which is presented in Fig. 2 [2]. From the experiment data it is known that the samples:

- $CdCr_2Se_4$ and $CdCr_2Se_4$: In are in the state with reentrant transition (REE),
- $CdCr_{2-2x}In_{2x}Se_4$ (In substitutes Cr) are in spin glass state (SG),
- $Cd_{1-y}In_yCr_2Se_4$ (In substitutes Cd) are in spin glass state,
- $Cd_{1-y}Cr_{2-2x}In_{2x+y}Se_4$ (In substitutes Cd and Cr) are in the randomly canted state [3, 4].

_____

[*]Corresponding author, e-mail: bcieciwa@agh.edu.pl.
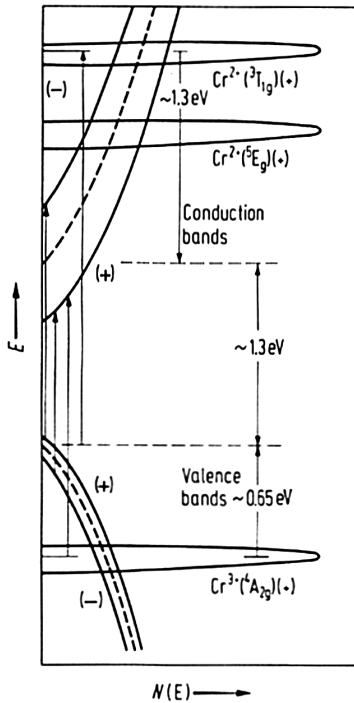
Fig. 1. Energy level diagram of CdCr$_2$Se$_4$ at $T < T_c$ [1]. Conduction and valence bands at $T > T_c$ are indicated by dashed lines
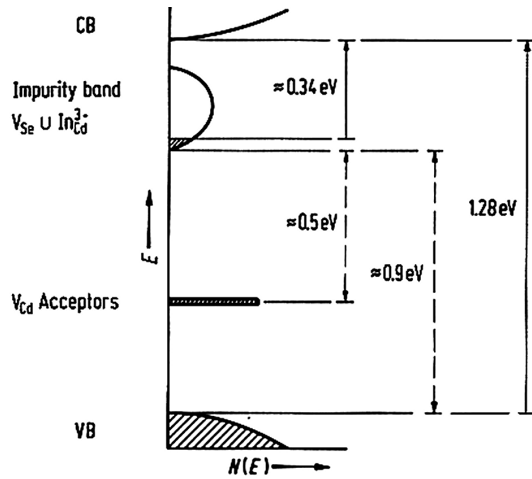
Fig. 2. Tentative energy level diagram at $T = 80$ K for In-doped n-type CdCr$_2$Se$_4$ [2]. $N(E)$ is the density of states, V_{Cd} is the Cd vacancy. Impurity band is formed by Se vacancies and In^{3+} ions on Cd-lattice sites

We investigated thin films of chalcogenide magnetic semiconductors obtained by the rf-sputtering technique. The magnetic state was classified based on the temperature dependence of the magnetization M and unidirectional magnetic anisotropy H_{an}. Both parameters were determined from the ferromagnetic resonance experiments (FMR).

The modified energetic structure affects the character of voltage sensitivity in the photoconductivity measurements. The photoconductivity measurements were carried out in the temperature range of 77–300 K. A different behaviour of a voltage sensitivity for the magnetic semiconductors with REE transition in comparison with the samples in SG state was observed.

2. Experiment

The chalcogenide semiconductor thin-film layers were fabricated by the co-sputtering from the three powdered cathodes (CdSe, Cr, Cr$_2$Se$_3$) on Corning glass substrates with controlled temperature. The dilution level was controlled with the amount of uniformly spotted pieces of In$_2$Se$_3$ on the Cr$_2$Se$_3$ cathode. Polycrystalline

layers were obtained after a heat treatment process. Composition of the samples was analysed using X-ray microprobe and the thickness was measured with Talysurf 4 profilometer. Samples were 300–800 nm thick. The technology details are presented in the paper [5]. The samples of CdCr$_{2-2x}$In$_{2x}$Se$_4$ thin films with $0 < 2x < 0.70$ and $y = 0$ have been investigated. The results for samples with $y > 0$ were presented earlier [3].

The dependencies of magnetization M and of unidirectional magnetic anisotropy field H_{an} on temperature were considered as the criteria of magnetic ordering. Both magnetic parameters were determined from the ferromagnetic resonance (FMR) data at X-band for perpendicular and parallel geometry and for temperature range from 4 to 125 K. The dispersion relation for uniform mode has the form [6]:

• for the perpendicular geometry (the external magnetic field is perpendicular to the film plane)

$$\frac{\omega}{\gamma} = H_\perp + H_{an} - 4\pi M \tag{1}$$

• for the parallel geometry (the external magnetic field is within the film plane)

$$\left(\frac{\omega}{\gamma}\right)^2 = (H_{\rm II} + H_{an})(H_{\rm II} + H_{an} + 4\pi M) \tag{2}$$

where $\omega = 2\pi\nu$, ν – the microwave frequency, γ – the gyromagnetic factor, $H_\perp$ and $H_{\rm II}$ – resonance fields of the uniform mode for the perpendicular and parallel geometry, respectively. Both equations are applied to determine $M(T)$ and $H_{an}(T)$ when the temperature dependencies of $H_\perp$ and $H_{\rm II}$ are known.
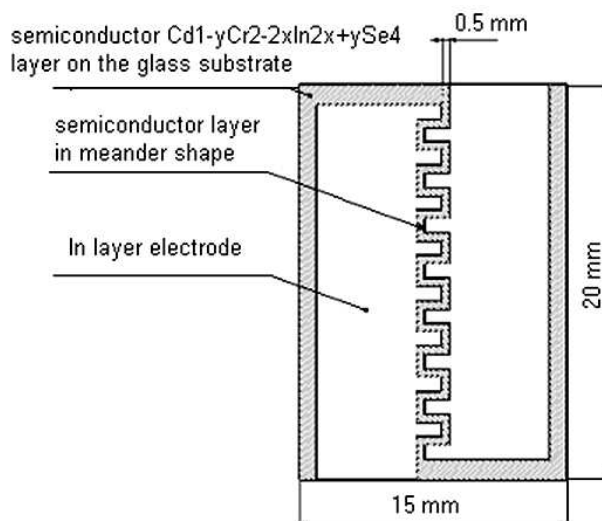

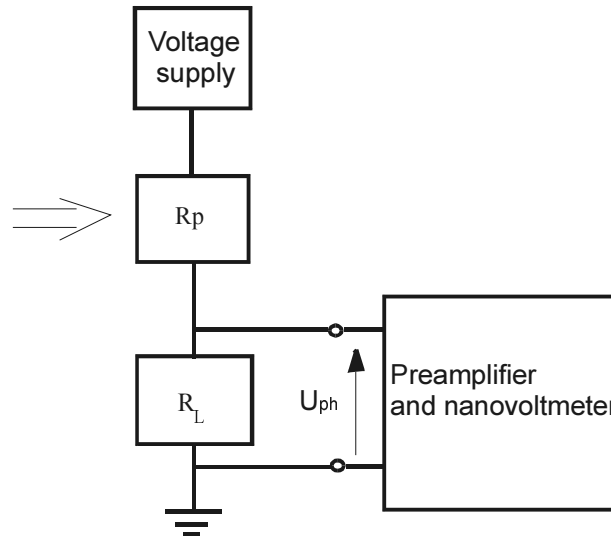Fig. 3. Thin film sample with the indium electrodes system

Fig. 4. Scheme of the voltage photoresponse measurements

To prepare the sample for the photoconductivity measurements, indium electrodes were carefully placed on the samples. Indium layer was evaporated on the semiconductor thin film to obtain a proper meander shape (Fig. 3). Such an action lowers the resistance R_p of the samples, which is important in a photoresponse signal. The photosignal was detected as a voltage response U_{ph} on the load resistor R_L, as is shown in Fig. 4. The illuminating light within the wavelength range from 400 nm to 1000 nm was chopped with the frequency of 90 Hz. The measurements were carried out under the condition $R_L = R_p$. The samples of 0.02–2 MΩ resistance (at 298 K) were biased with 30 V voltage. The temperature was changed from 77 K to 300 K. The voltage photo-signal was detected using a Selective Nanovoltmeter Lock-in SR830.

3. Results

The temperature dependencies of magnetization M and the unidirectional magnetic anisotropy field H_{an} obtained from the FMR experiment at X-band for thin films of CdCr$_2$Se$_4$:In (REE) and CdCr$_{1.7}$In$_{0.3}$Se$_4$ (SG) are shown in Figs. 5 and 6. Spectral sensitivity R_v of the voltage response is obtained from the photoconductivity measurements of the Cd$_{1-y}$Cr$_{2-2x}$In$_{2x+y}$Se$_4$ thin films. The data for CdCr$_2$Se$_4$:In (REE) and CdCr$_{1.9}$In$_{0.1}$Se$_4$ (SG) are presented. The experimental data are illustrated as a voltage sensitivity of the photoresponse vs. the wavelength (Figs. 7a 7b) for different temperatures. The transitions are indicated in the figures with dotted lines. The differences in the character of spectral sensitivity are observed depending on the temperature. Figures 8a and 8b present the voltage sensitivities for the temperatures $T < T_c$ and $T > T_c$, respectively.
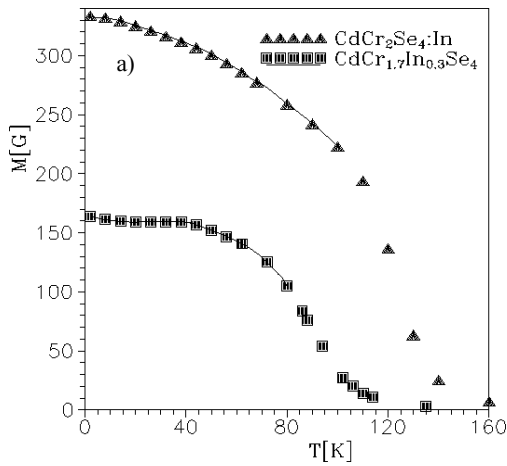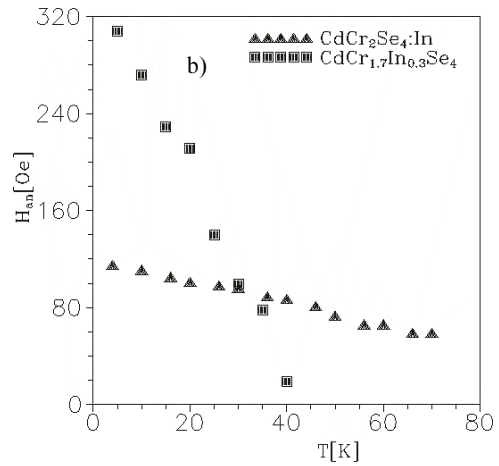
Fig. 5. Dependence of magnetization on temperature
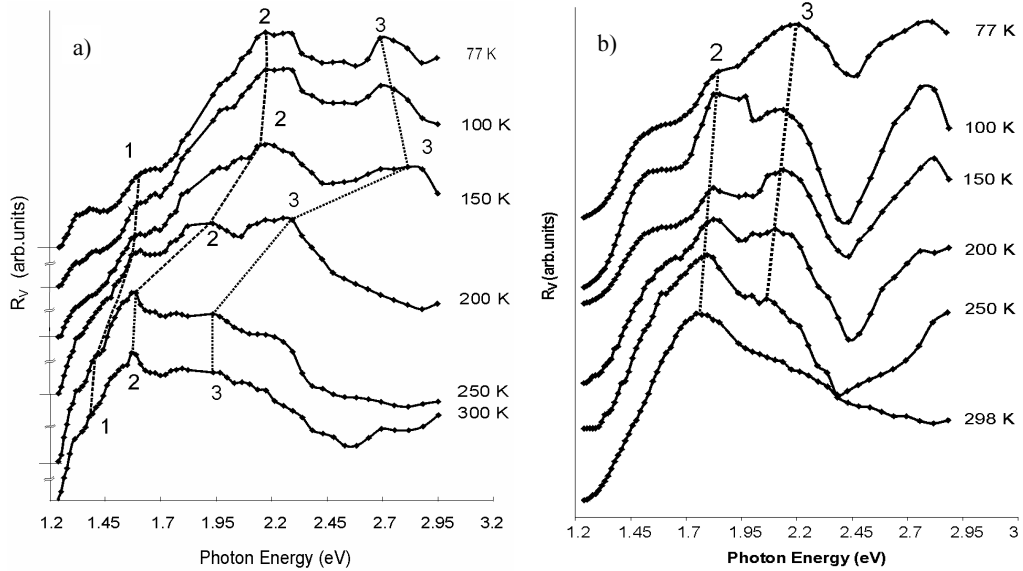

Fig. 6. Dependence of H_{an} on temperature

Fig. 7. The voltage sensitivity vs. the photon energy of the incident light for:
a) the undoped $CdCr_2Se_4$ thin film, b) the $CdCr_{1.9}In_{0.1}Se_4$ thin film

4. Discussion

4.1. Magnetic parameters

For both types of magnetic ordering (REE and SG), the dependence of magnetization on temperature does not obey the Bloch law. For the state with REE transition,

the Bloch law is modified due to a non-zero density of states in the energy gap. The dependence of magnetization on temperature is described by Eq. (3) [6]

$$\frac{M(0) - M(T)}{(0)} = BT^{3/2} \sum_{n=1}^{\infty} \frac{\exp(-n\Delta_r / k_B T)}{n^{3/2}} \tag{3}$$

where:

$$B = \xi \cdot \frac{3}{2} \cdot \frac{g\mu_B}{M(0)} \cdot \left(\frac{k_B}{4\pi D}\right)^{3/2}$$

$\xi \cdot (3/2)$ stands for the Riemann ξ-function, Δ_r is the energy gap and D is the spin-wave stiffness constant.
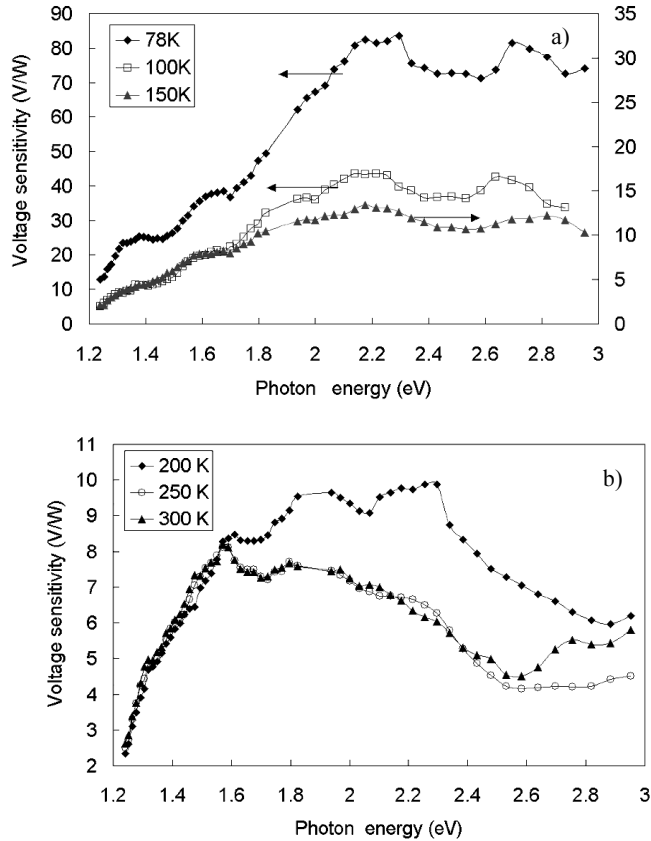

Fig. 8. The voltage sensitivity of the undoped CdCr$_2$Se$_4$ thin film (REE):
a) for the temperatures below the Curie temperature, b) for the temperatures higher than T_c

For the SG state, the dependence $M(T)$ is described by the equation

$$\frac{M(0) - M(T)}{M(0)} = \frac{C_S}{\exp(\Delta_S / kT) - 1} \qquad (4)$$

where C_s is responsible for the density of states in the energy gap and Δ_S is a measure of the intercluster interaction. The temperature dependence of magnetization presented in Fig. 5 is in a good agreement with the theoretical prediction for samples with REE transition CdCr$_2$Se$_4$:In and also for CdCr$_{1.7}$In$_{0.3}$Se$_4$ SG state. Following Eq. (3), the theoretical calculations for REE are presented for fitting parameters $M(0)$ = 330 G and Δ_r = 10 K, while for SG (Eq. (4)) $M(0)$ = 162 G, C_s = 11.8 and Δ_s = 270 K. The values of $M(T)$ calculated theoretically are represented by solid lines. It is seen in Fig. 6 that the unidirectional magnetic anisotropy field H_{an} in CdCr$_{2-2x}$In$_{2x}$Se$_4$ thin films decreases with increasing temperature and depends on the amount of In (H_{an} increases with increasing dilution level). H_{an} depends on the field-induced remanent magnetization and keeps the direction of the cooling field, which means that the spins have some memory of the cooling field direction. H_{an} is influenced by the dilution level and, being related to the induced magnetization, is also temperature-dependent. The dependence $H_{an}(T)$ is available only from the experimental data, since no comprehensive theoretical model of the temperature dependence of H_{an} is known.

4.2. Photoconductivity

The voltage sensitivity of undoped CdCr$_2$Se$_4$ thin films (REE) is presented in Fig. 7a. The transition is marked by three lines: for the energy about 1.6 eV (line 1), for the energy about 2.2 eV (line 2) and for the energy about 2.7 eV (line 3). Line 1 exhibits a blue shift. Line 2 also exhibits a blue shift which is significant for $T > T_c$. Line 3 exhibits a more complicated energy transition: we have a blue shift for $T > T_c$ and a red shift for $T < T_c$. The voltage sensitivity of diluted (SG) samples, CdCr$_{1.9}$In$_{0.1}$Se$_4$, is presented in Fig. 7b. Two transitions are observed for the energy about 1.8 (line 1) and 2.2 eV (line 2). For both cases a blue shift is observed.

Those shifts for samples with REE transition as well as for the samples with SG state result from a mechanism related to the magnetic ordering and interatomic exchange interaction [7–9].

For all samples investigated, the spectral response – voltage sensitivity is about one order of magnitude higher below the Curie temperature than above T_c. As an example, we present the data for the sample with REE transition (Figs 8a, b). For the potential application as the photodetectors, magnetic semicondutors working below T_c could be taken into consideration. The voltage sensitivity and its maximum are influenced by the dilution level.

5. Conclusions

Magnetic semiconductors of $Cd_{1-y}Cr_{2-2x}In_{2x+y}Se_4$ chalcogenide spinel exhibit different types of magnetic ordering, depending on the dilution level. For the samples $CdCr_2Se_4$: In, the state with REE is obtained, for diluted samples an SG state appears. We classify the magnetic states of thin films of $Cd_{1-y}Cr_{2-2x}In_{2x+y}Se_4$ based on the dependence of the magnetization and the unidirectional magnetic anisotropy field on the temperature and concentration.

The photoconductivity measurements show the influence of the type of magnetic ordering on the character of voltage sensitivity. We can conclude from our experimental results that the voltage sensitivity is higher in the case of state with reentrant transition than for the spin glass state. These differences are more pronounced below the critical magnetic temperature.

The voltage sensitivity exhibits its maximum at different energies, depending on the temperature: it appears in the high-energy region below T_c shifting towards lower energies above T_c. The exchange interactions in the magnetic semiconductor result in shifts of the energy transitions when the temperature changes. When the amount of indium increases, the maximum sensitivity shifts to the higher energies. Finally we can conclude that there is a possibility of controlling parameters of $CdCr_{2-2x}In_{2x}Se_4$ near-infrared detectors with the temperature and dilution level.

References

[1] TANIGUCHI M., KATO Y., NARITA S., Solid State Commun., 16 (1975), 261.

[2] TREITINGER L., BRENDECKE H., Mater Res. Bull., 12 (1977), 1021.

[3] MAKSYMOWICZ L.J., LUBECKA M., SZYMCZAK R., POWROŹNIK W., JANKOWSKI H., J. Magn. Magn. Mater., 242 (2002), 924.

[4] DORMANN J.L., NOGUES M., Phase Trans., 33 (1991), 159.

[5] MAKSYMOWICZ L.J., LUBECKA M., CIĘCIWA B. T., J. Magn. Magn. Mater., 192 (1999).

[6] JACKSON E.M., LIO S.B., BHAGAT S.M., MANHEIMER M.A., J. Magn. Magn. Mater., 80 (1989), 229.

[7] RYS F., HELMAN J., BALTENSPERGER W., Phys. Condensed Matter, 6 (1967), 105.

[8] CALLEN E., Phys. Rev. Lett., 20 (1968), 1045.

[9] SATO K., TERANISHI T., J. Phys. Soc. Japan, 29 (1970), 523.

[10] AMITH A., BERGER S.B., J Appl. Phys., 42 (1971), 1472.

Magnetic properties of the RMn$_{12-x}$T$_x$ alloys in high magnetic field[*]

W. SUSKI[1, 2**], B. BELAN[3], A. GILEWSKI[1], T. MYDLARZ[1], K. WOCHOWSKI[2]

[1]International Laboratory of High Magnetic Fields and Low Temperatures,
ul. Gajowicka 95, 53-421 Wrocław, Poland

[2]Polish Academy of Science, Włodzimierz Trzebiatowski Institute of Low Temperature and Structure
Research, P.O. Box 1410, 50-950 Wrocław 2, Poland

[3]Department of Inorganic Chemistry, Ivan Franko National University of L'viv, 79005 L'viv, Ukraine

The structure and magnetic properties of the tetragonal ThMn$_{12}$-type RMn$_{12-x}$T$_x$ alloys (R = Nd, Sm; T = Co, Ni) have been studied over a broad range of magnetic fields (up to 35 T). A high-pulsed magnetic field is applied at T = 4.2 K with the pulse duration of 10 ms. The NdMn$_{12-x}$Ni$_x$ system has been additionally investigated in the temperature range extended up to about 750 K. The ternaries exist in, approximately, the $4 \leq x \leq 8$ composition range. The alloys with x ~4 are frequently paramagnetic in a broad temperature range, whereas for other compositions, complex magnetic properties are observed. The results are discussed in relation to the free-ion values of the Nd and Sm ions.

Key words: *rare-earth intermetallics; magnetic properties; high magnetic field*

1. Introduction

Considerable attention has recently been paid to intermetallic compounds of rare-earth elements R and 3d magnetic transition metals T. because of a possibility of their application, e.g. due to their favourable magnetic properties, or as hydrogen accumulators. Compounds with the ThMn$_{12}$-type tetragonal structure (space group *I*4/*mmm*) belong to such materials. Alloys with nominal composition RNi$_{12}$ or RCo$_{12}$ do not exist, but can be stabilized by a partial substitution of Ni or Co by a transition metal with a lower valence-electron density, or the p-elements such as Si or Al (for review see Ref. [1]). In these ternary compounds, the R atoms occupy the 2a sites, whereas the 3d-transition elements occupy remaining 8f, 8i and 8j positions. In contrast to the mostly paramagnetic character

---

of nickel-rich compounds, cobalt-rich compounds are usually ferro- or ferrimagnetic, whereas the parent RMn_{12} compounds exhibit non-collinear antiferromagnetic ordering at low temperature [2] if R is non-magnetic Y. The transition temperature of YMn_{12} has been confirmed by electrical measurements [3]. It is remarkable that different Mn sites with their different Mn moments, as reported in neutron diffraction (ND) experiments [2], do not appear in μSR spectra [4]. However, if R is a heavy rare-earth atom, ferrimagnetic properties are observed [5–7]. Consequently, a complex magnetic behaviour is expected to occur in $RMn_{12-x}T_x$ solid solutions as a result of competing ferro- and antiferromagnetic interactions. The magnetic and electrical properties of compounds with Fe as a transition element and with heavier rare earths or with Y and Nd are reported in Ref. [8–17] (and in references herein).

Brief information about selected Co compounds has been presented in [12, 14, 18], whereas a more systematic study of those intermetallics has been reported (for Nd and Sm) in [19]. In all the materials mentioned above, within a limited composition range, three magnetic sublattices exist (R, Mn and Co), while in the whole concentration range x, a magnetic ordering is observed at least in two sublattices (R and Co). Until now, only few papers have been published on ternaries containing Ni, which turned out to be non-magnetic in these alloys [20]. Particularly interesting is the case of $SmMn_{12-x}Ni_x$ compounds [21] for which the temperature dependence of the magnetic susceptibility exhibits a maximum at $T \sim 60$ K. The field dependence of magnetisation at low temperature and at relatively low field is in principle linear. These results suggest that the maximum corresponds to the onset of an antiferromagnetic ordering at the Sm sublattice, because it is not sensitive to the composition change, while both the Mn and Ni sublattices seem to be nonmagnetic. Our preliminary investigations of the $NdMn_{12-x}Ni_x$ system seemed to suggest that these materials are nonmagnetic [22]; however, in the light of present results, this conclusion is not quite correct.

For getting a better insight into properties of these interesting alloys, we report at present on high magnetic field measurements of the $(Nd, Sm)Mn_{12-x}(Co, Ni)_x$ systems.

2. Experimental

All the $RMn_{12-x}T_x$ alloys investigated have been prepared as has been described previously [23]. The magnetic susceptibility of $NdMn_{12-x}Ni_x$ has been investigated in the temperature range of 300–750 K, in the magnetic field of 0.5 T, using a SQUID magnetometer. The magnetisation has been measured in a pulsed magnetic field up to 35 T at $T = 4.2$ K, with a pulse duration of 10 ms.

3. Results and discussion

All the samples investigated, stable for R = Nd in the $4 \leq x \leq 6$ range and for R = Sm in the $4 \leq x \leq 8$ range, have been found to be in principle single-phase. Their

unit cell volumes decrease as the concentration of the transition metal x increases (see Fig. 1). Only NdMn$_6$Ni$_6$ is an exception from this trend.
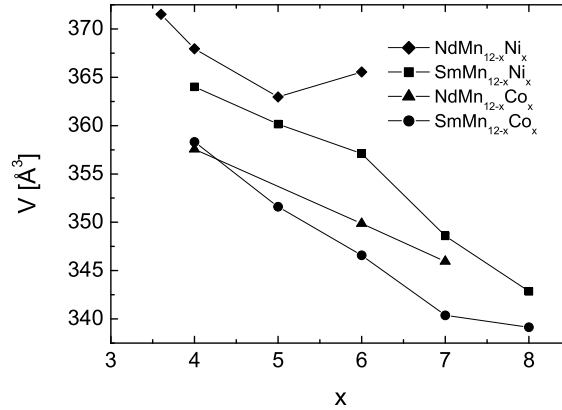

Fig. 1. Unit-cell volume V versus Co [19] and Ni [21, 22]
concentration x for NdMn$_{12-x}$Co$_x$ (triangles), SmMn$_{12}$–Co$_x$ (full circles),
NdMn$_{12-x}$Ni$_x$ (diamonds) and SmMn$_{12-x}$Ni$_x$ (full squares)

Figure 2 shows the results of the high-field measurements of the magnetization M at $T = 4.2$ K for the NdMn$_{12-x}$Co$_x$ alloys. It is seen that the character of the $M(H)$ plots for all the samples is ferromagnetic, however, without a clear saturation, even for the highest magnetic fields. The result for the sample $x = 4$ suggests that the ferromagnetic contribution is field-induced (see Fig. 10 in [19]) and rather weak.
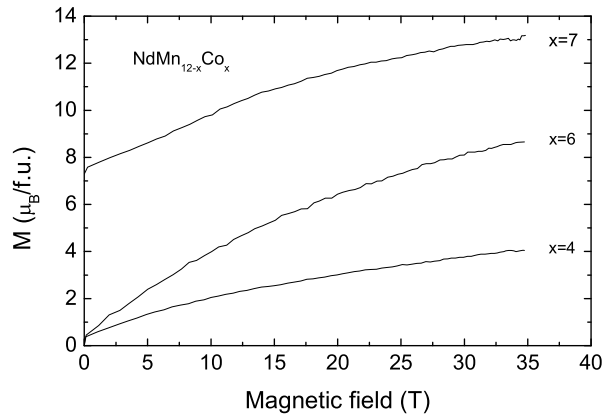

Fig. 2. Magnetization M versus magnetic field
up to 35 T at 4.2 K for NdMn$_{12-x}$Co$_x$

As can be seen from Fig. 3, at $T = 4.2$ K and under high magnetic fields the SmMn$_{12-x}$Co$_x$ compounds have a character slightly different from those of the Nd compounds. The sample $x = 4$ is antiferromagnetic up to the highest field, but the

compound $x = 6$ exhibits some ferromagnetic contribution which is also seen in lower fields [19]. However, the values of magnetization are clearly lower than for the sample $x = 4$. The sample $x = 7$ is apparently strongly ferromagnetic, however, also without a saturation and, in turn, with a lower value of the saturation magnetic moment than the corresponding Nd sample. The lack of saturation may result from a considerable anisotropy which is indicated by a difference in the magnetization of powdered and bulk samples (see [19]).
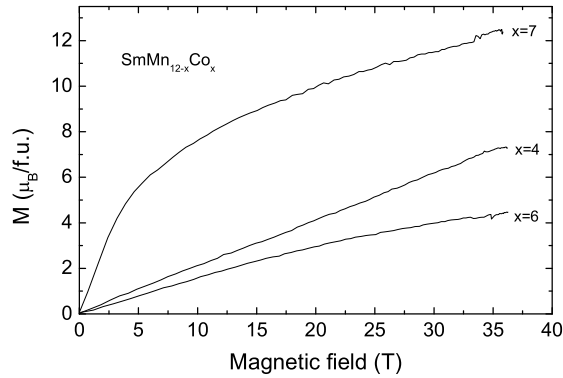

Fig. 3. Magnetization M versus magnetic field
up to 35 T at 4.2 K for $SmMn_{12-x}Co_x$

Our previous results [22] indicate, as mentioned above, that the $NdMn_{12-x}Ni_x$ alloys are most probably paramagnetic below 300 K. To support this hypothesis, at present we extend the susceptibility measurements up to about 750 K. It is seen from Fig. 4 that the compounds with $x = 4$ and $x = 5$ exhibit weakly temperature-dependent paramagnetism, whereas $NdMn_6Ni_6$ shows a maximum of magnetic susceptibility at about 590 K, which can correspond to the Néel point.
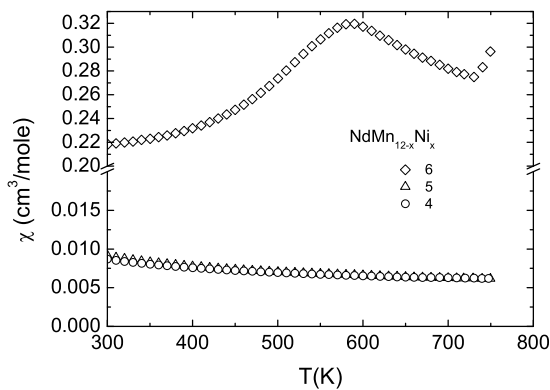

Fig. 4. Magnetic susceptibility χ
versus temperature T from 300 to 750 K for $NdMn_6Ni_6$

Such a high ordering temperature is often observed in other Mn ternaries [24]. The increase of magnetic susceptibility above 720 K most probably follows the thermal decomposition of the material. In Figure 5, the magnetic field dependence of the magnetization is presented at $T = 4.2$ K for the latter material. For the sake of simplicity, only the results obtained for the polycrystalline sample are shown, because the results for the powder sample are very close to those shown in Fig. 5. This behaviour proves that there is a very small anisotropy in this material. It is seen that the $M(H)$ dependence exhibits an apparent approach to saturation which could be an indication of a metamagnetic transition, although it is difficult to determine precisely the critical field. One can estimate it to occur below about 15 T for both polycrystalline and powder samples. Therefore, we believe that magnetic ordering (AF) is responsible for the high-temperature anomaly.
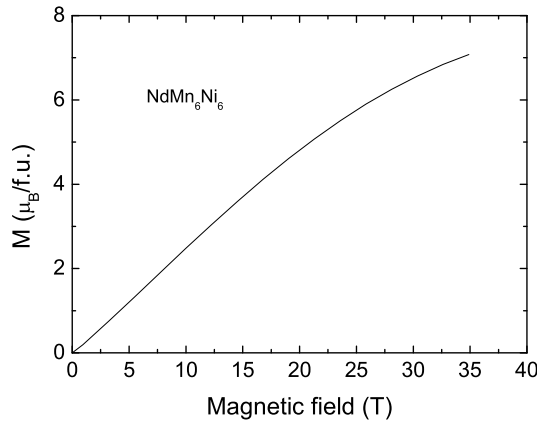

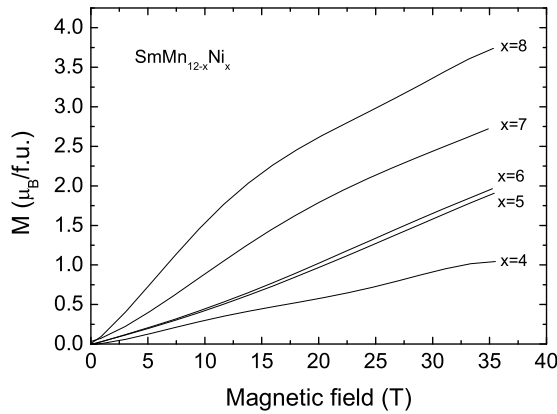Fig. 5. Magnetization M versus magnetic field
up to 35 T at 4.2 K for NdMn$_6$Ni$_6$

Fig. 6. Magnetization M versus magnetic field
up to 35 T at 4.2 K for SmMn$_{12-x}$Ni$_x$

Previously reported linear character of the field dependence of the magnetization up to 5 T [21] for he SmMn$_{12-x}$Ni$_x$ system is in principle preserved in higher fields for the samples with x between 4 and 6 (see Fig. 6). However, for the sample $x = 7$ some tendency to saturation is observed above about 20 T, while for the sample $x = 8$, the same behaviour is seen, but the critical field seems to be lower, whereas the values of magnetization are larger. This observation does not contradict the conclusion of Ref. [21] that the magnetic ordering is due to the Sm sublattice only. For the samples with higher concentration of Ni ($x = 7$ and $x = 8$) magnetic field can induce a magnetic ordering in the transition metal sublattice even of a band metamagnetic type (see e.g., [25]). One should notice that for these two samples in magnetic field below about 10 T a tiny hysteresis is observed (see Figs. 3 and 4 [21]).
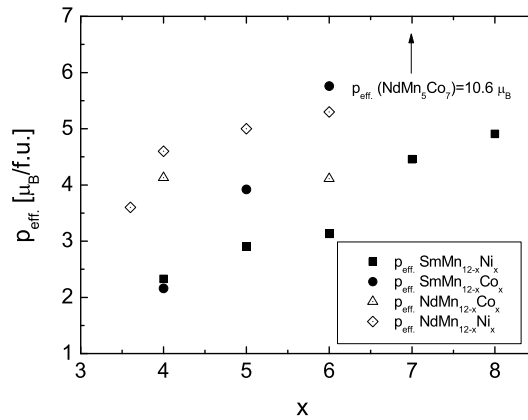

Fig. 7. Effective magnetic moments $p_{eff,}$ versus concentration
of transition element x. Note that effective magnetic moment
for the NdMn$_5$Co$_7$ alloy is out of scale

As was mentioned above, we expected the high-field magnetization measurements performed on powdered samples to provide a basis for the consideration of the contribution of the transition elements to the magnetism. Unfortunately, the saturation moments cannot be determined in a direct way, because hardly any saturation is approached in the compounds investigated, even in rather high magnetic fields. In Fig. 7, the values of the effective magnetic moments p_{eff} are collected. Since a modified Curie–Weiss law is fulfilled in a rather narrow temperature range for all systems investigated, the values provided are rough estimates of the effective magnetic moments. For the comparison, we should recollect the values of the magnetic moment for free ions. For Nd they amount to 3.27 and 3.62μ_B and for Sm to 0.71 and 0.85μ_B for the saturation and effective magnetic moment, respectively. One can see that all experimental values are higher than those of free ions. Therefore, a contribution of the transition metal sublattices is expected. However, at present we are not able to say which transition element has a more substantial effect. These systems are

rather complex and hopefully a neutron diffraction experiment will provide the final explanation of their magnetic properties.

References

[1] SUSKI W., [in:] K.A. Gschneidner, Jr., L.Eyring (Eds.), *Handbook on the Physics and Chemistry of Rare Earths*, Vol. 22, North Holland, Amsterdam, 1996, p. 143 (Chapter 149).

[2] DEPORTES J., GIVORD D., Solid State Commun., 19 (1976), 845.

[3] AMAKO Y., NAGAI H., ADACHI K., J. Phys. Soc. Jpn., 62 (1993), 3355.

[4] KALVIUS G.M., MÜNCH K.-H., KRATZER A., WÄPPLING R., NOAKES D.R., DEPORTES J., BALLOU R., Physica, B289–290 (2000), 69.

[5] DEPORTES J., GIVORD D., LEMAIRE R., NAGAI H., Physica, B86–88 (1977), 69.

[6] OKAMOTO N., NAGAI H., YOSHIE H., TSUJIMARA A., HIKARA T., J. Magn. Magn. Mater., 70 (1987), 299.

[7] AMAKO Y., NAGAI H., NOMURA T., YOSHIE H., OGURO I., SHINOHARA T., ADACHI K., J. Magn. Magn. Mater., 104–107 (1992), 1451.

[8] YANG Y.C., KEBE B., JAMES W.J., DEPORTES J., YELON W., J. Appl. Phys., 52 (1981), 2077.

[9] AMAKO Y., SAOKA S., YOSHIE H., NAGAI H., ADACHI K., J. Phys. Soc. Jpn., 64 (1995), 1860.

[10] MORALES M., ARTIGAS M., BACMANN M., FRUCHART D., SOUBEYROUX J.L., WOLFERS P., J. Alloys Compounds, 262–263 (1997), 1451.

[11] ABAD E., PIQUÈ C., BLANCO J.A., ARTIGAS M., BURRIEL R., FERNANDEZ-DIAZ M.T., J. Magn. Mater., 196–197 (1999), 745.

[12] SUSKI W., WOCHOWSKI K., MYDLARZ T., BELAN B., Acta Phys. Polon., A98 (2000), 505.

[13] SHENG X., WANG Y.-G., LIN P., DU W., TANG N., YANG N., J. Mater. Sci. Lett., 20 (2001), 733.

[14] SUSKI W., WOCHOWSKI K., GILEWSKI A., MYDLARZ T., BELAN B., Physica, B294–295 (2001), 177.

[15] MORALES M., BACMANN M., WOLFERS P., FRUCHART D., OULADDIAF B., Phys. Rev., B64 (2001), 144426.

[16] STANKIEWICZ J., BARTOLOME J., MORALES M., BACMANN M., FRUCHART D., J. Appl. Phys., 90 (2001), 5632.

[17] YANG J.B., YELON W.B., JAMES W.J., CAI S., ECKERT D., HANDSTEIN A., MÜLLER K.-H., YANG Y.C., Phys. Rev., B65 (2002), 064444.

[18] WANG Y.G., YANG F., CHEN C., DU W., LIN P., ZHONG X., WANG Q., phys. stat. sol. (a), 165 (1998), 483.

[19] SUSKI W., WOCHOWSKI K., MYDLARZ T., BELAN B., Physica, B319 (2002), 45.

[20] LIU J.P., DE BOER F.R., DE CHÂTEL P.F., COEHOORN R., BUSCHOW K.H.J., J. Magn. Magn. Mater., 132 (1994), 159.

[21] SUSKI W., WOCHOWSKI K., MYDLARZ T., BELAN B., phys. stat. sol., in press.

[22] SUSKI W., BELAN B., MYDLARZ T., WOCHOWSKI K., J. Alloys Compounds, in press.

[23] BELAN B., SUSKI W., WOCHOWSKI K., [in:] Proc. of the Moscow Intern. Symposium on Magnetism '99, Vol. I, Moscow, 1999, p. 380.

[24] SZYTUŁA A., [in:] K.H.J. Buschow (Ed.), *Handbook of Magnetic Materials*, Vol. 6, Elsevier, Amsterdam, 1991, p. 85 (Chapter 2).

[25] GOTO T., FUKAMICHI K., YAMADA H., Physica, B300 (2001), 167.

High-frequency magnetoimpedance effect in glass-coated amorphous $Co_{83.2} B_{3.3} Si_{5.9} Mn_{7.6}$ microwires

Heebok Lee[1*], Yong-Seok Kim[2], *Seong-Cho Yu[2]

[1]Department of Physics Education, Kongju National University, Kongju 314-701, Korea

[2]Department of Physics Chungbuk National University, Chongju 361-763, Korea

Measurements of the giant magnetoimpedance (GMI) were carried out in the amorphous $Co_{83.2}B_{3.3}$ $Si_{5.9}Mn_{7.6}$ micro-wires at high frequency range from 100 MHz up to 1 GHz of an ac-current flowing along the wire and at varying axial dc-magnetic field in its range of ±120 Oe. The wires, about 15 μm in diameter, were fabricated by a glass-coated melt spinning technique. The shapes of the impedance curves plotted vs. a dc-field change dramatically with the frequency. The phase angle was also strongly dependent on the field. The maximum value of GMI, around 250%, was reached at the frequency of about 500 MHz. The external dc-magnetic field changes the circumferential permeability as well as the penetration depth, both in turn change the impedance of the sample. The increments of GMI at high frequency can be understood in terms of the LC-resonance phenomena. A sudden change of the phase angle, as large as 180°, evidenced the occurrence of the resonance at a given intensity of the external dc-field.

Key words: magnetoimpedance effect; microwires; magnetic sensors

1. Introduction

Giant magnetoimpedance (GMI) effect has been intensively studied because of the increasing prospects of novel applications in magnetic sensors [1]. The phenomenon has a classical electromagnetic origin and is due to a simultaneous occurrence of the skin effect and the changes of the transverse or circumferential permeability under the influence of an external dc-magnetic field applied along a magnetic element [2]. As a consequence, the impedance of a wire, $Z = R + iX$, is altered by the external axial magnetic field (both its components, the resistance R and the reactance X vary with this field). A majority of studies carried out so far have mainly been devoted to investigations of the mechanisms of these complex phenomena at relatively low frequency (radio frequency range) of the ac-current flowing through the sample in the form of a thin ribbon or wires. However, it has been shown that this effect is of very large

----

*Corresponding author, e-mail: heebok@kongju.ac.kr.

magnitude in tiny magnetic wires of a micrometer-diameter. The behaviour of the GMI effect at very high frequencies has not been hitherto studied intensively in spite of their importance from the view-point of both, basic knowledge and technological applications. High-frequency sources are nowadays easily available in communication electronics such as PCs, cellular phones, GPS, etc. It might be expected that the GMI sensors operated at such high frequencies could well be adapted to these electronics, being profitable since at high frequencies the penetration depth is very small.

For a cylindrical magnetic conductor, its impedance can be expressed as

$$Z = R_{dc} ka \frac{J_0(ka)}{2J_1(ka)} \tag{1}$$

where R_{dc} is the dc-resistance of the wire, J_0, and J_1 are the Bessel functions of the first kind, $k = (1 + i)/\delta$, where δ is the penetration depth $\delta = c/(2\pi\omega\sigma\mu_\phi)^{1/2}$, a – the radius of the wire, ω – the angular frequency, σ – the conductivity of the wire, and μ_ϕ – the effective complex magnetic permeability in the circumferential direction [3]. At high frequency range within which $\delta \ll a$, the changes of the impedance are roughly proportional to $Z \propto (\omega\mu_\phi)^{1/2}$ [4, 5]. Therefore, in this frequency range, the total impedance of a magnetic wire is proportional to the square root of the circumferential permeability μ_ϕ.

To achieve large GMI, the penetration depth should be very small in the absence of an external magnetic field. Large circumferential permeability along with a low value of the resistivity gives rise to a small penetration depth at a high frequency range. A large increase of the circumferential permeability can be achieved applying an ac-current of the frequency sufficiently high to excite the resonance of the sample, which constitutes a LC-resonator at this frequency range. This large circumferential permeability strongly decreases the penetration depth and, therefore increases the impedance of the sample.

Since the circumferential permeability equals

$$\mu = 1 + 4\pi\chi(\omega, H)$$

the inductance L of a microwire becomes

$$L = L_0 \left(1 + 4\pi\chi(\omega, H)\right),$$

where

$$\chi = \chi'(\omega, H) - i\chi''(\omega, H)$$

is a complex susceptibility dependent on ω and H. Therefore, the impedance Z of a microwire in the vicinity of the resonance becomes

$$Z = iL_0\omega(1 + 4\pi\chi') + L_0\omega4\pi\chi'' + R_0$$

Recently developed amorphous microwires were found to be more promising for several applications compared to amorphous thicker wires and ribbons because of

their tiny dimensions, superior magnetic properties and a protective glass coating. In this study, we have investigated the high-frequency GMI effect in the glass-coated $Co_{83.2}B_{3.3}Si_{5.9}Mn_{7.6}$ microwires.

2. Experimental

Glass-coated amorphous microwires of nominal composition $Co_{83.2}B_{3.3}Si_{5.9}Mn_{7.6}$ were fabricated using the Taylor–Ulitosky method. The diameter of the metallic core of the sample, measured under an optical microscope, was about 16 μm and the thickness of the insulating glass coating was equal to ~5 μm.

The samples were annealed for 1 hour in vacuum at various temperatures in the range of 150–250 °C in order to settle optimum annealing conditions to achieve the best magnetic softness by reducing residual internal stresses (stress relaxation).

All the measurements of GMI were carried out at a room temperature. A network analyzer (Agilent, 8712ET, 0.3 MHz–1.3 GHz) and an impedance analyzer (HP4191A, 1 MHz–1 GHz), both connected to a computer data acquisition system, were used for these measurements. The power level of the impedance analyzer for the MI measurement was fixed at –20 dBm. A dc-magnetic field, applied in an axial direction, was swept through the entire cycle between –120 Oe and 120 Oe.

The ratio of the magnetoimpedance (MIR), dependent on the external magnetic dc-field, is usually expressed as

$$MIR\,(\%) = \frac{\Delta Z}{Z}(\%) = 100 \times \left[\frac{Z(H) - Z(H_{max})}{Z(H_{max})} \right] \qquad (2)$$

where H_{max} is the maximum intensity of the dc-field applied (in the present experiment H_{max} = 120 Oe). Equation (2) was applied to calculate the magnetoimpedance ratio MIR using the data obtained in the experiment.

3. Results and discussion

It was found that the sample annealed at 180 °C displayed the best magnetic softness, hence this wire-specimen was used in the experiment.

Figure 1 shows the MIR curves calculated using the experimental data obtained at different frequencies and plotted as a function of the external axial dc-field. As is seen in the figure, the maximum value of MIR increases drastically with an increase of the frequency up to 550 MHz. This is mainly due to a decrease of the penetration depth, whose value is estimated smaller than 1 μm at the frequencies used in the experiment.

The dominating contribution to the effective permeability comes either from the rotation of magnetization or from the domain wall motion [6]. In general, depending on the frequency, three main mechanisms of the GMI-effect can be distinguished, namely: (i) at relatively low frequencies the changes of the impedance are entirely

ascribed to the magnetoinductive effect arising from the circular magnetization proc-
esses, (ii) at high frequencies, the skin effect becomes dominant because of the large
permeability, and (iii) at very high frequencies, a motion of domain walls is totally
damped and the permeability rapidly decreases until the resonance phenomena are
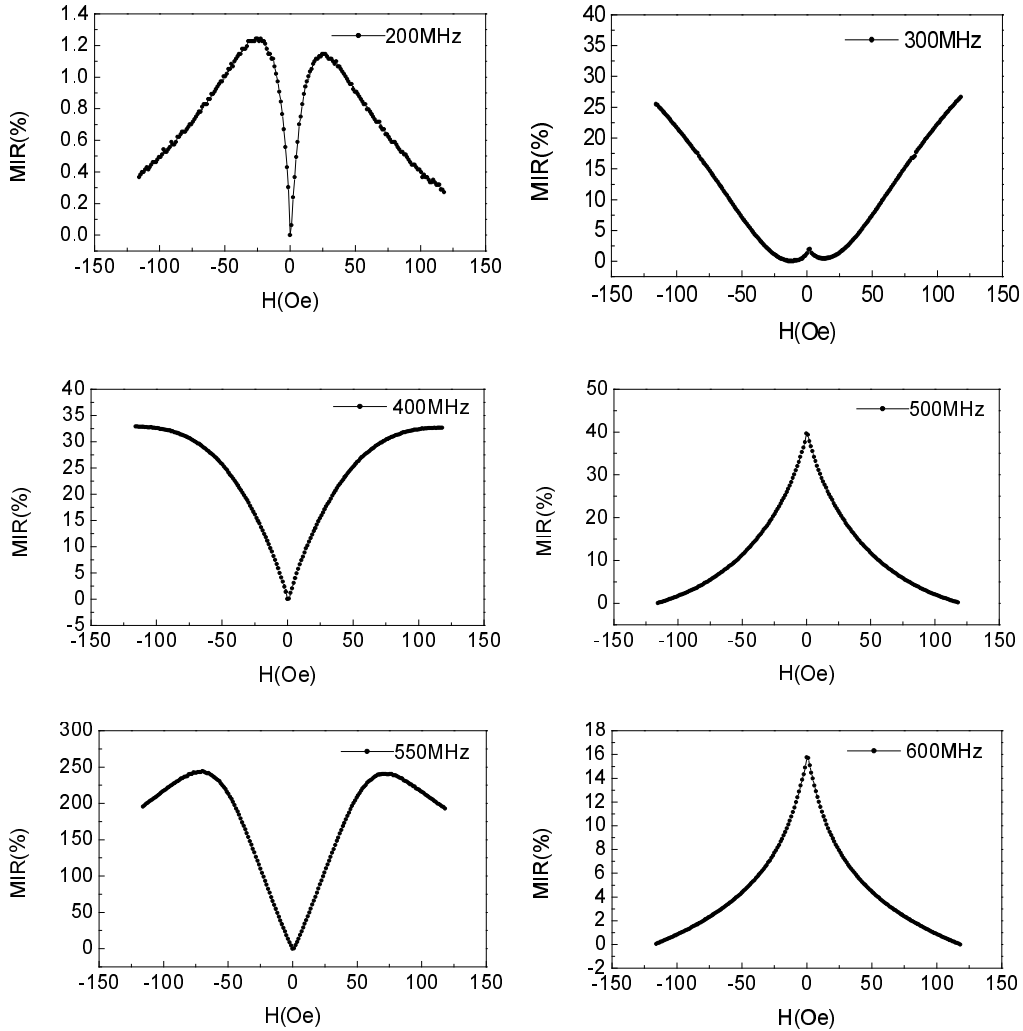reached [7].

Fig. 1. MIR curves measured at various frequencies (200, 300, 400, 500, 550, 600 MHz)

Because the frequencies of the ac-current flowing along the wire-sample are very high,
the obtained experimental dependencies of GMI can be interpreted in accordance with the
case (iii), where the domain walls are immovable. Therefore, the MIR curve obtained at
200 MHz can be understood considering the above case. At the frequencies above

200 MHz, a dramatic increase of the MIR value is observed, due to the occurrence of the resonance. At very high frequency range, the sample behaves like a RLC-electric circuit, where R is its resistance, L – the inductance and C – capacitance. Therefore, the resonance frequency of the sample can be given by the well-known expression

$$\omega_r(\omega, H) = \frac{1}{\sqrt{L(\omega, H)C}} \tag{3}$$

where ω is the angular frequency of the ac-current flowing along the wire-sample.

Since the inductance $L(\omega, H)$ depends on the external dc-field as well as on the frequency, the resonance frequency of the sample depends also on these quantities. This is reflected by the complex shapes of the MIR-curves shown in Fig. 1.

In order to simulate the GMI behaviour based on the concept of a LC-resonator, it can roughly be assumed that the inductance L does not depend on the frequency in its range used in the experiment. It can be expressed as

$$L(H) = L_0\left(1 - \alpha H^{0.5}\right)$$

where L_0 is the inductance at $H = 0$, and α is a constant. The inductance simulated in such a way is shown in Fig. 2 as a function of the dc-field.

The impedance and the phase angle can be given by

$$Z(\omega, H) = \sqrt{R^2 + \left(\omega L(H) - \frac{1}{\omega C}\right)^2} \tag{4a}$$

$$\theta(\omega, H) = \tan^{-1}\left(\frac{\omega R}{\frac{1}{C} - L(H)\omega^2}\right) \tag{4b}$$

The impedancies $Z(\omega, H)$ calculated according to Eq. (4a) and plotted as a function of frequency at various intensities of the external dc-field are shown in Fig. 3, where C is taken as 1000 pF estimated from cylindrical condensers of electric terminals at the ends of a microwire. As can be expected, the impedance at frequencies higher than the resonance frequency, $\omega \gg \omega_r$, decreases with an increase of the external magnetic dc-field. In the frequency range lower than that of the resonance, $\omega \ll \omega_r$, an opposite effect is observed, the magnetoimpedance increases with the increase of the external magnetic dc-field.

The calculated impedance curves plotted as a function of the dc-field at different 3 frequencies are shown in Fig. 4. As can easily be noticed, the shapes of these simulated magnetoimpedance curves are much the same as the shapes of those obtained experimentally (see Fig. 1). Similarly, the calculated field dependence of the phase angle (Eq. (4b)), shown in Fig. 5, resembles the experimental one obtained at

550 MHz (close to the resonance frequency). The sudden change of the phase angle as large as 180° gives evidence that the resonance in fact occurs at a specific intensity of the dc-field.
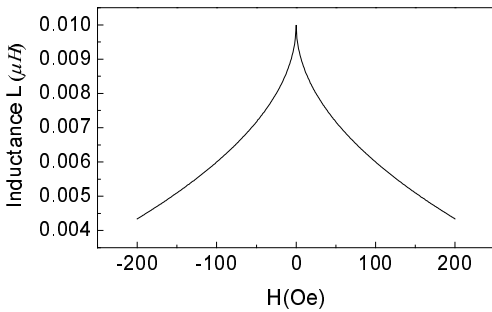

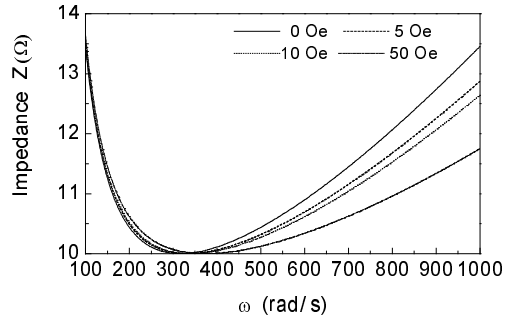Fig. 2. Calculated inductance *L* as a function of the external field *H*

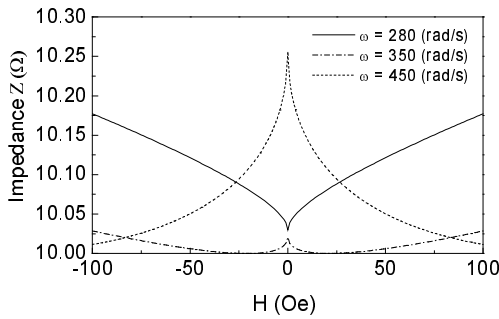Fig. 3. Calculated impedances *Z* as a function of frequency ω at various external fields, $H = 0, 5, 10, 50$ Oe

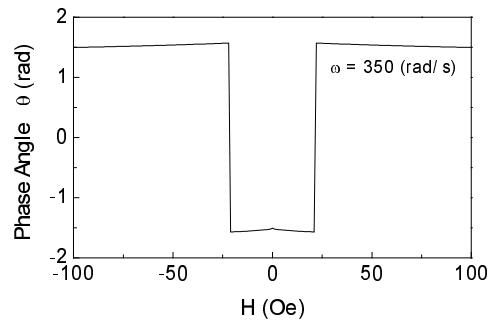Fig. 4. Calculated impedances *Z* at different frequencies, $\omega = 450, 350, 280$ (rad/s)

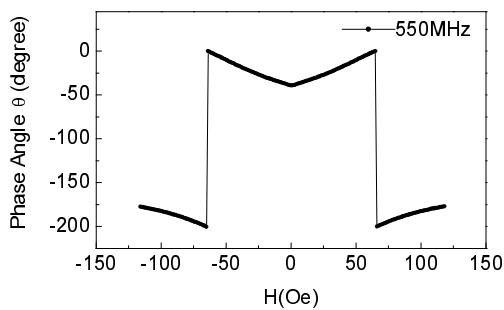Fig. 5. Calculated phase-angle θ curve at a resonance frequency ω of 350 (rad/s)

Fig. 6. Phase-angle curve measured at 550 MHz

However, a drastic increase of the ac-current takes place at the resonance frequency. This effect was not taken into account in the performed calculation of the impedance. The large current generates a large circumferential magnetic ac-field in the wire-sample resulting in an increment of the circumferential permeability μ_ϕ. Therefore, a drastic rise of the

magnetoimpedance in the vicinity of the resonance frequency can be expected. This is clearly visible in the MIR curve measured at 550 MHz (see Fig. 1).

4. Conclusions

In this study, the giant magnetoimpedance (GMI) effect was investigated in amorphous $Co_{83.2}B_{3.3}Si_{5.9}Mn_{7.6}$ microwire in a very high frequency range up to 1 GHz. The shapes of the dc-field dependencies of the impedance changed dramatically with an increase of the frequency of the ac-current flowing along the sample. The observed increments of the maximum of the magnetoimpedance ratio (MIR) with an increase of the frequency can be interpreted in terms of the LC-resonance phenomena. The maximum value of MIR reached in the experiment equals 250% at the frequency of around 550 MHz. The sudden change of the phase angle, as large as 180°, proved the occurrence of the resonance at the specified intensity of the external dc-field.

References

[1] KIM Y.K., CHO W.S., KIM T.K., KIM C.O., LEE HEEBOK, J. Appl. Phys., 83 (1998), 6575.
[2] PANINA L.V., KATOH H., MOHRI K., KAWASHIMA K., IEEE Trans. Magn., 29 (1993), 2524.
[3] PANINA L.V., MOHRI K., BUSHIDA K., NODA M., J. Appl. Phys., 76 (1994), 6198.
[4] CIUREANU P., BRITEL M., MENARD D., YELON A., AKYEL C., ROUABHI M., COCHRANE R.W., RUDKOWSKI P., STRÖM-OLSEN J.O., J. Appl. Phys., 83 (1998), 6563.
[5] MACHADO F.L.A., DE ARAUJO A., PUCA A., RODRIGUES A.R., REZENDE S.M., Phys. Stat. Solidi (a), 173 (1999), 135.
[6] ATKINSON D., SQUIRE P.T., J. Appl. Phys., 83 (1998), 6569.
[7] VAZQUEZ M., J. Magn. Magn. Mater., 226–230 (2001), 693.

The effect of axial dc-field on transverse permeability in Co-based metallic glass ribbons

HENRYK K. LACHOWICZ[1*], MAREK KUŹMIŃSKI[1], SEONG-CHO YU[2]

[1]Institute of Physics, Polish Academy of Sciences, al. Lotników 32/46, 02-668 Warszawa, Poland

[2]Department of Physics, Chungbuk National University, Chongju 361-763, Korea

A simple geometrical model is proposed. This model allows calculating the penetration depth and the mean transverse permeability in magnetic elements of a rectangular cross-section which are used to study the giant magnetoimpedance effect (GMI). As an example, both the quantities mentioned were calculated for the Co-based metallic glass ribbon using the experimental data. Their evolution with the axial dc-field applied at various frequencies of the ac-current, flowing along the ribbon, is presented. A comparison of the experimental data with those calculated from the model shows that the latter gives only a qualitative approximation of the dependencies measured.

Key words: *giant magnetoimpedance; skin effect; penetration depth; transverse permeability; metallic glass*

1. Introduction

The occurrence of the giant magnetoimpedance (GMI) effect was reported in 1994 [1–3]. This effect manifests itself as huge changes in the impedance of a magnetic element usually in the form of magnetically soft thin ribbon, tiny wire or occasionally thin film submitted to a simultaneous action of an external longitudinal dc-magnetic field and a transverse or circular (in the case of wires) ac-field generated by an ac-current of the r.f.-frequency flowing through the element. The physical background of the GMI-phenomenon is now well recognized (see e.g. [4]). Moreover, this effect is expected to be utilized in a numerous sensitive sensors of various physical quantities (see e.g. [5]). In a range of a relatively high frequency of the ac-current (~ 0.1–100 MHz), the main source of GMI is a well-known classical skin effect. The latter manifests itself in such a way that the applied current effectively flows in an outer part of the cross-section of the magnetic element.

_____

[*]Corresponding author, e-mail: lacho@ifpan.edu.pl.

The penetration depth δ, which gives a measure of this effect, is described by the commonly known expression

$$\delta = \left(\frac{2\rho}{\omega \mu_0 \mu} \right)^{1/2} \tag{1}$$

where ρ is the electrical resistivity of a magnetic element, ω – the angular frequency of a driving current ($\omega = 2\pi f$; f – frequency), μ_0 – permeablity of free space equal to $4\pi \cdot 10^{-7}$ H/m, and μ – the relative transverse (or circular) permeability.

Since the transverse permeability can vary by orders of magnitudes with a dc-external magnetic field applied along the length of the magnetic element, the penetration depth also strongly varies, resulting in huge changes of the impedance. Considering the above, it is obvious that the transverse permeability (or circular one in the case of wires) is the key parameter which governs the GMI-effect in the range of high enough r.f.-frequencies.

A direct measurement of the transverse permeability is not an easy task and requires some special measuring arrangement (see e.g. [6]). However, this permeability and its dc-field dependence can be estimated using a very simple, geometrical model. Such a model for magnetic wires has been proposed by Knobel et al. [7].

In the present paper, a similar approximation is presented but for samples in the form of a ribbon. The results calculated using this approximation are compared with the experimental data obtained for Co-based metallic glass ribbon samples.

2. Simple theoretical model

A simple model is formulated under a rough assumption that changes in the real component (in-phase one) of the impedance are only due to changes in the effective cross-section within which the current flows as a consequence of the skin effect. Under this condition, it can be assumed that the current flows in an outer area of the cross-section of the ribbon S which is given by

$$S = 2b\delta + 2(a - 2\delta)\delta \tag{2}$$

where a and b are the thickness and width of the ribbon, respectively (assuming that the cross-section of the ribbon has a rectangular shape, the condition which in reality is not exactly fulfilled), and δ is the penetration depth as before.

Considering Eq. (2), the penetration depth can now be expressed in terms of the ratio $R_0/R_{ac}(H)$, where R_0 is the dc-resistance of the sample, and $R_{ac}(H)$ – the real (in-phase) component of the impedance at a given frequency of the current and external dc-field. Applying the usual definition of resistance, $R = \rho l/S$, the penetration depth as a function of the external dc-field is then given by

$$\delta(H) = \frac{1}{4}(a+b)\left\{1 - \left[1 - 4\frac{ab}{(a+b)^2} \cdot \frac{R_0}{R_{ac}(H)}\right]^{1/2}\right\} \qquad (3)$$

Using the values of $\delta(H)$, calculated from Eq. (3) for the experimental data of $R_{ac}(H)$, it is possible to estimate the mean values of the relative transverse permeability μ, making use of Eq. (1). Hence

$$\mu(H) = \frac{2\rho}{\mu_0 \omega [\delta(H)]^2} \qquad (4)$$

3. Experimental details

The experiments were performed on the metallic glass ribbon samples annealed at 350 °C for 80 min (stress relaxation) and at 350 °C for 1 h under tensile stress of 410 MPa in order to induce transverse anisotropy (marked for short as A- and B-samples, respectively). The ribbon, 25 μm thick and 2.2 mm wide, of the nominal composition $Co_{67}Fe_4Mo_{1.5}Si_{16.5}B_{11}$ (VITROVAC 6025) was used considering its extremely high magnetic softness [8]. The quasi-static magnetization characteristics of the samples were measured using a computer-controlled hysteresis loop tracer. The real and imaginary components of the impedance of the samples were measured between the voltage pick-up contacts placed 19 mm away in the sample holder, using an Agilent 4285A Precision LCR Meter equipped with the coaxial leads (4-pair method). These measurements were carried out at the frequencies of 0.1, 1, 10 and 30 MHz of a sinusoidal ac-current of 10 mA, flowing along the sample axis. In order to generate the GMI-effect, a longitudinal dc-magnetic field up to ~ 12 kA/m was applied by a Helmholtz pair.

4. Results and discussion

The magnetization characteristics for the samples studied, measured along their axis, are shown in Fig. 1. The observed tilt of the characteristic obtained for the A-sample resulted mainly from the demagnetization effect in the sample 40 mm long used in these measurements. The characteristic obtained for the B-sample displays typical hard-axis magnetization dependence. In Fig. 2a, b, the experimental field dependencies of the real $R_{ac}(H)$ and imaginary $X(H)$ components of the sample impedance, obtained for the A-sample at 0.1, 1, 10 and 30 MHz, are shown. Similar dependencies obtained for the B-sample at 10 MHz are shown in Fig. 3. These characteristics exhibit typical shapes, similar to those reported in the literature. However, it is worth noting that the curves presenting the field dependencies of the real compo-

nent (Fig. 2a) tend asymptotically with an increase of the dc-field to the measured value of a dc-resistance of the sample, $R_0 = 0.37$ ω. This gives an evidence for the reliability of the measurements performed.
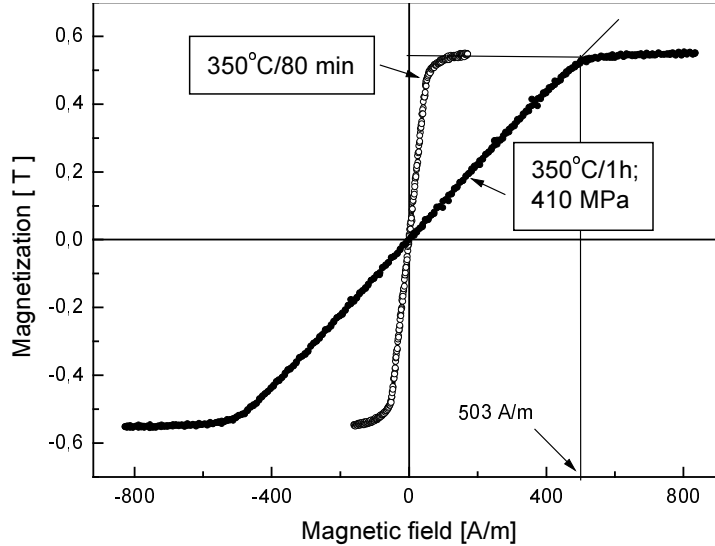

Fig. 1. Magnetization characteristics of Co-based metallic glass samples used in experiments

The dependencies of the penetration depth vs. the dc-field, calculated using Eq. (3), the value of R_0 given above and the experimental data of $R_{ac}(H)$, obtained for the A-sample at different frequencies of the ac-current, are shown in Fig. 4. In Fig. 5, the field dependencies of the mean relative transverse permeability, calculated for the same sample by Eq. (4), are presented. As expected, the skin effect became stronger with an increase of the frequency. As can also be expected, a maximum of this effect (the smallest penetration depth) occurs in the range of the dc-field within which the transverse permeability was the largest. With an increase of the dc-field, the penetration depth decreases monotonically tending asymptotically towards a value of a half of the sample thickness (no skin effect).

The absolute value of the imaginary component of the impedance (reactance) equals $X = \omega L$, where L is the inductance of the magnetic element (neglecting the capacitive term of the reactance which usually is very small). If the penetration depth is much smaller than the sample thickness ($\delta/a < 0.15$), the inductance of the sample can well be approximated by an equation which shows that this quantity is directly proportional to the product of this depth and the transverse permeability [9]. Considering this, a comparison of the measured imaginary component with the calculated product mentioned above should show to what extent the introduced model approximates the experimental data. Such a comparison obtained for the A-sample at 10 MHz is presented in Fig. 6 (both quantities shown are normalized in relation to their maximum

values). As is seen in this figure, the calculated curve considerably departs from that obtained experimentally. The penetration depth is the smallest in the range of low dc-field (see Fig. 4), therefore it can be expected that the approximation should be more satisfactory in this range of field. Figure 7 shows both curves plotted within a small range of the dc-field, around its zero value (double lines in these dependencies reflect the hysteresis effect). As is seen in these figures, only a qualitative approximation of the experimental field dependencies of the reactance is observed.
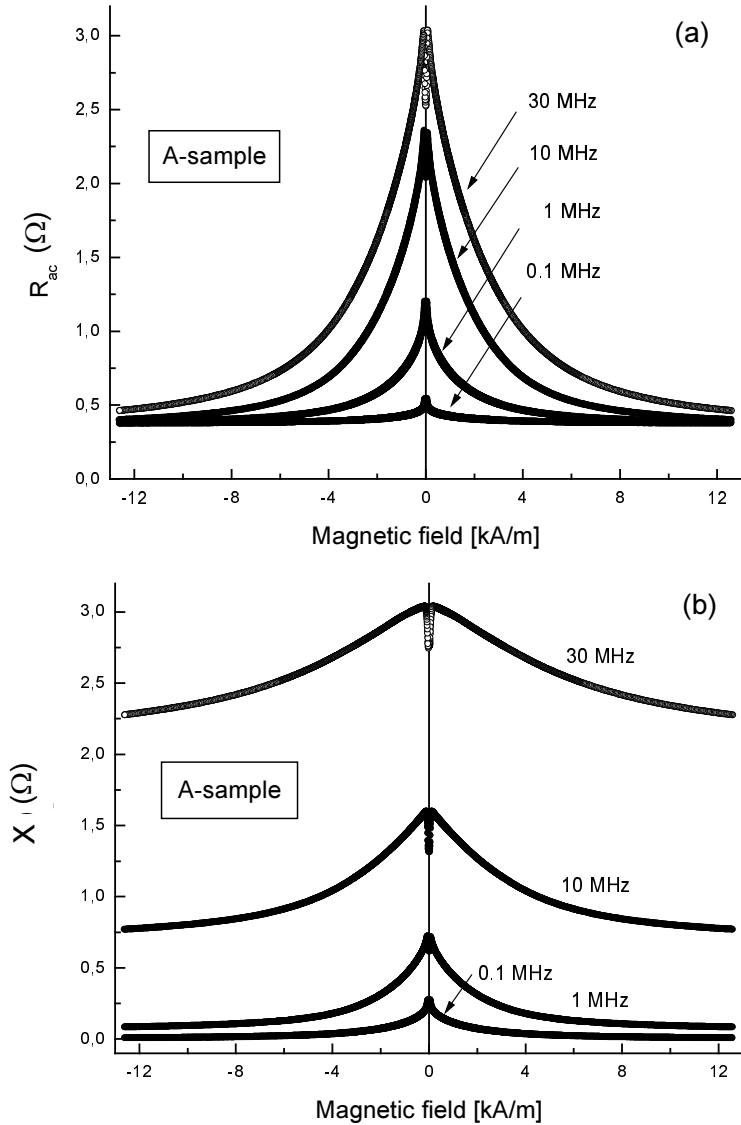
Fig. 2. Real (a) and imaginary (b) components of impedance vs. dc-field measured for A-sample at various frequencies of ac-current
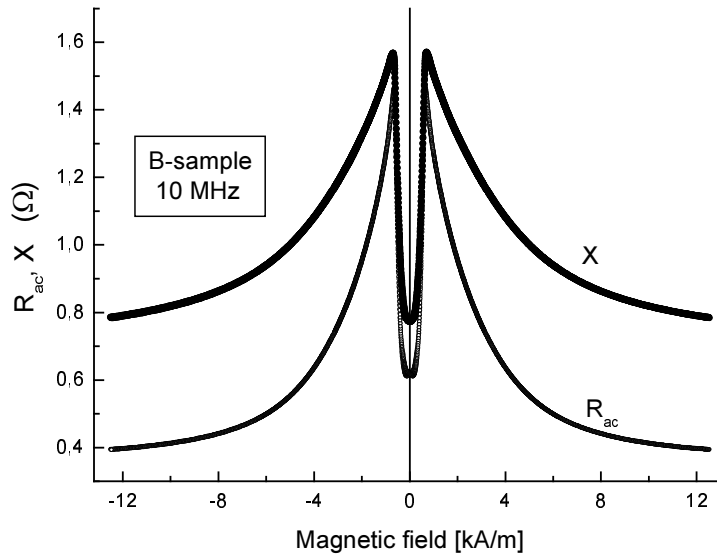
Fig. 3. Real (R_{ac}) and imaginary (X) components of impedance
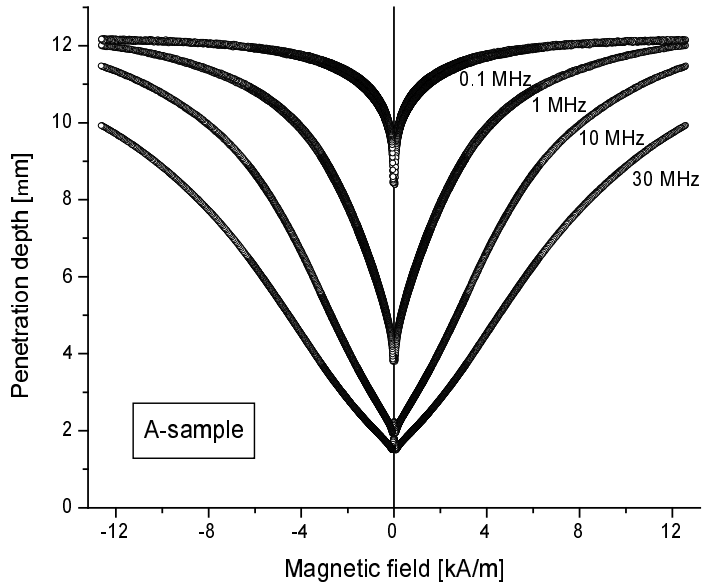vs. dc-field measured for B-sample at 10 MHz

Fig. 4. dc-field dependencies of penetration depth
calculated for A-sample at various frequencies

Figure 8 presents the field dependencies of the penetration depth and transverse permeability obtained for the B-sample, whereas Fig. 9 shows similar curves as those in Fig. 7 but for the B-sample. Since at dc-fields lower than the anisotropy field of the

sample, its magnetization proceeded mainly by rotation of spins, one can speculate that the better approximation visible in Fig. 9 occurs for rotational processes rather than for a domain wall motion. Further studies are in progress to confirm whether the above supposition is correct.
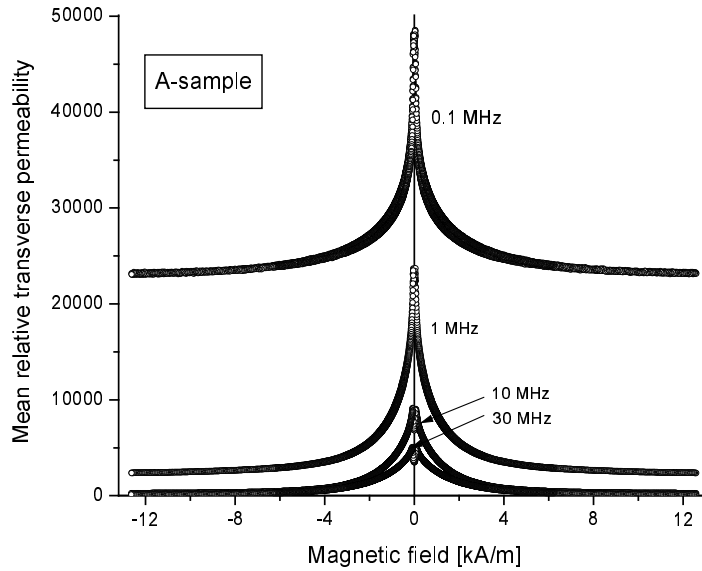

Fig. 5. dc-field dependencies of mean relative transverse permeability
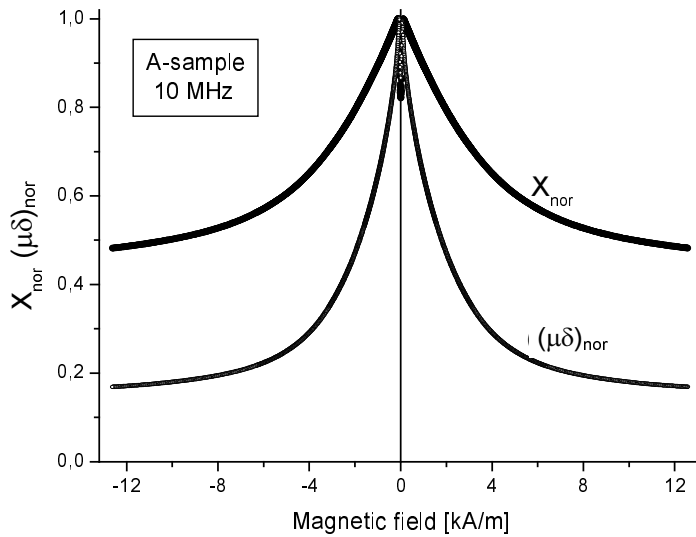calculated for A-sample at various frequencies

Fig. 6. Measured imaginary component of impedance (X_{nor}) and calculated product
of penetration depth and transverse permeability ($\mu\delta$) vs. dc-field obtained for A-sample
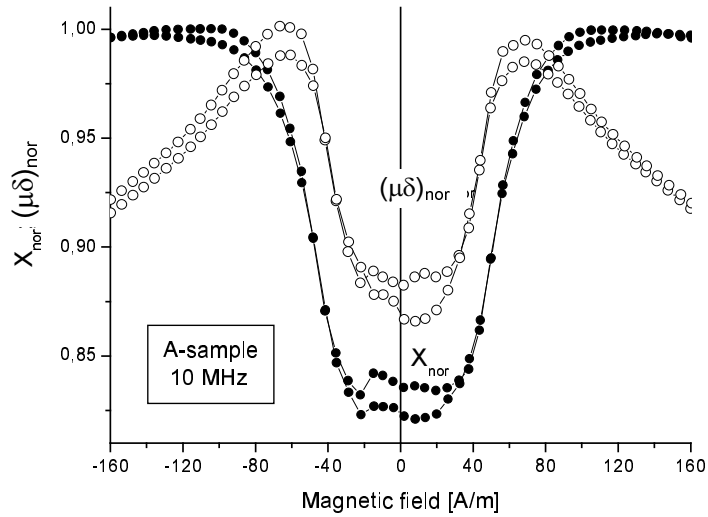at 10 MHz (both curves normalized in relation to their maximum values)

Fig. 7. Measured imaginary component of impedance (X_{nor})
and calculated product ($\mu\delta$) for A-sample (normalized in this same way as in Fig. 6)
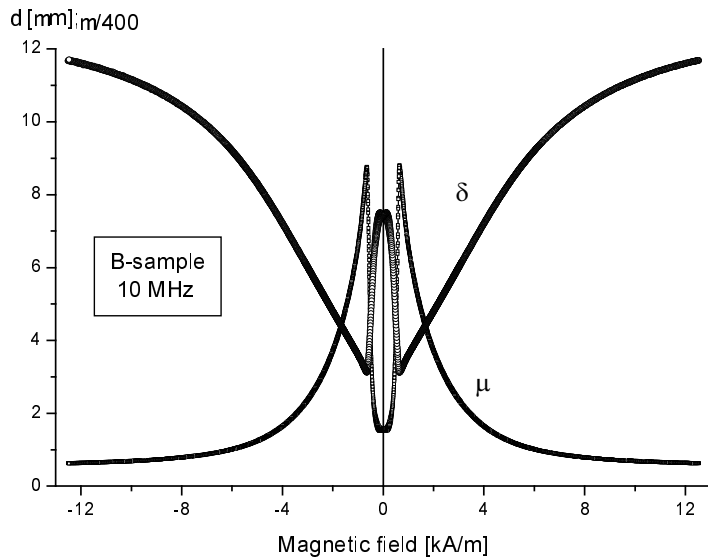shown in narrow range of dc-field around its zero value at the frequency of 10 MHz

Fig. 8. Dependencies of penetration depth (δ) and mean relative transverse
permeability (μ) calculated for B-sample at 10 MHz

The fact that the performed approximation is far from being satisfactory is, how-
ever, not surprising since the measured values of the reactance comprise the self-
inductance of the sample which consists of two components, intrinsic and external
ones, the latter are being neglected in the calculations. Additionally, the condition
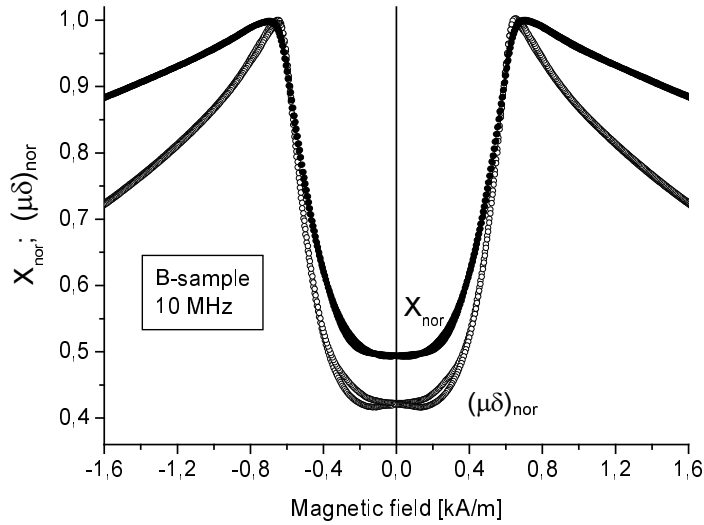
Fig. 9. Measured imaginary component of impedance and calculated product
for B-sample at 10 MHz, shown in narrow range of dc-field

$\delta/a < 0.15$ is not fulfilled even at the highest frequency used in the experiments. Furthermore, the model was introduced neglecting a number of effects which most probably occur in a magnetic element, but which would hardly be taken into account. The current distribution within the ribbon sample is, in reality, much more complex than that assumed in the model. Additionally, the transverse permeability could not be homogeneous because of magnetic heterogeneity usually existing in the real magnets. Also the thickness of the ribbon can display fractional variations. Further, the micro-eddy currents, generated by the moving domain walls, should also be considered [10]. However, the advantage of this model is that the shapes of both the self-consistent basic quantities governing the GMI-effect, the penetration depth and the transverse permeability can effortlessly be estimated giving an instructive outlook on their variation with the external dc-field.

5. Conclusions

A simple model is proposed which allows us to calculate the penetration depth, the parameter giving a measure of the skin effect which is mainly responsible for the GMI phenomenon observed at high enough frequencies of the ac-current flowing through magnetic element. The model also makes it possible to calculate the mean transverse permeability as a function of the external magnetic dc-field. A comparison of the experimental dependencies with those calculated from the model showed that only a qualitative agreement can be achieved. However, the model allows us to estimate the basic quantities governing the GMI-effect, which are difficult to be obtained oth-

erwise. Such estimation can be performed not only for ribbon samples but also for magnetic elements, the cross-section of which is rectangular, e.g., magnetic films.

References

[1] BEACH R.S., BERKOWITZ A.E., Appl. Phys. Lett., 64 (1994), 3652; also J. Appl. Phys., 76 (1994), 6209.

[2] PANINA L.V., MOHRI K., Appl. Phys. Lett., 65 (1994), 1189.

[3] MACHADO F.L.A., DA SILVA B.L., REZENDE S.M., MARTINS C.S., J. Appl. Phys., 75 (1994), 6563.

[4] KNOBEL M., J. Phys. IV France, 8 (1998), Pr2-213.

[5] VÁZQUEZ M., KNOBEL M., SÁNCHES M.L., VALENZUELA R., ZHUKOV A., Sensors and Actuators A, 59 (1997), 20; see also MOHRI K., UCHIYAMA T., PANINA L.V., Ibid, p.1, and VÁZQUEZ M., Physica B, 299 (2001), 302.,

[6] HERNANDO A., VÁZQUEZ M., J. Phys.D: Appl.Phys., 11 (1078), 1539.

[7] KNOBEL M., SÁNCHES M.L., GÓMEZ-POLO C., MARÍN P., VÁZQUEZ M., HERNANDO A., J. Appl. Phys., 79 (1996), 1646.

[8] Vacuumschmelze Catalogue.

[9] *Encyclopedia of Physics* (in Polish), Vol. 1, PWN, Warszawa, 1972, p. 805.

[10] PANINA L.V., MOHRI K., J. Appl. Phys., 79 (1996), 1646.

Large magnetocaloric effect in perovskite manganites: changes of the magnetic entropy above 300 K

Manh-Huong Phan[1], Seong-Cho Yu[1*], A.N. Ulyanov[1, 2], H.K. Lachowicz[3]

[1]Department of Physics, Chungbuk National University, Cheongju 361-763, Korea

[2]Donetsk Physico-Technical Institute of National Academy of Sciences, 83114 Donetsk, Ukraine

[3]Institute of Physics, Polish Academy of Science, al. Lotników 32/46, 02-668 Warszawa, Poland

We present results of the investigation of the large magnetic entropy change, ΔS_M, above 300 K, in a series of $La_{0.65}Sr_{0.35}MnO_3$, $La_{0.6}Sr_{0.2}Ca_{0.2}MnO_3$, $La_{0.6}Sr_{0.2}Ba_{0.2}MnO_3$, $La_{0.7}Ba_{0.3}MnO_3$ and $La_{0.7}Ba_{0.24}Ca_{0.06}MnO_3$ perovskite manganites. Of the compositions studied, $La_{0.6}Sr_{0.2}Ba_{0.2}MnO_3$ exhibits the highest value of ΔS_M^{max} equal to 2.26 J/(kg·K) at the Curie temperature $T_C = 354$ K when the magnetic field is changed from 0 to 10 kOe. The adiabatic temperature change ΔT_{ad} of this sample is ~1.1 K and ~4.95 K in the fields of 10 kOe and 50 kOe, respectively. Due to a strong magnetocaloric effect produced in those materials above the Curie temperature of 300 K, they seem to be attractive for the above room-temperature magnetic-refrigeration applications.

Key words: *entropy; magnetocaloric effect; magnetic refrigeration; perovskite; double exchange*

1. Introduction

A magnetocaloric effect (MCE), consisting in the change of magnetic entropy closely related to the change of temperature of a magnetic material when it passes through a magnetization–demagnetization process, was primarily discovered by Warburg [1]. The MCE, being intrinsic to all magnetic materials, results from the coupling of the magnetic sublattice with the magnetic field, which changes the magnetic part of the entropy of solid [2, 3]. There are two crucial requirements for a magnetic material to possess a large MCE. One is a large enough spontaneous magnetization (such as in the case of a heavy rare-earth metal, Gd, for example) and the other is a sharp drop in magnetization with increasing temperature, associated with ferromagnetic–paramagnetic transitions at the Curie temperature (as was found in perovskite manganites).

---

*Corresponding author, e-mail: scyu@chungbuk.ac.kr.

In recent years, Pecharsky and Gschneidner [4] discovered a giant magnetic entropy change associated with a first-order phase transition in $Gd_5Si_2Ge_2$ alloy. This compound exhibits the MCE about twice as large as that exhibited by gadolinium, the best known magnetic refrigerant material for near room temperature applications. However, efforts to search a proper material that exhibits a large magnetic entropy change in a wide temperature region required for application are still extremely promoted. Thereby, recently rare-earth perovskite manganites of the general formula $La_{1-x}M_xMnO_3$ (M = Ca, Sr, Ba, etc.) having a substantial magnetic-entropy change associated with the ferromagnetic–paramagnetic transition at the Curie temperature have generated considerable interest of many scientists because of a practical aspect of the research [5–11].

In the present work, we report on the magnetocaloric effect in perovskite manganites such as $La_{0.65}Sr_{0.35}MnO_3$, $La_{0.6}Sr_{0.2}Ca_{0.2}MnO_3$, $La_{0.6}Sr_{0.2}Ba_{0.2}MnO_3$, $La_{0.7}Ba_{0.3}MnO_3$ and $La_{0.7}Ba_{0.24}Ca_{0.06}MnO_3$. A considerable magnetic entropy change associated with ferromagnetic–paramagnetic transition is interpreted in terms of the Zener double-exchange model.

2. Experimental details

$La_{0.65}Sr_{0.35}MnO_3$ (LSMO), $La_{0.6}Sr_{0.2}Ca_{0.2}MnO_3$ (LSCMO), $La_{0.6}Sr_{0.2}Ba_{0.2}MnO_3$ (LSBMO), $La_{0.7}Ba_{0.3}MnO_3$ (LBMO) and $La_{0.7}Ba_{0.24}Ca_{0.06}MnO_3$ (LBCMO) samples were prepared by the conventional solid-state reaction technique from a stoichiometric mixture of La_2O_3, $SrCO_3$, $CaCO_3$, $BaCO_3$ and MnO_2 at a pre-sintering temperature of 1250 °C for 16 hrs. They were sintered at 1350 °C for 18 h after regrinding and pressing into pellets. X-ray diffraction confirmed the single-phase rhombohedral perovskite structure in all the samples. The magnetic measurements were carried out with a vibrating sample magnetometer (VSM) in the fields up to 10 kOe.

In terms of the thermodynamic theory, the entropy change caused by the variation of the magnetic field from 0 to H_{max} is given by

$$\Delta S_M \quad = \quad \int_0^{H_{max}} \left(\frac{\partial S}{\partial H} \right)_T dH \tag{1}$$

On the other hand, by using Maxwell's thermodynamic relationship

$$\left(\frac{\partial M}{\partial T} \right)_H = \left(\frac{\partial S}{\partial H} \right)_T \tag{2}$$

Equation (1) can be re-written in the following form:

$$\Delta S_M \quad = \quad \int_0^{H_{max}} \left(\frac{\partial M}{\partial T} \right)_H dH \tag{3}$$

Furthermore, according to [7] we have for an isobaric process at constant H

$$\left(\frac{\partial S}{\partial T}\right)_H = \frac{C_{P,H}}{T} \tag{4}$$

where $C_{P,H}$ is the heat capacity at a constant pressure and constant magnetic field. Considering a reversible adiabatic process ($dS_M = 0$) and combining Eqs. (2) and (4), we arrive at

$$dT = -\frac{T}{C_{P,H}}\left(\frac{\partial M}{\partial T}\right)_H dH \tag{5}$$

The adiabatic temperature change can now be obtained by integrating Eq. (5) over the magnetic field

$$\Delta T_{ad} = -\int_{H_1}^{H_F} \frac{T}{C_{P,H}}\left(\frac{\partial M}{\partial T}\right)_H dH \tag{6}$$

where H_1 is the initial magnetic field and H_F is the final magnetic field.

For simplification, numerical evaluation of the change of magnetic entropy was carried out based on Eq. (3), which is estimated from the isothermal magnetization measurements. In the case of magnetization measurements at small discrete field and temperature intervals, ΔS_M can be approximated using Eq. (3) by

$$\left|\Delta S_M\right| = \sum_i \frac{M_i - M_{i+1}}{T_{i+1} - T_i} \Delta H_i \tag{7}$$

where M_i and M_{i+1} are the magnetization magnitudes measured in the field H at the temperature T_i and T_{i+1}, respectively. Thereby, the changes of magnetic entropy associated with the variations of the field applied can be calculated from Eq. (7).

3. Results and discussion

Figure 1 shows the temperature dependencies of magnetization for two selected samples (LSBMO and LSCMO), for which the Curie temperatures were 354 K and 337 K, respectively. The Curie temperature T_C, defined as the temperature at which the curve $\partial M/\partial T$–T reaches a minimum, has been determined from the M–T curves. The values of T_C of all the samples studied are summarized in the table. In Figure 2, the dependencies of magnetization of LSBMO on magnetic field are presented as a representative example. They show a substantial variation of magnetization around the Curie temperature. As will be discussed later in detail, a considerable magnetic entropy variation associated with the ferromagnetic–paramagnetic transition temperature (T_C) can be observed.
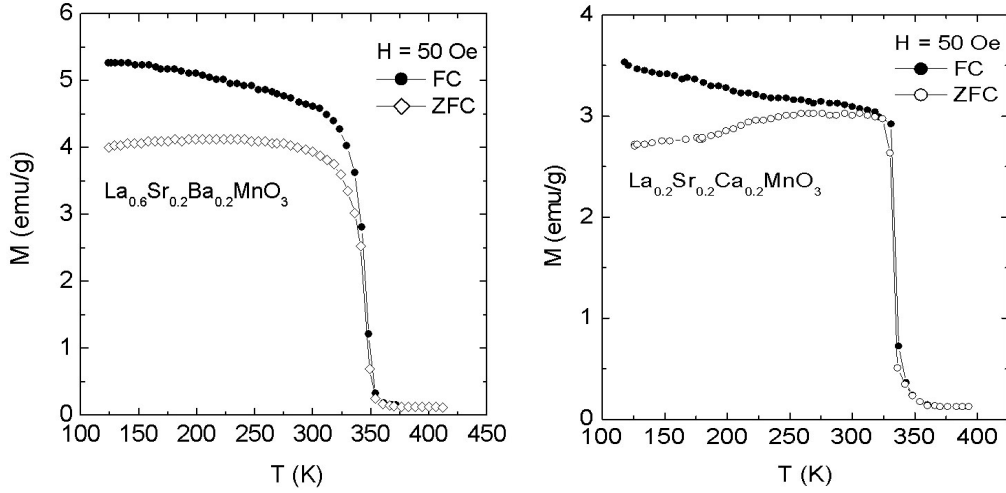
Fig. 1. Temperature dependencies of magnetization measured for both zero-field-cooled (ZFC) and field-cooled (FC) $La_{0.6}Sr_{0.2}Ba_{0.2}MnO_3$ and $La_{0.6}Sr_{0.2}Ca_{0.2}MnO_3$ samples in the field of 50 Oe

Table. Curie temperature T_C and the maximum magnetic entropy change $\left|\Delta S_M^{max}\right|$ for different compositions

Composition	T_C (K)	$\left|\Delta S_M^{max}\right|$ (J/(kg·K))	ΔH (T)	Reference
$La_{0.6}Ca_{0.4}MnO_3$	263	5.0	3	[7]
$La_{0.65}Ca_{0.35}Mn_{0.9}Ti_{0.1}O_3$	103	1.3	3	[7]
$La_{0.975}Li_{0.025}Mn_{0.9}Ti_{0.1}O_3$	90	2.0	3	[7]
$La_{0.65}Sr_{0.35}MnO_3$	305	2.12	1	present work
$La_{0.6}Sr_{0.2}Ca_{0.2}MnO_3$	337	1.96	1	present work
$La_{0.6}Sr_{0.2}Ba_{0.2}MnO_3$	354	2.26	1	present work
$La_{0.7}Ba_{0.3}MnO_3$	336	1.60	1	present work
$La_{0.7}Ca_{0.06}Ba_{0.24}MnO_3$	320	1.72	1	present work
$La_{0.65}Nd_{0.05}Ca_{0.3}MnO_3$	250	1.68	1	[9]
$La_{0.65}Nd_{0.05}Ca_{0.3}Mn_{0.9}Cr_{0.1}O_3$	220	0.96	1	[9]
$La_{0.65}Nd_{0.05}Ca_{0.3}Mn_{0.9}Fe_{0.1}O_3$	130	0.42	1	[9]
Gd	294	4.2	1.5	[4]
$Gd_5(Si_2Ge_2)$	276	14	2	[4]

Using Eq. (7), the changes of magnetic entropy under the influence of the field of 10 kOe have been calculated for all the samples and plotted as a function of temperature (Fig. 3). We summarized the changes of the maximum magnetic entropy $\left|\Delta S_M^{max}\right|$ for all the samples in the table. Among the compositions investigated, LSBMO exhibits the highest value of $\left|\Delta S_M^{max}\right|$ (2.26 J/(kg·K)) at $T_C = 354$ K (Fig. 3).
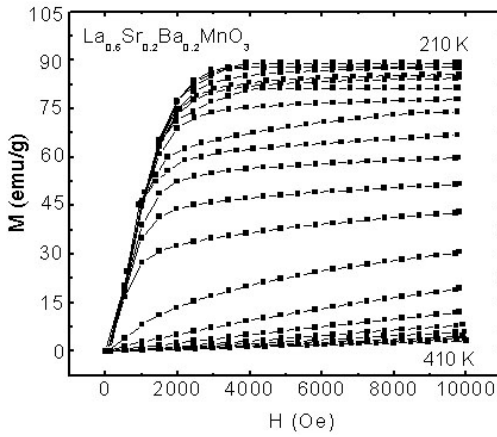
Fig. 2. Magnetic field dependencies
of the magnetization for La$_{0.6}$Sr$_{0.2}$Ba$_{0.2}$MnO$_3$
at various temperatures ranging
from 210 K to 410 K
(ΔT = 10 K)
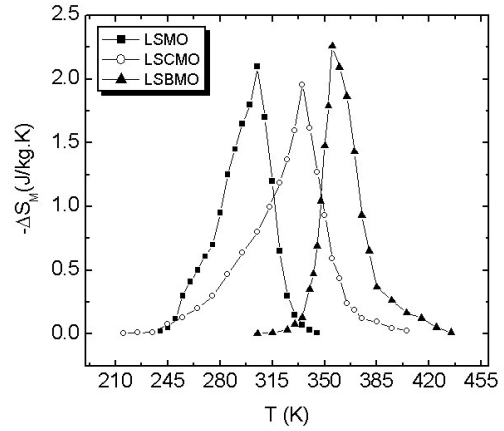
Fig. 3. Magnetic entropy changes induced
by the field of 10 kOe as a function of temperature
for the samples of La$_{0.65}$Sr$_{0.35}$MnO$_3$ (LSMO),
La$_{0.6}$Sr$_{0.2}$Ca$_{0.2}$MnO$_3$ (LSCMO),
and La$_{0.6}$Sr$_{0.2}$Ba$_{0.2}$MnO$_3$ (LSBMO)

In order to complete the analysis, in terms of Eq. (6), we also estimated the adiabatic temperature change ΔT_{ad} for the LSBMO sample. The estimated value of ΔT_{ad} is ~ 1.1 K in the field of 10 kOe and ~ 4.95 K in the field of 50 kOe. These results indicate that the samples investigated are promising materials for magnetic refrigerators. To explain in detail such a large change of magnetic entropy in perovskite manganites, the Zener double-exchange model has been taken into account [12]. According to this model, the changes of magnetic entropy caused by the presence of the external magnetic field relate closely to the mechanism of double-exchange interaction between Mn^{3+} and Mn^{4+} ions and vary substantially with the change in the Mn^{4+}/Mn^{3+} ratio due to various doping processes [8–10].

In the cases where increase of the Mn^{4+}/Mn^{3+} ratio leads to an enhancement in the double-exchange interaction between Mn^{3+} and Mn^{4+} ions, a substantial magnetic entropy variation is observed. For our samples, the partial replacement of La with Sr or (Ba, Ca) favoured the double-exchange interaction arising from the increase of the Mn^{4+}/Mn^{3+} ratio, and that, in turn, led to a significant change of magnetic entropy. Additionally, Guo et al. [13] proposed that the considerable change of magnetic entropy in perovskite manganites could originate from the spin-lattice coupling in the magnetic ordering process. Because of the strong coupling between spin and lattice, significant changes of the lattice accompanying magnetic transition in perovskite manganites has been observed [14]. The lattice structural change in the $\langle \mathrm{Mn} - \mathrm{O} \rangle$ bond distance as well as in the $\langle \mathrm{Mn} - \mathrm{O} - \mathrm{Mn} \rangle$ bond angle would, in turn, favour the spin ordering. Therefore, a more abrupt variation of magnetization occurring near T_C and resulting in a substantial change of the magnetic entropy, i.e. in the strong MC effect, could be attributed to this effect. For comparison, the data of several magnetic

materials, which could be used as active refrigerants, were summarized in the table. Though the values of $\left|\Delta S_M^{\max}\right|$ for manganites are smaller than those for the most conspicuous magneto-caloric material $Gd_5(Si_2Ge_2)$, the perovskite manganites are easy to fabricate and exhibit a higher chemical stability as well as a higher resistivity, which is favourable for lowering of eddy current heating. Furthermore, T_C of ceramic materials can be easily adjusted by tuning the doping concentration. As a result of this procedure, a considerable magnetic entropy change can be observed in different temperature ranges from low temperature to near or above room temperature, which is beneficial for magnetic refrigerators operating in a desired variety of temperatures.

4. Conclusions

Changes of maximum magnetic entropy in $La_{0.65}Sr_{0.35}MnO_3$, $La_{0.6}Sr_{0.2}Ca_{0.2}MnO_3$, $La_{0.6}Sr_{0.2}Ba_{0.2}MnO_3$, $La_{0.7}Ba_{0.3}MnO_3$ and $La_{0.7}Ba_{0.24}Ca_{0.06}MnO_3$ perovskite manganites occurring at their Curie temperatures of above 300 K were observed. Among the compositions investigated, $La_{0.6}Sr_{0.2}Ba_{0.2}MnO_3$ reveals the highest value of 2.26 J/(kg·K) for $\left|\Delta S_M^{\max}\right|$ at $T_C = 354$ K, under the 10 kOe field applied. The estimated ΔT_{ad} value for this sample is ~1.1 K and ~4.95 K in the fields of 10 kOe and 50 kOe, respectively. The increase of the Mn^{4+}/Mn^{3+} ratio leads to an enhancement in the double-exchange interaction between Mn^{3+} and Mn^{4+} ions, and hence it results in a substantial magnetic entropy variation. The significant magnetocaloric effect was observed in the presently investigated materials above the Curie temperature of 300 K, indicating that these materials can be very appropriate for above room temperaturemagnetic refrigeration applications.

References

[1] WARBURG E., Ann. Phys., 13 (1881), 141.
[2] JU H.L., GOPALAKRISHNAN I., PENG J.L., LI Q., XIONG G.C., VENKATEASAN T., GREENE R.L., Phys. Rev., B51 (1995), 6143.
[3] RADAELLI P.G., COX D.E., MAREZIO M., CHEONG S.-W., SCHIFFER P.E., RAMIREZ A.P., Phys. Rev. Lett., 75 (1995), 4488.
[4] PECHARSKY V.K., GSCHNEIDNER K.A. Jr., Phys. Rev. Lett., 78 (1997), 4494.
[5] VON HELMOLT R., WECKER J., HOLZAPFEL B., SCHULTZ L., SAMWER K., Phys. Rev. Lett., 71 (1993), 2331.
[6] PRINZ G.A., J. Magn. Magn. Mater., 200 (1999), 57.
[7] BOHIGAS X., TEJADA J., DEL BARCO E., ZHANG X.X., SALES M., Appl. Phys. Lett., 73 (1998), 390.
[8] SUN Y., XU X., ZHANG Y., J. Magn. Magn. Mater., 219 (2000), 183.

[9] WANG Z.M., NI G., XU Q.Y., SANG H., DU Y.W., J. Magn. Magn. Mater., 234 (2001), 371.

[10] PHAN M.H., TIAN S.B., YU S.C., ULYANOV A.N., J. Magn. Magn. Mater. (in press).

[11] SUN Y., TONG W., ZHANG Y., J. Magn. Magn. Mater., 232 (2001), 205.

[12] ZENER C., Phys. Rev., 81 (1951), 440; 82 (1955), 403.

[13] GUO Z.B., DU Y.M., ZHU J.S., HUANG H., DING W.P., FENG D., Phys. Rev. Lett., 78 (1997), 1142.

[14] RADAELLI P.G., COX D.E., MAREZIO M., CHEONG S.W., SCHIFFER P.E., RAMIREZ A.P., Phys. Rev. Lett., 75 (1995), 4488.

Microstructure and magnetic properties of NdFeB magnets fabricated by current-applied pressure-assisted process

Y.B. KIM[1*], H.T. KIM[1], S.H. CHO[1, 2], G.A. KAPUSTIN[3**]

Institute of Standards and Science (KRISS), P.O. Box 3, Taedok, Korea

[2]Chungnam National University, Korea

[3]Kurchatov Institute, Russia

The microstructure and magnetic properties of isotropic and anisotropic NdFeB magnets fabricated by the current-applied pressure-assisted (CAPA) process have been investigated. The process consists of CA-press to make full dense isotropic magnets and CA-deformation to obtain high-energy anisotropic magnets. During the CA-press, the increase of pressure applied is found to suppress the grain growth and to lead to high coercivity, while the increase of applied current deteriorates coercivity. Through the CA-deformation process, the platelet grains with the *c*-axis texture parallel to the press direction are formed. The best properties of CA-deformed magnets obtained from MQP-A powder were $B_r = 1.36$ T (13.6 kG), $_iH_c = 868$ kA/m (10.9 kOe) and $(BH)_{max} = 352$ kJ/m^3 (44.2 MGOe) and those obtained from MQUG powder were $B_r = 1.31$ T (13.1 kG), $_iH_c = 1457$ kA/m (18.3 kOe) and $(BH)_{max} = 333$ kJ/m^3 (41.8 MGOe).

Key words: *NdFeB; CAPA-process; hot-working; permanent magnet*

1. Introduction

Hot-press and subsequent die-upset [1–3] of rapidly quenched NdFeB alloys induces magnetic anisotropy and a high-energy product. High coercivity with fine grain structure is the merit of the process. Recently, we have investigated a modified hot-working process to obtain anisotropic NdFeB magnets [4, 5]. The process, referred to as current-applied pressure-assisted (CAPA) process hereinafter, is quick because high electric current is applied to heat the specimen, and a high coercivity with high-energy product is easily obtained.

---

*Corresponding author, e-mail: ybkim@kriss.re.kr.
**Present address: Institute of Standards and Science, Korea.

In this work, we report the procedure of the process and the magnetic properties, texture and microstructures of the magnets obtained.

2. Experimental procedure

Raw materials used in the experiments were commercial powders MQPA, MQPB and MQUG (Magnequench) with compositions shown in Table 1. For consolidation of the powders, 15–20 g of the raw materials were poured into a graphite mold (OD: 45 mm, ID: 20 mm, H: 40 mm), then, DC current (1000–3000 A) and mechanical pressure (15–100 MPa) were applied simultaneously through the upper and lower punches under the evacuated Ar atmosphere. The powder was thus heated by Joule heat and compacted until densification was attained. This process, referred to as current-applied press (CA-press) hereinafter, is shown in Fig. 1a. In order to endow the anisotropy, the CA-pressed magnet was placed between the upper and lower graphite punches in an open die, then pressed to deform while current was applied. This procedure is shown in Fig. 1b and referred to as current applied deformation (CA-deformation) process. During the processes, the shrinkage of specimen, mold temperature, applied load and current were monitored.

Table 1. Nominal composition of raw powders (wt. %).
The numbers in parentheses correspond to atomic percentage

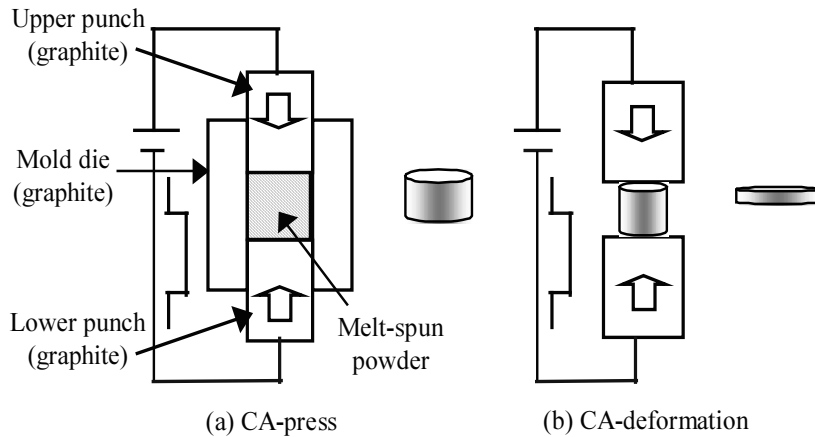| Powder	Fe	Nd	B	Co	Dy	Ga
MQPA	68.6 (80.9)	30.5 (13.8)	0.9 (5.3)			
MQPB	66.6 (77.3)	27 (12.2)	0.9 (5.2)	5 (5.2)	0.5 (0.2)	
MQUG	61.6 (73.2)	26.1 (12)	0.9 (5.6)	5.9 (6.6)	4.9 (2)	0.6 (0.6)

Fig. 1. Schematic presentation of the CAPA process

To determine magnetic properties, a pulsed field magnetometer and a hysteresis-graph system were used. The crystal phase was identified by X-ray diffractometry with CuK$_\alpha$ radiation. Pole figures corresponding to (006) reflections were obtained using a Philips X-ray diffractometer by employing the geometry of Schulz reflection method [6]. The detector was set at fixed angles $2\theta = 44.5°$ and $38.4°$ relative to the incident beam for the measurement of the intensity of (006) and (105) reflections. The tilt angle (α) was varied from 0° to 80° in steps of 5°. The second rotation axis, azimuth angle (β), was varied from 0° to 360° in steps of 20°.

3. Results and discussion

Figures 2a and b show the examples of the change of fabrication parameters during CA-press and CA-deformation, respectively. The shrinkage of powder during CA-press occurs in two steps. The first shrinkage observed at the initial stage is cold-press of powder, and the second shrinkage occurring for $t = 40–110$ s is due to the powder bonding through Nd-rich liquid phase formed by the Joule heating. The decrease of the load applied at $t \approx 40$ s and the increase of the temperature for $t = 60–110$ s coincide well with the trace of shrinkage. In the case of CA-deformation, the shrinkage also occurs in two steps. The first step is a rapid deformation at a rate of ~1.2 mm/s, which occurs during 2–3 s at the initial stage, and 60–70% of the whole deformation is achieved. The second step is a slower deformation at a rate of ~0.03 mm/s, and the rest of deformation proceeds for about 30 s.
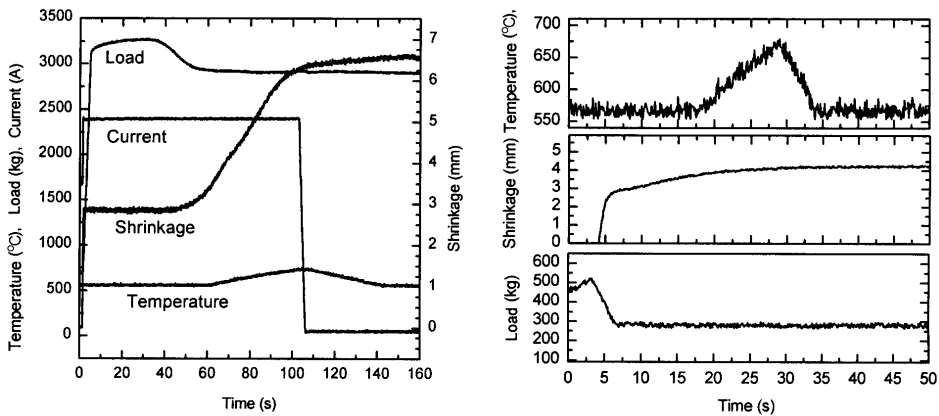

Fig. 2. Changes of experimental parameters during CA-press (a) and CA-deformation (b) process

Figures 3a and b show the magnetic properties and density of CA-pressed magnets as a function of the pressure applied and electric current, respectively. As shown in Fig. 3a, nearly a full-dense magnet is obtained at $P_a \geq 20$ MPa, and the remanence and energy product reach the maximum at $P_a = 20–30$ MPa. A further increase of P_a re-

sults in a continuous increase of $_iH_c$. The increase of coercivity is due to the grain refinement by high pressure . The full density is obtained above $I = 1500$ A (Fig. 3b). A further increase of the current, however, decreases the coercivity, probably due to the disclosure of the specimen to high temperature by high current flowing.
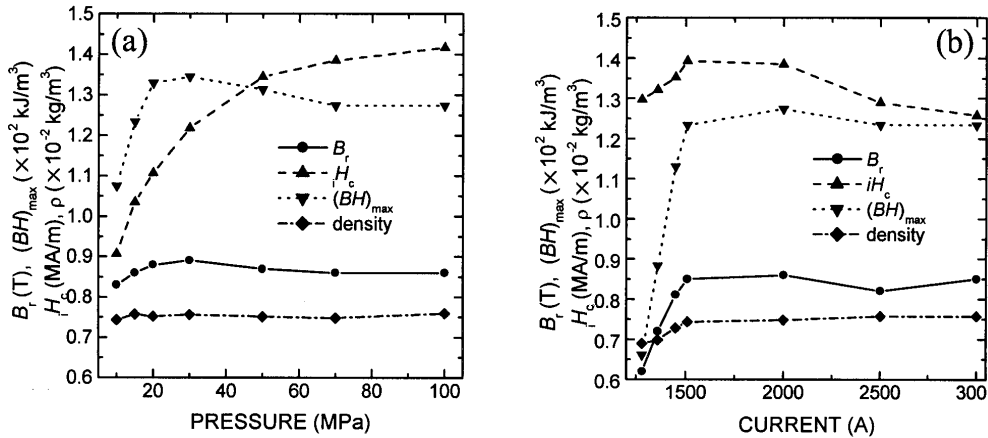

Fig. 3. Magnetic properties and density of CA-pressed magnets
as a function of pressure applied (a) and electric current (b)

Figure 4 shows the demagnetization curves of the MQPA powder and its CA-pressed and CA-deformed magnets. The CA-pressed magnet maintains the high coercivity of raw powder, while the remanence increases by 8.5%. The high coercivity of CA-press magnet, which is comparable to the coercivity of raw powder, is due to a small grain size almost unchanged compared to the original state. After CA-deformation, the remanence increases considerably with the expense of the coercivity. The SEM micrograph shows well-aligned platelet grains of 200–700 nm in diameter grown perpendicular to the press direction (Fig. 5).
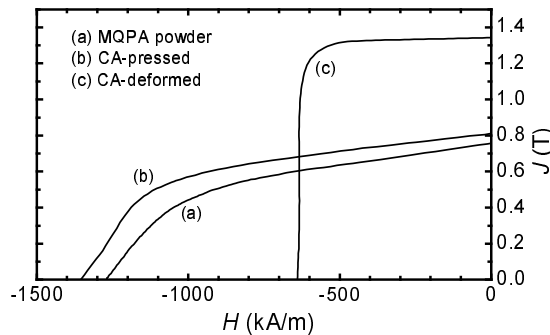

Fig. 4. Demagnetization curves of MQPA powder,
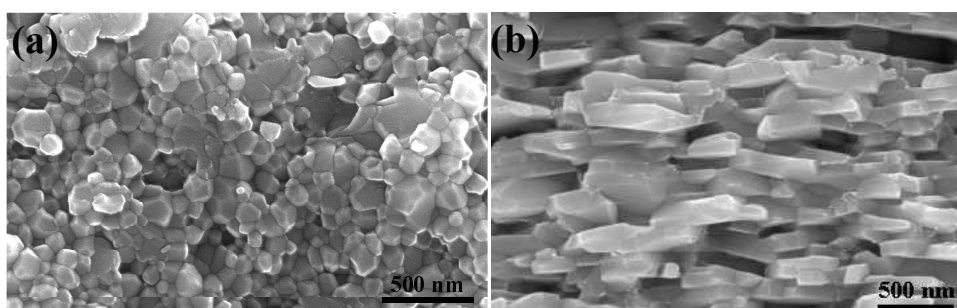CA-pressed and CA-deformed magnets

Fig. 5. SEM micrographs of fracture surface
for CA-pressed (a) and CA-deformed (b) magnets

Table 2. Magnetic properties of raw powders, CA-pressed and CA-deformed magnets

Type of specimen		Residual induction B_r		Intrinsic coercivity $_iH_c$		Energy product $(BH)_{max}$	
		(T)	(kG)	(kA/m)	(kOe)	(kJ/m^3)	(MGOe)
MQPA	raw powder	0.76	7.6	1360	17.1	126	15.8
	CA-pressed	0.87	8.7	1416	17.8	132	16.6
	CA-deformed	1.36	13.6	868	10.8	352	44.2
MQPB	raw powder	0.89	8.9	740	9.3	126	15.8
	CA-pressed	0.79	7.9	287	3.6	80	10.1
	CA-deformed	1.07	10.7	174	2.2	72	9.1
MQUG	raw powder	0.96	6.9	1187	14.9	67	8.4
	CA-pressed	0.80	8.0	2022	25.1	117	14.7
	CA-deformed	1.31	13.1	1457	18.3	333	41.8

In Table 2, the magnetic properties of CA-pressed and CA-deformed magnets obtained from various raw powders are summarized. The magnets fabricated from MQUG powder show particularly high coercivity of 2022 kA/m for CA-pressed and of 1457 kA/m for CA-deformed magnets, possibly due to the fine grain structure as well as the increase of crystal anisotropy by Dy addition. The magnets obtained from MQPB powder, however, show low coercivity and low remanence. The texture of CA-deformed magnets examined by (006) pole figure shows well-developed *c*-axis alignment for the magnet obtained from MQPA, but poor alignment for the magnet obtained from MQPB (Fig. 6). The SEM micrographs observed along the press direction reveal that the magnet is composed of two regions, as shown in Fig. 7. One area – dark (a), is the region with no texture, and the other – bright (b) – is the region well-textured but composed of large grains of 3–4 μm in diameter. Clearly, the low coercivity is due to large grains and the low remanence is caused by large volume of untextured area.
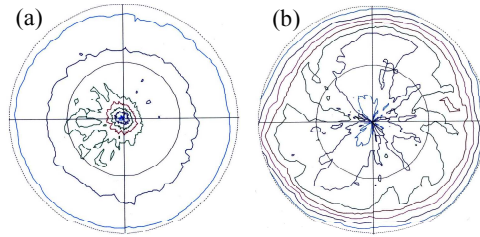
Fig. 6. (006) pole figures of CA-deformed magnets
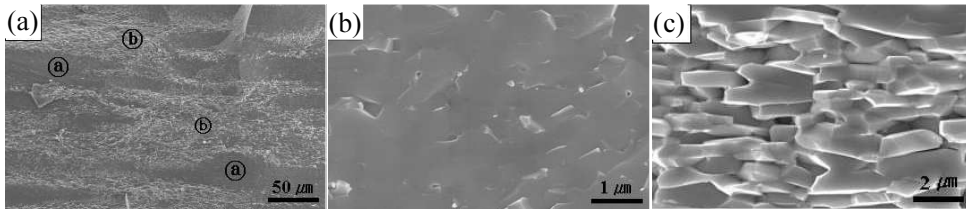obtained from MQPA (a) and MQPB (b) powders

Fig. 7. SEM micrographs of the fracture surface of CA-deformed magnet
obtained from MQPB powder. The two magnifications, i.e. (b) and (c),
correspond to the zones a) and b) of (a), respectively

4. Conclusion

Nanocrystalline NdFeB magnets with high-energy product have been obtained by applying the CAPA-process. During CA-press, the increase of the pressure applied increases the coercivity. However, the increase of the current applied decreases the coercivity. By CA-deformation treatment, the platelet grains with the c-axis texture parallel to the press direction are obtained. The best properties obtained for MQPA powder were: B_r = 1.36 T (13.6 kG), $_iH_c$ = 868 kA/m (10.9 kOe) and $(BH)_{max}$ = 352 kJ/m^3 (44.2 MGOe), and those obtained for MQUG powder were: B_r = 1.31 T (13.1 kG), $_iH_c$ = 1457 kA/m (18.3 kOe) and $(BH)_{max}$ = 333 kJ/m^3 (41.8 MGOe).

References

[1] LEE R.W., Appl. Phys. Lett., 46 (1985), 790.
[2] LEE R.W., SCHAFFEL N., BREWER L., IEEE Trans. Magn., 21 (1985), 1958.
[3] MISHRA R.K., CHU T.Y., RABENBERG L.K., J. Magn. Magn. Mater., 84 (1990), 88.
[4] KIM H.T., KIM Y.B., KIM H.S., J. Magn. Magn. Mater., 224 (2001), 173.
[5] KIM H.T., KIM Y.B., KIM H.S., J. Magnetics, 5 (4) (2000), 130.
[6] SCHULTZ G., J. Appl. Phys., 19 (1949), 388.

Effects of an external magnetic field on the perpendicular magnetic anisotropy of electrodeposited micro-patterned arrays

W. Y. JEUNG, D. H. CHOI, K. H. LEE[*]

Metal Processing Research Center, Korea Institute of Science and Technology, Seoul 136-791, Korea

We have investigated effects of an external magnetic field on perpendicular magnetic anisotropy (PMA) of electrodeposited continuous films and micro-patterned arrays. For continuous films, external magnetic field gave rise to a highly aligned grain structure with PMA. Our results indicate that the effect of applied magnetic field is apparent only at specific current density. XRD patterns showed that electrodeposited continuous Co films consist of hexagonal cobalt only and have strong texture for grains with the *c*-axis lying perpendicular to the film plane. The patterned arrays were fabricated by UV-LIGA process, and PMA was modified by changing the aspect ratio of patterned arrays. Our results suggest that there is a critical aspect ratio at which PMA dominates in-plane anisotropy. For the patterned arrays, however, the external magnetic field was not very effective due to a large concentration polarization.

Key words: *cobalt; magnetic field; perpendicular anisotropy; electrodeposition*

1. Introduction

Recently, demands for the electrodeposition of hard magnetic materials have increased significantly due to their potential applications in ultrahigh density magnetic recording and MEMS [1–5]. It has been reported that hard magnetic materials improved the density of recording medias in the field of magnetic recording media, reduced the driving voltage in the operation of actuators, and enhanced the sensibility of sensors [6, 7]. In most cases, however, hard magnetic materials electrodeposited as thin films are easily magnetized in the in-plane direction because of their large shape anisotropy. Therefore, it is important to control the crystallographic orientation and aspect ratio of the magnet arrays in order to produce hard magnet arrays with PMA.

In this study, we report the electrodeposited continuous films and micro-patterned arrays of cobalt, which show a magnetic anisotropy with an easy axis perpendicular to

_____

[*]Corresponding author, e-mail: kwanhyi@kist.re.kr

the film plane. We also discuss the correlation between structural, crystallographic, and magnetic properties.

2. Experimental

Specimens were prepared by constant current electrodepositing. The working electrode (5 mm×5 mm) was a 100 nm thick Au layer on (100) Si wafer. The current density was varied from 0.75 to 5 A/dm^2 and electrolytic cobalt chips (99.9% purity) in a Ti basket were used as anodes. The electrolyte was a mixed solution of 100 g/dm^3 $CoCl_2 \cdot 6H_2O$, 100 g/dm^3 $CoSO_4 \cdot 7H_2O$, and 100 g/dm^3 NH_4Cl. All solutions were prepared using ultra-pure water (over 18 MΩ at 30±1 °C). The agitation rate was 50 strokes per minute during electrodeposition using the paddle cell [10].

In a CV (cyclic voltammetry) test, the same working electrode was used with the constant current plating. The counter electrode and reference electrode were a graphite plate and a saturated Calomel electrode, respectively. The scan rate was 20 mV/sec. External magnetic field was applied using two magnets (Nd–Fe–B, 0.5 T) facing each other during electrodeposition of the magnet arrays to produce a highly aligned grain structure with perpendicular anisotropy in the magnetic properties. Magnetic properties of prepared specimens were measured with vibrating sample magnetometer, VSM-5, Toei, Japan. Crystal structure and texture were examined by X-ray diffraction (DY983, Philips, The Netherlands) with the operating condition of 30 kV and 20 mA using Mo target.

3. Results and discussion

In Figure 1, there are shown representative *M–H* loops of cobalt continuous films are shown electrodeposited without and with an external magnetic field (0.5 Tesla) measured in a magnetic field parallel (dashed line) and perpendicular (solid line) to the film plane, respectively.

The cobalt film electrodeposited without an external magnetic field shows a typical loop resulting from shape anisotropy with an easy axis parallel to the film plane and a hard axis perpendicular to the film plane (Fig. 1a). The intrinsic coercivity *Hc* was found to be ~ 60 Oe for in-plane direction and ~250 Oe for perpendicular direction, and this difference is thought to be attributable to a mixed anisotropy of shape and magnetocrystalline anisotropy. On the other hand, when a *M–H* loop was measured in the magnetic field perpendicular to the film plane (Fig. 1b), the electrodeposit with an external magnetic field was found to have a small minor-loop-like loop showing coercivity of ~500 Oe which is twice as high as that in Fig. 1a. For in-plane direction, the *M–H* loop in Fig. 1b was very similar to that in Fig. 1a. From these results it is inferred that the external magnetic field might induce the *c*-axis of growing
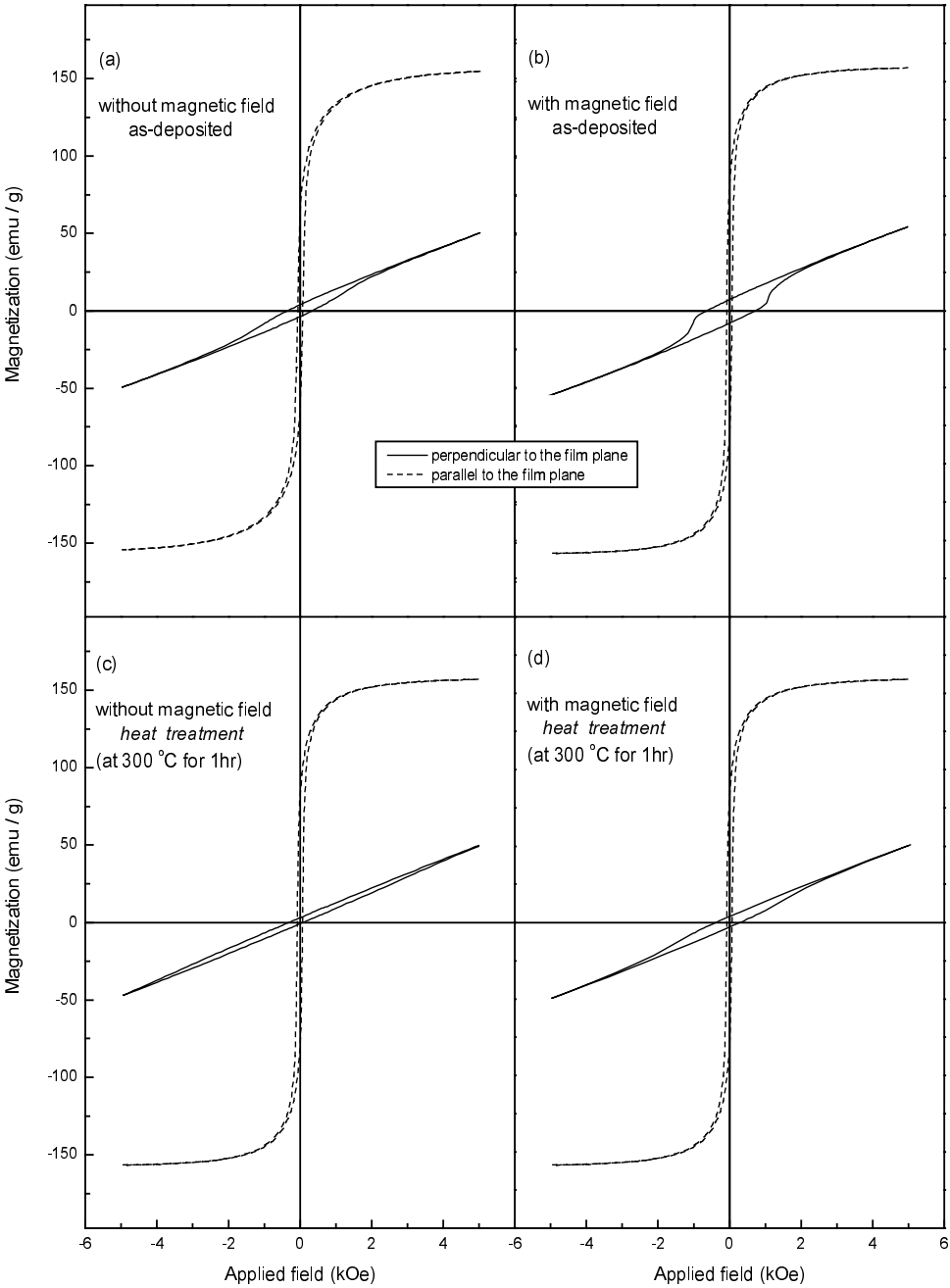
Fig. 1. *M–H* hysteresis loops of the electrodeposited Co films:
a) without magnetic field (as-deposited), b) with magnetic field (as-deposited),
c) without magnetic field (annealed at 300 °C for 1 hr),
d) with magnetic field (annealed at 300 °C for 1 hr)

cobalt crystallites in the direction perpendicular to the film plane, and make the grain size close to the single domain size. Figures 1c and d also show the variations of the *M–H* loops of the cobalt films electrodeposited without (Fig. 1c) and with (Fig. 1d) an external magnetic field after the samples were annealed at 300 °C for 1 hr. When the sample was electrodeposited without an external magnetic field, the *M–H* loop was independent of the heat treatment except that the perpendicular coercivity decreased to some extent. In Fig. 1d, however, the minor-loop-like loop disappeared after annealing, which indicated the shape anisotropy gradually becoming dominant in the mixed anisotropy, but the magnetocrystalline anisotropy was still effective (this may be deduced from the fact that the value of the coercivity remained ~500 Oe regardless of the heat treatment). These results demonstrate that the application of an external magnetic field during electrodeposition can affect both the crystallographic orientation and the grain size. Figure 2 presents X-ray diffraction patterns of the continuous films of cobalt electrodeposited without (Fig. 2a) and with (Fig. 2b) an external magnetic field, respectively.
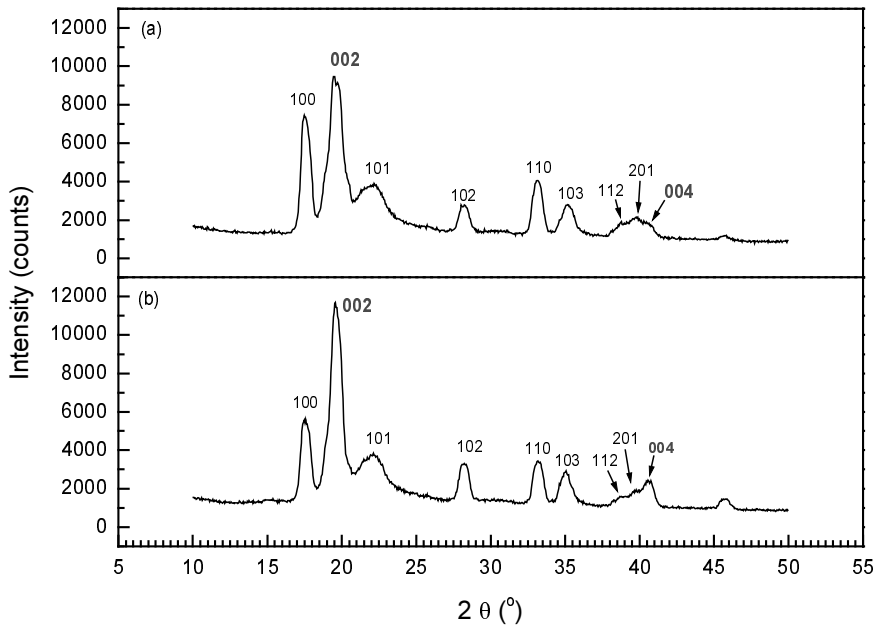

Fig. 2. X-ray diffraction patterns of the Co film electrodeposited without (a) and with (b) an external magnetic field. The electrodeposition was conducted at 1 A/dm^2

In Figure 2b, two peaks from *hcp* cobalt (002) and (004) planes are observed more apparently than in Fig. 2a. This means that the application of an external magnetic field during electrodeposition leads cobalt grains to grow preferentially and form (002) texture. Considering that cobalt grains with the (002) orientation have the *c*-axis

perpendicular to the film plane, the difference between Figs. 1a and 1b can be easily understood.

Figure 3 is a comparison of the cyclic voltammograms measured without (dashed line) and with (solid line) an external magnetic field. The switching potential at which the scanning direction changes from cathodic to anodic one was fixed at −1.1 V in order to eliminate a possible interference from the hydrogen evolution reaction.
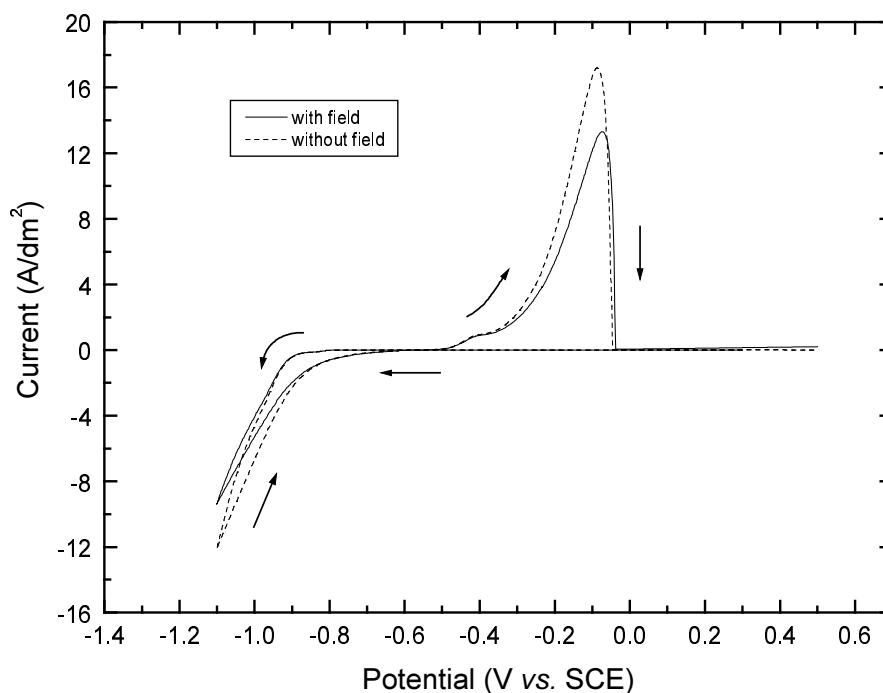

Fig. 3. Comparison of the cyclic voltammograms measured
without (dashed line) and with (solid line) an external magnetic field

The shapes of the cyclic voltammograms in Fig. 3 are similar to each other, but the polarization during the cathodic scan reveals different polarization values. With an external magnetic field of 0.5 Tesla, the polarization is larger and it is well known that the polarization has a close correlation with the size of grain in the electrodeposited alloys, producing small grains when the alloy is electrodeposited at high polarization condition [5, 8, 9]. It can be expected that the application of an external magnetic field induces an increase in polarization and the grain size of Co films may become smaller. The reduction of grain size caused by an increase in polarization has been ascertained by transmission electron microscopy (TEM) in our previous work [5]. Interestingly, the effect of applied external magnetic field was apparent only at specific current density, 2.5 A/dm^2. For higher current densities, it seems that the electrocrystallization cannot proceed sufficiently due to large concentration polarization.

For the micro-patterned arrays of cobalt as in Fig. 4, typical *M–H* loops were measured in perpendicular (Fig. 5a) and in-plane (Fig. 5b) directions to the film plane depending on the variation of aspect ratios.
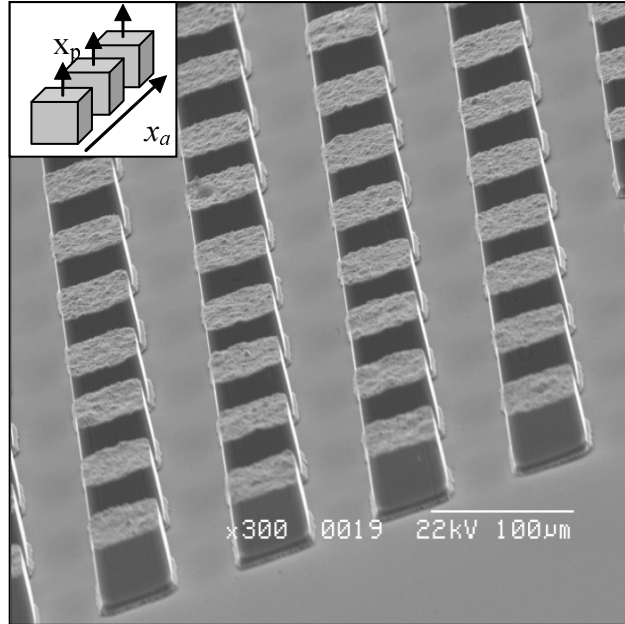

Fig. 4. Scanning electron micrographs of cobalt arrays
(50 μm×50 μm×50 μm) stripped the photoresist

Although Co cubic (50 μm×50 μm×50 μm) array was expected to have the same *M–H* loop in x_p direction as in x_a direction in Fig. 4, it exhibits different magnetization values according to the direction of the field applied. For example, when the field applied was 2000 Oe, magnetization measured in the x_p direction was 58 emu/g, being 81 emu/g in x_a direction. From this result it can be inferred that Co array has shape anisotropy to be magnetized in the x_a direction.

In Figure 5, when two patterned arrays of the same dimension (50 μm×50 μm ×50 μm) are compared with each other, they exhibit almost the same *M–H* loops. This means that application of an external magnetic field is insufficiently effective to improve PMA for the electrodeposited patterned array. It has been reported that in a through-template electrodeposition like this work, mass-transfer effects are significant, and diffusion of ions through the template is a rate-determining step [6,11]. In these conditions, a large concentration polarization appears. The reason why the application of an external magnetic field was not effective for patterned arrays can be attributed to an insufficient electrocrystallizaton due to the large concentration polarization. It is not ascertained whether if cobalt patterned arrays have any magnetocrystalline anisotropy.
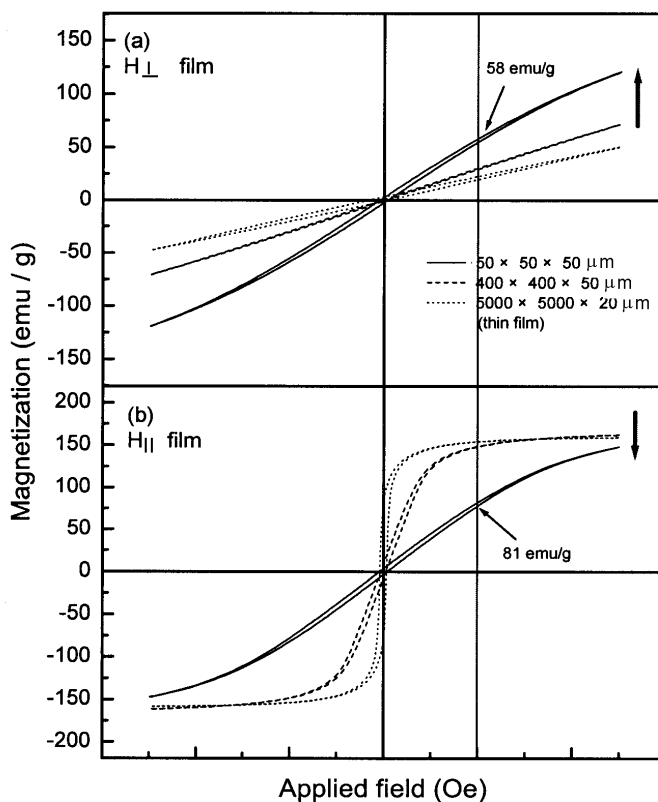
Fig. 5. *M–H* hysteresis loops of patterned Co arrays according to the aspect ratio.
Loops were measured in perpendicular (a) and in-plane directions (b) to the film plane

4. Conclusion

We studied the effects of an external magnetic field on continuous films and mi-
cro-patterned array in order to improve the PMA of cobalt electrodeposits. Our
experimental results give evidence that an external magnetic field leads to the (002)
preferred crystallographic orientations of continuous cobalt film and the reduction of
the grain size. We also found that the patterned cobalt array shows a predominant
PMA in competition with in-plane shape anisotropy. Our results indicate that applica-
tion of an external magnetic field is effective to improve PMA for electrodeposited
continuous film, but little dominant for patterned array due to large concentration
polarization during electrodeposition.

References

[1] HORKANS J., SEAGLE D.J., CHANG I.H., J. Electrochem. Soc., 137 (1990), 2056.
[2] MYUNG N.V., YANG H., SCHWARTZ M., JUDY J.W., YANG C.K., NOBE K., Abstracts of 198th ECS
    Meeting, 2000-2 (2000), 583.

[3] Ross C.A., Haratani S., Castano F.J., Hao Y., Hwang M., Shima M., Cheng J.Y., J. Appl. Phys., 91 (2002), 6848.

[4] Sung M., Zangari G., Metzger R.M., IEEE Trans. Magn., 36 (2000), 3005.

[5] Lee K.H., Kim G.H., Jeung W.Y., Electrochem. Commun., 4 (2002), 605.

[6] Datta M., Landolt D., Electrochim. Acta, 45 (2000), 2535.

[7] Osaka T., Kasai N., Koiwa I., Goto F., Suganuma Y., J. Electrochem. Soc., 130 (1983), 568.

[8] Dini J.W., Plat. Surf. Finish., 75 (1988), 642.

[9] Dini J.W., *Electrodeposition* (Chapter 6), NOYES Publications, New Jersey, 1992.

[10] US Patent 3, 652, 442 (1972), 4, 102, 756 (1978).

[11] Mehdizadeh S., Dukovic J., Andricacos P.C., Romankiw L.T., Cheh H.Y., J. Electrochem. Soc., 140 (1993), 3497.